permafrost table) and the lakes that appear dark have a water layer beneath the ice cover. This finding is important from several points of view. Such images could provide information to local communities concerning which lakes to tap for a winter water supply. The biological regime between completely and partly frozen lakes is different, the latter having far more fish.

### Conclusions

Satellite-borne active microwave sensors offer the only means of obtaining high-resolution imagery of polar ice during all times, thus penetrating the "observational barrier" that has hampered much-needed research. Sequential synoptic active microwave imagery of sea ice is urgently needed to test and help develop numerical models of air/ice/ocean interaction. Such data will greatly enhance the usefulness of ESMR imagery of the gross characteristics of the sea ice canopies.

The only remote-sensing means capable of observing subsurface structures of ice-caps and glaciers is active microwave. The SLAR images of glaciers clearly delineate the accumulation foliation planes through several meters of snow cover. Those of ice-caps reveal a subsurface parallel banded structure. Such images promise to provide needed data on accumulation amounts, and patterns may help in determining surface flow patterns. Satellite radar is the best way to track and study the metamorphosis of ice island (bergs).

Active microwave imaging of lake and estuary ice will provide high-resolution, sequential, synoptic data needed to extend the navigable season in busy waterways such as the Gulf of St. Lawrence and the Baltic Sea.

The SLAR can be used to determine which tundra lakes are frozen to the bottom and which are not, an important logistical and ecological technique.

Although the potential of active microwave sensors that currently exist has been demonstrated as ice sensors, neither U.S. nor U.S.S.R. scientists yet know what frequency (or combination of frequencies) or what polarization (or combination of polarizations) is best for monitoring either sea ice or lake ice. Although earlier theories might be used to permit some extrapolation or interpolation, these too need improvement and further verification. Hence, in addition to further flights over the ice, both theoretical research and research with a microwave spectrometer that can be transported onto the ice seems to be needed if the optimum system parameters are to be established.

## PART E



## TECHNICAL APPROACHES

### INSTRUMENTATION

Radar altimeters, scatterometers, and imaging radar are the major instruments needed to accomplish the applications discussed earlier in this chapter. This section describes the instrumentation in terms of its functions, future developments, constraints, and applications.

#### Altimetry

*Introduction.*—Satellite altimetry has demonstrated the capability for determining mean sea level. Although past efforts have not achieved the ultimate goal in spatial and height resolution, it is attainable in the next decade. On attaining this goal, satellite altimetry will enable improved knowledge of

the geoid, increasing the number of terms in the knowledge of the gravity field and the upward extension of the surface field. Also, the position and density of underwater topographic features can be determined from geoid undulations and satellite tracking. In addition, from waveform analysis of the radar altimeter return, global knowledge of sea slopes, currents and eddies, and estuarine characteristics is possible. From proper choice of orbit parameters and system concepts, an altimeter can provide a global synoptic description of the ocean surface. Figure 3–45 shows the differences between the "computed" and "measured" sea surface from one of the last Skylab experiments as a typical example of a first test (ref. 3–45).

*Satellite altimetry.*—Satellite radar altimetry has the potential to significantly improve knowledge of the geoid and sea state on a global basis. Although the data collection capabilities are limited to nadir, the short-pulse altimeter concept for the simultaneous measurement of surface-height variations and sea state has experimental verification warranting its deployment into space. Both the scientific value and the applications were emphasized in the Terrestrial Environment Solid Earth and Ocean Physics Study conducted during August 1969. Based on available data, the NASA EOPAP [3] (ref. 3–45) recognized the importance of satellite altimetry and has adopted a long-range physical ocean sensing program with objectives that rely heavily on this sensor.

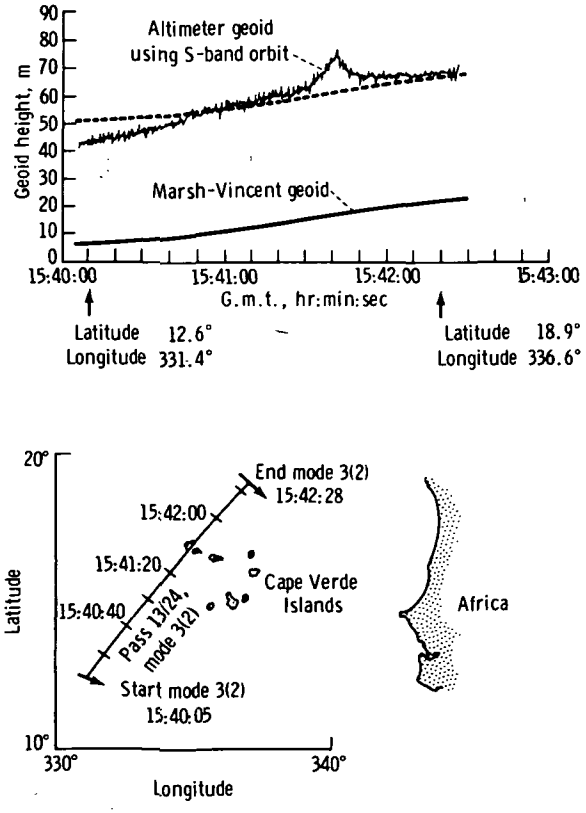


FIGURE 3–45.—Skylab altimeter pass over the Cape Verde Islands.

In all the activities to date, the role of altimetry has been visualized to include detection of dynamic ocean features (tides, waves, currents, etc.) or mapping of permanent mean ocean surface topography (geoid). The subsurface geological features have been known to affect the ocean geoid, and results obtained with the Skylab altimeter have correlated this relationship. These correlations could result in new applications of altimetry for bathymetric positioning of underwater topographic features (ref. 3–50).

The Skylab S193 experimental altimeter has demonstrated a system bias change of less than 20 cm in approximately 6 months of orbital operation. Altitude noise levels slightly less than 1 m have been maintained.

Altimeter tracking over the Great Salt Lake and the Great Lakes obtained altitudes above mean sea level for these features that correlate very nearly to those listed on maps. For mapping the ocean topography (ref. 3–81), a typical system error model has been produced (table 3–VI). Both the uncorrected magnitude and the residual of the best-known corrections that are applied to the data are shown.

Antenna beam pointing and antenna height bias are the two factors that are most critical to mapping surface topography. True

[3] NASA: Earth and Ocean Physics Applications Program. Vol. I—Executive Summary, Vol. II—Rationale and Program Plan, Sept. 1972 (NASA internal document, restricted distribution).

satellite heights are difficult to determine when short orbit arcs are used for analysis of the data. Also, the altitude of the satellite is continually changing, which affects the antenna pointing. Therefore, methods have been developed to extract pointing information from the altimeter waveforms and then to apply corrections to the altitude based on this information.

Figure 3–45 also shows data obtained from a pass over the Cape Verde Islands on September 3, 1973. For comparison, the Goddard (Marsh-Vincent) geoid (refs. 3–44 and 3–50) is shown on the graph. The absolute difference between the altimeter geoid and the Goddard geoid of approximately 45 m is well within the estimated orbit uncertainty. The dotted line on the graph is the geoid shifted for shape comparison. The overall comparison is good except for the 12-m undulation in the vicinity of the Cape Verde Islands. Detailed analyses of the altimeter footprint, noise characteristics, and ground-track indicate that the altimeter was not over land during any part of the pass. Because dynamic sea-surface effects could explain only a few meters of the undulation observed, the geoid undulation observed is surmised to be a real feature.

Figure 3–46 illustrates the altimeter-derived geoid for a pass of data taken on the Skylab 3 mission on September 13, 1973. These data were taken as the altimeter passed over the Mid-Atlantic Ridge in the North Atlantic. Excellent agreement with the general shape of the geoid is again seen and the offset is well within the expected orbit accuracy. A comparison of the altimeter geoid with the bottom topography in the area also shows excellent correlation.

The Skylab altimeter data analysis results are representative of numerous data that have been studied. The instrument performance was excellent, and the geoid shape information derived correlates well with the Goddard global geoid. Also, a strong correlation appears to exist between the derived geoid and underwater topographic features. The agreement between Sklab data and the predictions of system models has been extremely close (ref. 3–82). For example, figure 3–47 illustrates the agreement between

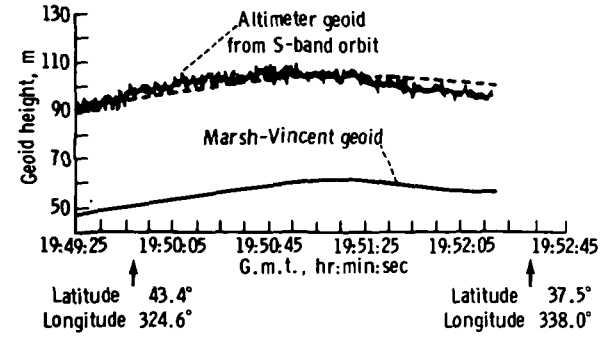


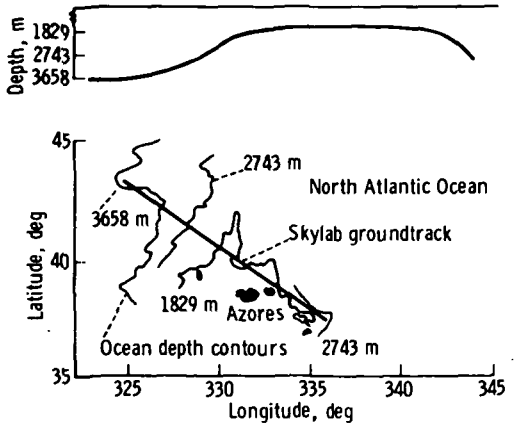


FIGURE 3–46.—Skylab altimeter pass over the Mid-Atlantic Ridge in the North Atlantic.

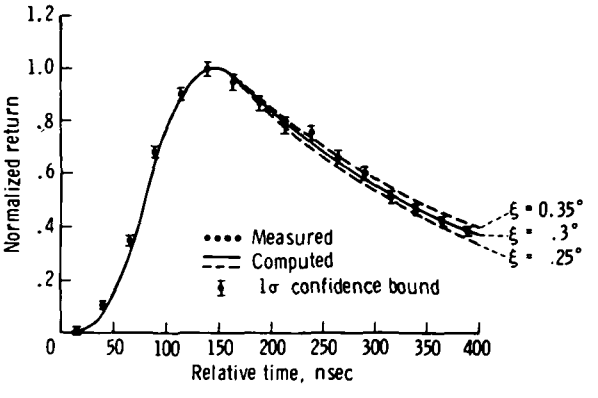


FIGURE 3–47.—A comparison between Skylab data and the predicted waveform (where $\xi$ is pointing offset from nadir).

Skylab data and a predicted waveform for a 0.3° pointing error. The low one-sigma variation indicates the quality of that system for determining pointing.

*Future developments.*—The AAFE pulse compression altimeter development will increase the radar sensitivity and flexibility. This increase improves the radar performance over the NRL nanosecond pulse radar and establishes the feasibility for use in satellite altimetry. The GEOS–C altimeter experiment is primarily intended to demonstrate the operational utility of altimetry for geodesy and oceanography. Thus, the GEOS–C altimeter experiment follows the Skylab S193 altimeter experiment in a planned sequence of developments leading to an operational satellite system for oceanographic applications. The GEOS-C altimeter capability to measure mean-sea-level and ocean-wave heights will be greatly improved over the S193 altimeter. Experiments with GEOS-C (ref. 3–83) will be improved over the Skylab experiment because of improved orbital determination for GEOS-C. The orbital determination capability of the GEOS-C experiment will represent the best in the state of the art in this technology and will show from planned experiments what factors limit this technology for an operational oceanographic satellite. The next planned altimeter is for SEASAT–A and will have two modes of operation. In mode A, the altimeter will have a maximum range noise of 31 cm at a data output rate of 10 Hz, and in mode B, a 10-cm range noise at a data output rate of once per second. An internal calibration mode will provide a capability of an absolute range accuracy calibration to within ±25 cm. Ocean backscatter coefficients will be determined to ±1 dB, and the measurement of significant wave height $H_{1/3}$ of the ocean surface will be determined to ±25 percent of $H_{1/3}$ or 0.5 m, whichever is greater, in the $H_{1/3}$ range of 1- to 20-m wave height. The requirements for mode B are the same as for mode A except that $H_{1/3}$ will be accurate to ±10 percent or 0.5 m, whichever is larger, and that all the data outputs specified will be determined in real time onboard the satellite instead of by ground processing. The mode B goal will be achieved by the use of an onboard maximum-likelihood processor, which will adaptively change the tracking and sea-state algorithms as a function of signal-to-noise ratio and sea state.

*Applications.*—The immediate application of active microwave sensors is in the area of measuring sea state. The ability of mapping sea state globally and synoptically by active remote sensors would provide reference data needed to plan shipping routes, design ships, design offshore structures, and help plan future ports. The knowledge of sea state will also enable the testing of present meteorological and oceanographic models and aid in improving the understanding of the air/sea interactions so that better models can be derived for forecasting sea state and weather.

The intrinsic values of monitoring sea state are not limited to the consideration of wave forces or energy. The knowledge of sea state in the form of a wave spectrum can be used to measure ocean-surface currents (ref. 3–66). The information on global and synoptical ocean surface current systems will be very cost effective in efficiently deploying ships. Understanding mass transport, heat transport, and current systems has dominant effects on economies of marine communities and global weather predictions.

### Scatterometers

*Introduction.*—Active microwave sensors have been used to measure range, reflection or scattering coefficient, and shape of the returned pulse from various objects or scenes. The ability with which a scene or object scatters incident microwave energy can be assessed by measuring the radar-scattering cross sections at various frequencies, polarizations, and incident angles. A microwave scatterometer is a special-purpose radar that is used to quantitatively measure the target reflectance or scattering cross section. Microwave scatterometers are usually simpler than conventional radars because range and velocity measurement capability and the high

spatial resolution (short pulse) requirements are eliminated. Long-pulse and continuous-wave scatterometers have been used to measure the scattering signatures of rough surfaces such as terrain or the ocean. The quantity of interest is the radar-backscatter coefficient, which is the backscattered power per unit area normalized for antenna gain, range loss, and the transmitted power.

The result of measurements taken to date reveals the following information about the dependence of the backscattering cross section from the ocean on windspeed:

1. A range of radar wavelengths exists for which backscatter is primarily dependent on surface windspeed, relatively insensitive to large-scale roughnes.
2. Backscatter at and near the vertical (0° incident angle) monotonically decreases with increasing windspeed.
3. Backscatter from incident angles greater than 20° from the vertical monotonically increases with increasing windspeed.

A representation of these three features of ocean backscatter as a function of windspeed and incident angle for 2- to 3-cm wavelength radar illumination is shown in figure 3–48. For windspeeds less than 1 m/sec, essentially no sensible backscatter is seen at any angle of incidence; the strong radar return at 0° incident angle is from specular mirror reflection (shown as a dotted line). As the windspeed increases toward 2 m/sec, patches of roughness begin to appear on the surface where turbulent gusts at the surface exceed the threshold for wind-to-water coupling. The small capillary waves generated by these gusts produce some backscatter at all angles of incidence with very rapid rates of change of backscatter as compared to windspeed.

At windspeeds above approximately 1.5 m/sec, the total surface is essentially covered with wind-driven capillary waves from which the large waves will grow. The approximate magnitude of backscatter cross section at 0° and 55° incident angles in figure 3–48 has been formed from good, but sparse, data taken between the extremes of approximately

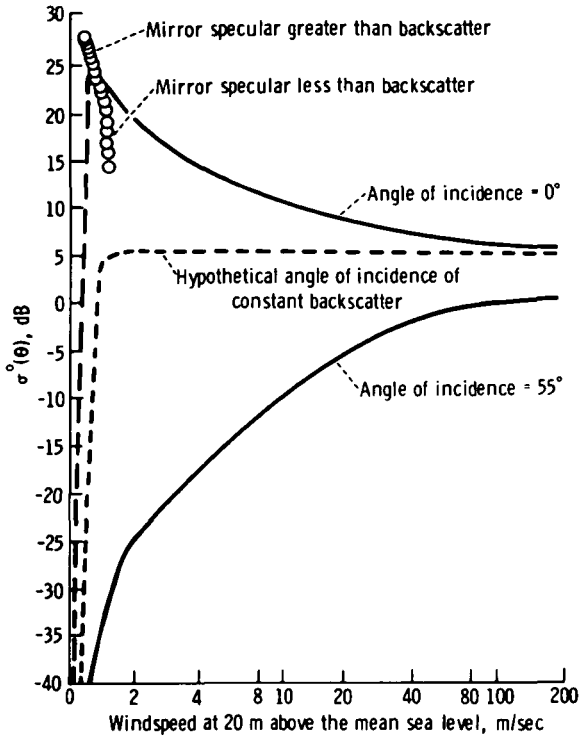


FIGURE 3–48.—Representation of approximate magnitude of backscatter cross section from the ocean at 2- to 3-cm radar wavelengths.

2- to 30-m/sec windspeeds. The continuation of the curves beyond 30 m/sec shows that the monotonic changes in backscatter cross section initiated at low windspeeds probably do not stop abruptly but become very slight at higher windspeeds. The local slope of the curves at high windspeeds shows that extremely accurate measurements of the backscatter must be made to sense small-percentage changes in windspeeds, but this accuracy is required over only a small range of backscatter values. Alternatively, the local slopes at low windspeeds show that less-accurate measurements are required to sense small-percentage windspeed changes.

The set of curves for backscatter is compared to windspeed at all angles of incidence between 0° and 55° lies between the curves shown in figure 3–48, being far apart at low windspeeds and close together at high windspeeds.

Because the change of backscatter compared to windspeed has a change in sign at some incident angle between 0° and 20°, a hoped-for discovery would be an incident angle for which the backscatter cross section is constant for all windspeeds. This constancy would provide a natural reference backscatter cross section and eliminate the requirement for absolute backscatter cross-section measurements for windspeed measurements. The dashed line in figure 3–48 shows that this hoped-for "hypothetical incident angle of constant backscatter" lies at approximately the average level of the backscatter as compared to windspeed for incident angles between 5° and 20°.

Other aspects of backscatter measurements present both an opportunity and a problem:

1. The upwind, downwind, and crosswind viewing directions give different values for backscatter cross sections.
2. The sensitivity of backscatter to upwind, downwind, and crosswind viewing directions is different at each incident angle.
3. The sensitivity of backscatter to upwind, downwind, and crosswind viewing angle at each incident angle is also windspeed dependent.

Figure 3–49 shows typical data of this kind. An interesting observation is that the upwind-downwind dependency was predicted and explained rather well 20 yr ago at NRL, assuming specular points as the backscatter mechanism and wave tank measurements of the probability distributions of surface facets as compared to windspeed. These statistics included not only the distributions of surface slope normals but also the distributions of the areas of these specular reflecting surfaces. Because NRL could not measure these same statistics in other directions, the crosswind dependency was not predicted. The problem created by this feature of ocean backscatter is obvious: with perfect instrumentation—that is, no error in the backscatter measurements but no knowledge of the viewing direction with respect to the wind direction—a radar cross-section data spread of many decibels will be obtained. For example, in figure 3–49, a 6-dB spread exists upwind to crosswind at a 13.9-m/sec windspeed, 40° incident angle, with an average backscatter coefficient over all wind heading angles of −10 dB, whereas at a 6.5-m/sec windspeed, the average is approximately −15.5 dB, with an upwind-to-crosswind spread of 4 dB.

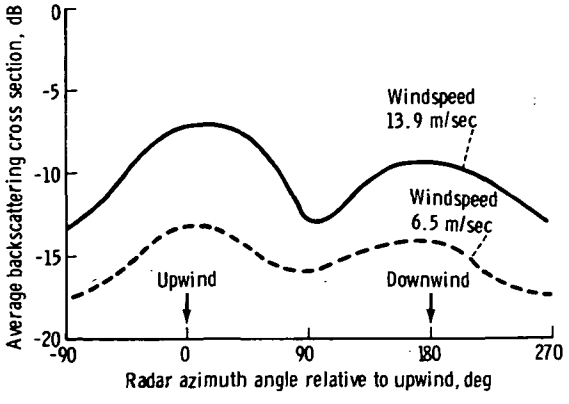


FIGURE 3–49.—Langley Research Center values of $\sigma^\circ$ compared to wind heading (vertical transmit/vertical receive polarization; incident angle of 40°).

This problem can only be solved either by knowing the viewing direction with respect to wind directions or by viewing the surface from enough different directions so that the upwind, downwind, and crosswind curves can be obtained as input data. However, this method represents an opportunity because, with this curve as input data, the wind direction in that resolution cell has also been measured. These resolution-cell data at many incident angles in a swath along the satellite path are required to properly map the windfields over the oceans and/or the pressure fields at the 100 000-N/m$^2$ level.

Scientists working with scatterometry data have recognized and accepted the facts illustrated by figures 3–48 and 3–49 and, finding that the data are repeatable, are starting to design their instruments, data-gathering procedures, and data-processing algorithms to solve the problems and take advantage of the directional data to the extent possible, given the satellite platform constraints.

With proper system design, satellite-borne

scatterometry will provide a majority of the input data required for mapping the windfields over the oceans with refresh times of less than 12 hr.

*Typical scatterometer measurements.*—Radar observations of the scattering cross sections from the ocean surfaces have been conducted for nearly 30 yr. In almost all cases, only the backscattering cross sections have been measured.

The NRL has conducted the most comprehensive measurements of the backscattering cross sections from ocean surfaces (refs. 3–84 to 3–89). These measurements have been conducted at several frequencies and polarization combinations. Both airborne and ground sensors have been used by NRL. A summary of the significant NRL measurements is given in table 3–VII.

The NASA has flown numerous missions with spaceborne and airborne sensors over ocean surfaces (refs. 3–63, 3–90, and 3–91). Scatterometer data have been collected at 0.4 and 13.3 GHz. Spaceborne radar data at 13.9 GHz (Skylab S193) have also been obtained. Backscattering cross-section data have also been collected by LaRC at 13.9 GHz. Table 3–VII also presents a summary of the NASA measurements. Other data, such as those recorded by Newton and Rouse (ref. 3–92), are available.

The interaction of the ocean surface winds and waves is a complex phenomenon. A mathematical model of ocean surface roughness as a function of surface wind velocity is not available. The large volume of the radar-backscattering cross-section data gathered over rough oceans has aided in the understanding of the interaction of waves and winds on the ocean surface. In this section, typical radar-backscattering cross-section data are presented. Problem areas and future efforts for their resolution are also outlined.

Experimental studies of the sea echo at 9.2-, 3.2-, and 1.25-cm wavelengths have been

TABLE 3–VII.—*Available Radar Backscattering Cross Sections Over Water/Ocean Surfaces*

| Type of measurement and organization | Wavelength or frequency | Polarization combinations [a] | Approximate range of angles of incidence, deg | Range of winds or waves |
|---|---|---|---|---|
| Spaceborne experiments: | | | | |
| JSC | 13.9 GHz | VV, VH, HV, and HH | 0 to 53 | 2.1 m/sec to more than 28.3 m/sec. |
| Airborne experiments: | | | | |
| NRL | 0.428, 1.228, 1.25, 4.425, and 8.91 GHz | VV, VH, HV, and HH | 0 to 89 | 2.1 m/sec to 24.7 m/sec. |
| JSC | 13.3 GHz | VV | 0 to 60 | 3.1 m/sec to more than 28.3 m/sec. |
| | 0.4 GHz | VV, VH, HV, and HH | 0 to 60 | |
| | 13.9 GHz | VV, VH, HV, and HH | 0 to 50 | |
| LaRC | 13.9 GHz | VV, VH, HV, and HH | 0 to 50 | 3.1 m/sec to 20.6 m/sec. |
| From platform/bridges: | | | | |
| NRL | 8.6 mm, 1.25, and 3.2 cm | VV | 0 to 80 | 0 to 12.9 m/sec. |
| Wave tank measurements: | | | | |
| NRL | 9.375 GHz | VV and HH | 10 to 86 | Millimeter waves of wavelengths from 1.6 to 6 cm. |

[a] VV=vertical transmit/vertical receive; VH=vertical transmit/horizontal receive; HH=horizontal transmit/horizontal receive; and HV=horizontal transmit/vertical receive.

described by Kerr and Shain (ref. 3–93). These measurements were primarily aimed at studying the frequency dependence of the radar return at higher angles of incidence (grazing angles as much as 4°). The surface winds and waves have not been reported in these measurements.

Measurements of both the ocean-surface contour and the backscattering cross sections were conducted by MacDonald (ref. 3–84). These measurements were conducted at 1.25 GHz with an airborne radar, and the data corresponding to VV and HH polarization combinations were gathered. These data are shown in figure 3–50.

The details of ocean-surface wind, significant wave height, and mean-square slopes are also given by MacDonald (ref. 3–84). At higher angles of incidence (40° to 82°), the radar cross section decreases from −30 to −60 dB. Data given in figure 3–50 show a strong dependence of windspeed with horizontal polarization returns relative to vertical returns. The range of wind velocities for these measurements extended from 0 to 15 m/sec.

The widely quoted experiments by Grant and Yaplee (ref. 3–85) of NRL were performed at wavelengths of 8.6 mm and 1.25 and 3.2 cm; some results are shown in figure 3–51. These data were taken with a bridge-mounted radar system using VV polarizations. The surface wind velocities ranged from 0 to 12.9 m/sec. The height of the radar above the water surface was 50 m.

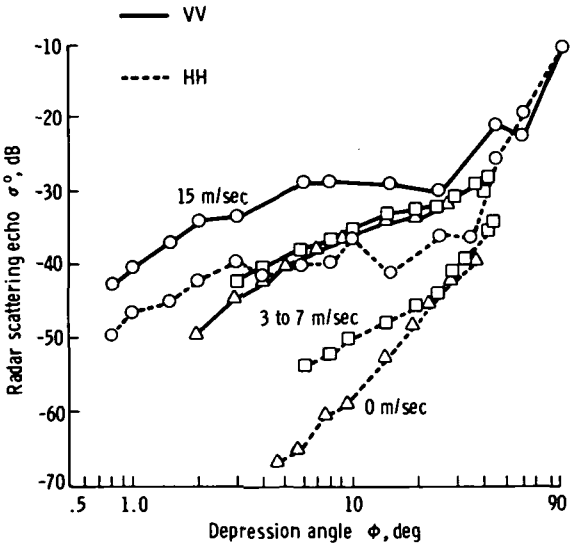


FIGURE 3–50.—Naval Research Laboratory data at 1.25 GHz (ref. 3–84).

These measurements show a rapid decrease in the backscattering cross section as a function of angle of incidence for surface windspeeds below 1 m/sec. At normal incidence for scattering, cross section decreases with an increase in surface wind velocity. For 1.25-cm and 8.6-mm wavelengths, the scattering cross section increases with wind velocity for incident angles higher than 20°.

These measurements do not include the effects of wind direction and winds in excess of 12.9 m/sec on the backscattering cross section. Furthermore, data corresponding to VH, HV, and HH polarizations were not acquired.

From 1964 to 1971, personnel of the NRL acquired numerous sea return data using a single four-frequency airborne radar. The four major measurement programs (refs. 3–64 and 3–86 to 3–89) conducted by NRL were Puerto Rico (1965), North Atlantic (1969), Joint Ocean Surface Study I (JOSS I) (1970), and JOSS II (1971). Surface truth measurements were established by ground-based observations.

A summary of NRL measurements and ground data measurements is given by Daley (ref. 3–64). The NRL measurements are given as the median normalized radar cross section (MNRCS). The scattering cross section per unit area has been defined as normalized radar cross section (NRCS).

To establish the average value of the backscattering cross section $\sigma°$, the probability distribution of the NRCS must be known. For a Rayleigh-distributed NRCS, $\sigma°$ can be computed by adding 1.6 dB to MNRCS. Both theory and experiment have shown that the sea return may have a probability density distribution other than that specified by Rayleigh. Hence, the average-to-median ratio

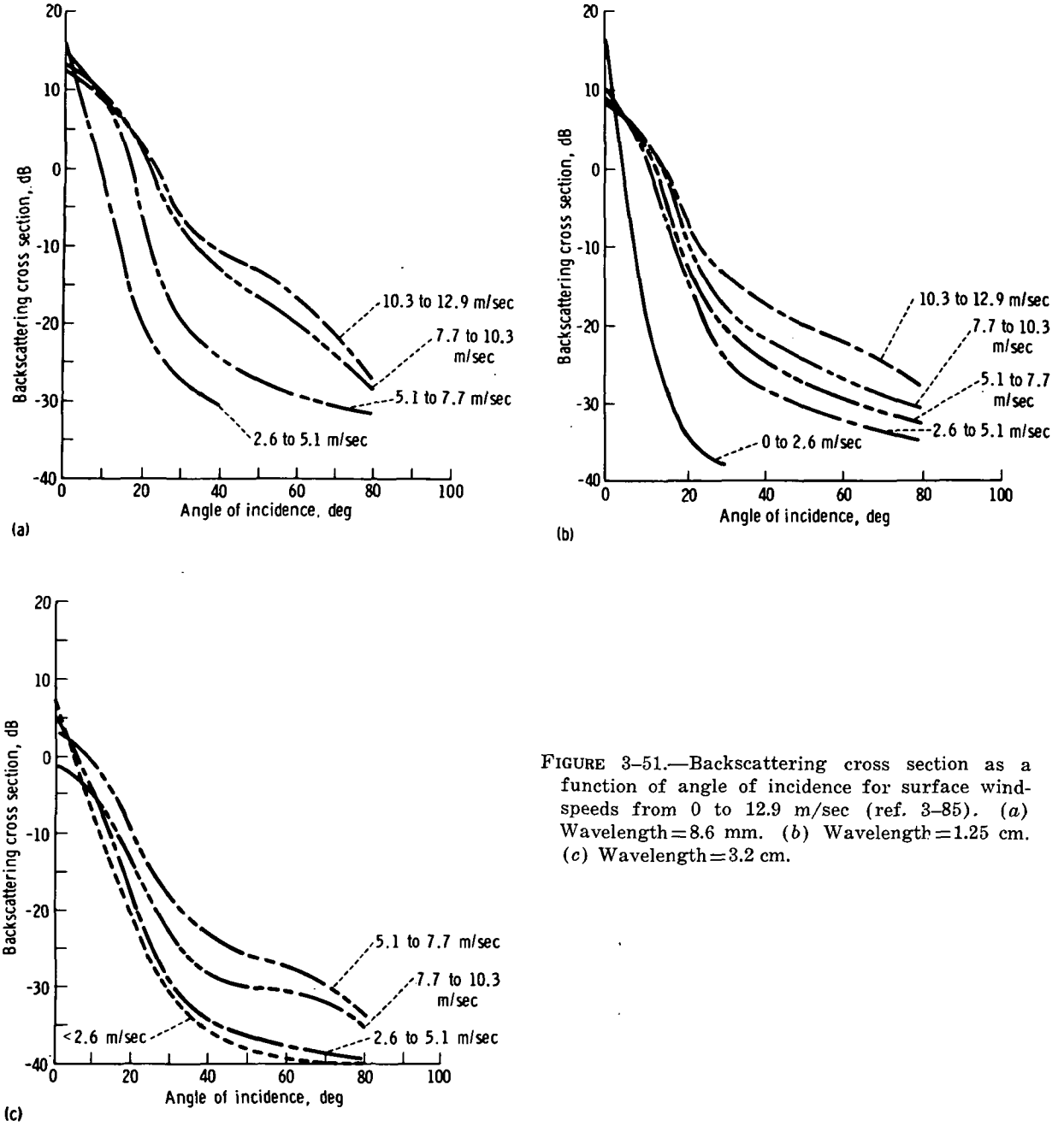


FIGURE 3–51.—Backscattering cross section as a function of angle of incidence for surface wind-speeds from 0 to 12.9 m/sec (ref. 3–85). (*a*) Wavelength=8.6 mm. (*b*) Wavelength=1.25 cm. (*c*) Wavelength=3.2 cm.

may differ from 1.6 dB and depend on the sea-surface roughness.

The previously published data, with the exception of JOSS II (ref. 3–89), do not define the illuminated area in terms of the two-way antenna pattern. Corrections to the NRL data are given by Daley (ref. 3–64). Typical NRL data acquired during the JOSS II mission are given in figure 3–52. The MNRCS decreases with increasing wind velocity at vertical incidence. The NRL measurements have been used to develop models for the frequency dependence of radar-backscattering cross section from the ocean surface. A more recent

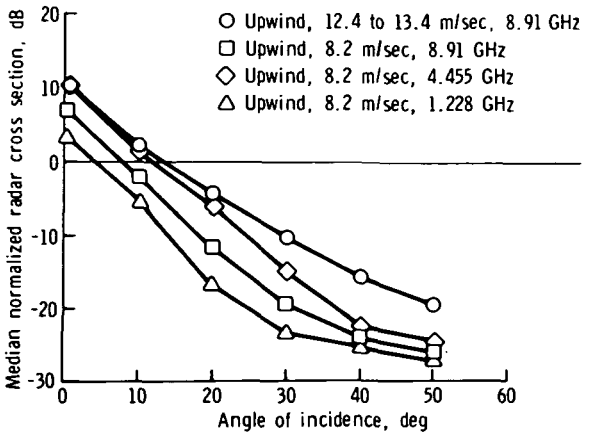


FIGURE 3–52.—Median normalized radar cross section as a function of incident angle for various frequencies and windspeeds (vertical transmit/vertical receive polarization).

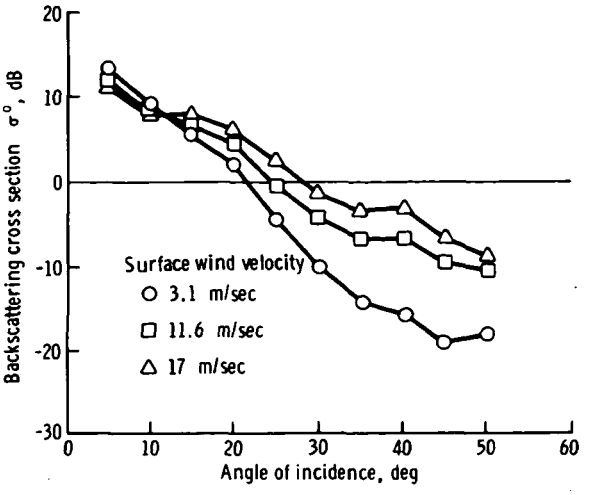


FIGURE 3–53.—Backscattering cross section as a function of angle of incidence for 13.3-GHz scatterometer for mission 119 (vertical transmit/vertical receive polarization).

analysis of NRL data shows correlations between surface wind velocity and the normalized radar cross section. Backscattering from capillary waves has also been investigated by NRL (ref. 3–94).

During a period of several years, many aircraft missions have been flown by NASA JSC to study the dependence of radar return on such parameters as local windspeed, wind direction, and the spectrum of the sea. Data have been collected using scatterometers at frequencies of 0.4, 13.3, and 13.9 GHz. Extensive surface truth has been compiled, including wind and wave measurements. Airborne laser profilometers were used to measure sea-surface spectra. Photographs of the ocean and clouds are also available for detailed correlation analysis. For the 0.4- and 13.3-GHz scatterometers, the data are collected simultaneously for incident angles between 60° and −60° (ref. 3–95) by using coherent Doppler wave techniques.

The digital-processing program yields the backscattering cross section as a function of the angle of incidence. The typical backscattering cross sections for 13.3 GHz are given in figure 3–53 (ref. 3–63). These data are for NASA JSC mission 119. For the 13.3-GHz scatterometer, a strong dependence of the backscattering cross section on surface-wind velocity has been shown (ref. 3–61).

The NASA 13.9-GHz RADSCAT (also known as AAFE RADSCAT) is a multiple-polarization system. Data corresponding to VV, HH, VH, and HV polarization combinations and radiometer vertical- and horizontal-polarization data (ref. 3–96) can be collected. The system antenna can be moved automatically, corresponding to 0°, 10°, 20°, 30°, 40°, and 50° pitch angles, or can be manually adjusted at each of these angles. Figure 3–54 is a typical example of the data gathered over ocean scenes using this system.

The most recent addition to active microwave measurements over ocean scenes has been the data acquired with Skylab S193 operated in several modes both in-track and crosstrack (ref. 3–97). Scatterometer data corresponding to VV, VH, HH, and HV polarization states were gathered. An altimeter was also used to collect backscattering cross-section data to approximately a 16° incident angle.

Ocean-surface measurements were made simultaneously for detailed data analysis, and data have been gathered over oceans having calm to hurricane conditions. Examples

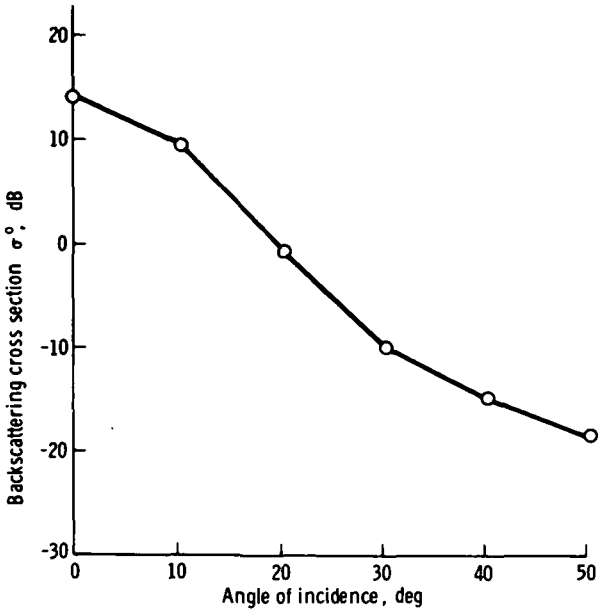


FIGURE 3–54.—Backscattering cross section as a function of incident angle for a 13.9-GHz aircraft RADSCAT (upwind: 6.7 m/sec; vertical transmit/vertical receive and horizontal transmit/horizontal receive polarizations).

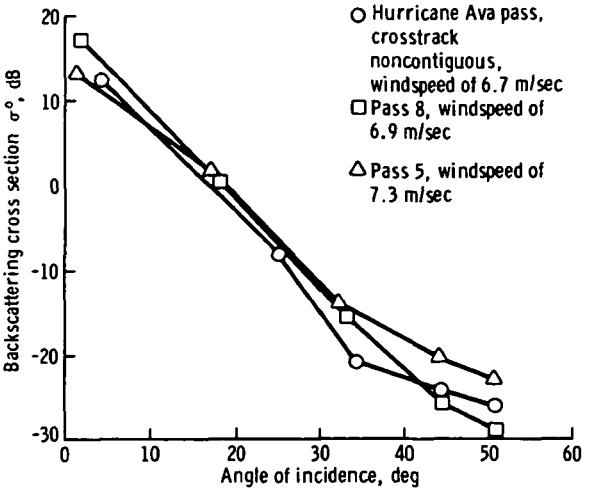


FIGURE 3–55.—Comparison of S193 scatterometer backscattering cross sections for EREP passes 5 and 8 and Hurricane Ava pass.

of S193 data are given in figures 3–55 and 3–56. In these figures, Earth Resources Experiment Package (EREP) (passes 5 and 8) and Hurricane Ava data are given. The S193 scatterometer data show a strong dependence on ocean-surface wind velocity.

*Relationship between backscattering cross sections and ocean-surface wind velocity.*— This section summarizes significant results in the investigation of the correlation between radar backscattering coefficient $\sigma^\circ$ and the ocean-surface windspeed $W$. This correclation has been investigated intensively during the past decade (refs. 3–63, 3–89, 3–91, 3–92, and 3–96) and much $\sigma^\circ$ data have been acquired by using airborne and spaceborne sensors. The major sources of active microwave data are NRL, JSC, and LaRC.

The relationship between $\sigma^\circ$ and $W$ is currently being investigated. However, certain conclusions have been made based on aircraft- and spacecraft-acquired data analysis:

1. For angles of incidence beyond about 25°, the backscattering cross section increases with windspeed to 25 m/sec of wind for 13.3-, 24-, 1.25-, 13.9-, 4.455-, and 8.91-GHz frequencies.

2. Near and at vertical incidence, the scattering cross section decreases with surface windspeed. This fact has been observed at all frequencies thus far investigated.

The remote sensing of ocean-surface winds can be more effectively accomplished by measuring the ratio $Q_0$ defined by Krishen (ref. 3–63).

$$Q_0 = \frac{\sigma^\circ \text{ at or near vertical}}{\sigma^\circ \text{ at or near } 45^\circ \text{ incident angle}} \qquad (3\text{–}14)$$

The investigation of the winds over oceans can be divided into two parts for remote sensors: windspeed and wind direction. Detection of windspeeds using active microwave sensors has been done successfully, but little has been accomplished concerning the wind direction detection. The prediction of wind detection has been investigated by LaRC (ref. 3–96). This aspect of the problem still requires more research.

To study the effect of the wind on the backscattering cross section, the directional spectrum of the high-frequency gravity-capillary

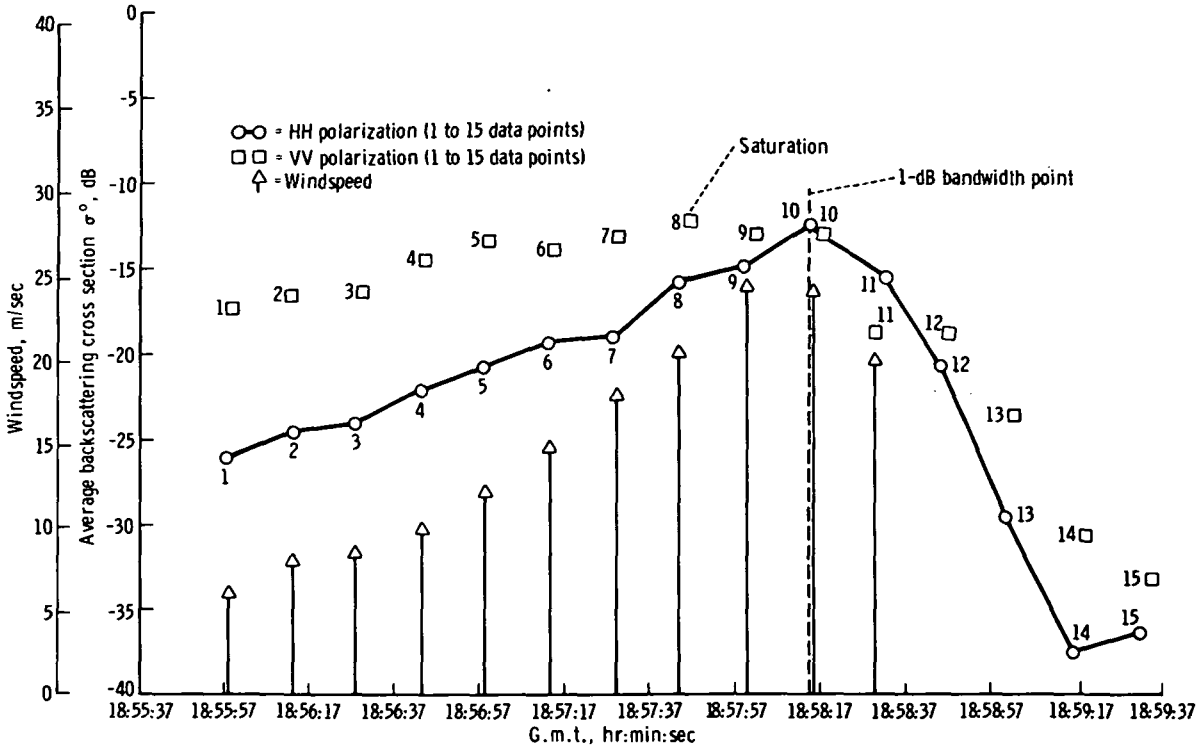


FIGURE 3–56.—Skylab S193 backscattering cross section as a function of time (roll angle of 46.6°; incident angle of 50.7°; Hurricane Ava pass). Data points 1 to 13 refer to locations in figure 3–59.

structure of the sea could be expressed as

$$W(Z) = kZ^{-k_3} \qquad (3\text{–}15)$$

where $k$ and $k_3$ are constants, $Z = (p^2+q^2)^{1/2}$, and $p$ and $q$ are radian wave numbers on the ocean surface.

At higher angles of incidence, the backscattering cross section can be expressed, in part empirically and in part caused by scattering from a small gravity-capillary structure, as (ref. 3–63)

$$\sigma^\circ{}_{ij}(\theta) = k_1 W^{k_2} |\alpha_{ij}|^2 \cos^4\theta \ (\text{cosec}\,\theta)^{k_3} \qquad (3\text{–}16)$$

In equation (3–16) $\alpha_{ij}$ is defined as

$$\alpha_{HH} = \frac{\epsilon - 1}{(\cos\theta + \sqrt{\epsilon - \sin^2\theta})^2} \qquad (3\text{–}17a)$$

$$\alpha_{VV} = \frac{(\epsilon-1)\,[(\epsilon-1)\sin^2\theta + \epsilon]}{(\epsilon\cos\theta + \sqrt{\epsilon-\sin^2\theta})^2} \qquad (3\text{–}17b)$$

$$\alpha_{VH} = \alpha_{HV} = 0 \qquad (3\text{–}17c)$$

where $\epsilon$ is the complex dielectric constant of the surface and $k_1$ and $k_2$ are constants ($k_1$ is related to constant $k$).

The cosec $\theta$ form given in equation (3–16) can be simplified and expressed in cot $\theta$ form as (ref. 3–63)

$$\sigma^\circ{}_{ij}(\theta) = k_1 W^{k_2} |\alpha_{ij}|^2 (\cot\theta)^{k_3} \qquad (3\text{–}18)$$

In figure 3–57, the experimental and calculated data (using eq. (3–14)) for upwind mission 119 NASA JSC 13.3-GHz data are shown. The values of constants are $k_1 = 0.026$, $k_2 = 1.324$, and $k_3 = 5.47$.

Table 3–VIII is the 1.25-cm data reported by Grant and Yaplee (ref. 3–85). The values of $k_1$, $k_2$, and $k_3$, using cot $\theta$ form, are $k_1 = 0.00107$, $k_2 = 1.64$, and $k_3 = 5.03$.

These studies have also demonstrated that scatterometers can be used to determine the directional spectrum of small gravity and

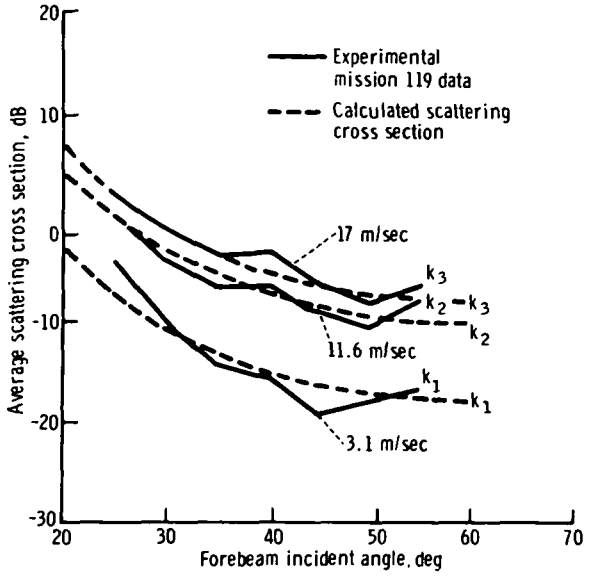


FIGURE 3–57.—Comparison of calculated and experimental scattering cross section for mission 119.

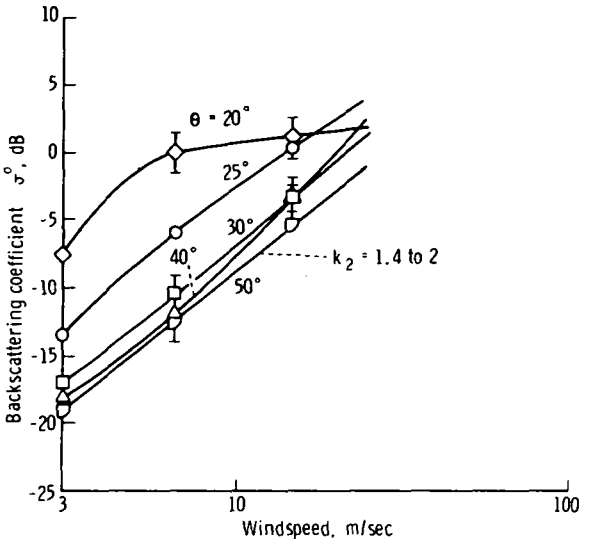


FIGURE 3–58.—Langley Research Center values of backscattering coefficient as a function of windspeed (frequency of 13.9 GHz; vertical transmit/vertical receive polarization; downwind).

capillary waves at various surface-wind velocities.

Measurements by NRL have also been analyzed to determine dependence of $\sigma^\circ$ on $W$. The values of $k_2$ are somewhat smaller (ranging from 0.2 to 1.9) compared to the values for NASA data. However, the operating frequency of NASA scatterometers (13.3 GHz) is higher than for NRL radar.

The LaRC has acquired 13.9-GHz data for various windspeeds. The values of $k_2$ for these data (ref. 3–96) range from 1.4 to 2.0 (fig. 3–58).

From the data shown in figure 3–58, the measured power factor $k_2$ apparently lies somewhere between 1.4 and 2.0 at those incident angles at which the radar return is dominated by the capillary wave structure. Initially, this may appear to be a trivial range of uncertainty. Nevertheless, many arguments have been generated among various groups because the value of $k_2$ and the instrument characteristics essentially define the accuracy and the upper limit on the measurement of windspeed.

TABLE 3–VIII.—*Backscatter as a Function of Mean Windspeed and Angle for the 1.25-cm VV Case*

| Mean windspeed, m/sec | Backscatter, dB, for— | | | |
|---|---|---|---|---|
| | $\theta$=20° | $\theta$=30° | $\theta$=40° | $\theta$=50° |
| 3.9 .... | −14.0 | −25.0 | −28.75 | −31.10 |
| 6.4 .... | −12.4 | −21.25 | −25.00 | −27.60 |
| 9.0 .... | − 9.0 | −17.8 | −22.5 | −24.4 |
| 11.5 .... | − 7.5 | −14.2 | −17.5 | −20.2 |

The Skylab EREP Hurricane Ava pass provides backscattering cross sections for a wide range of wind velocities. A quick-look evaluation (refs. 3–98 and 3–99) of the Hurricane Ava data shows a strong dependence of $\sigma^\circ$ on the wind velocity. The S193 RADSCAT gathered data in a crosstrack (right only) mode for nominal pitch angles of 0°, 15.6°, 29.4°, 40.1°, and 48°. The actual angles attained by the S193 antenna differed from these nominal angles.

The highest pitch angle data (average 46.6°) were taken from approximate areas shown in figure 3–59. The photograph was prepared by NOAA.

The scatterometer data corresponding to average roll angles of 31.35°, 40.61°, and

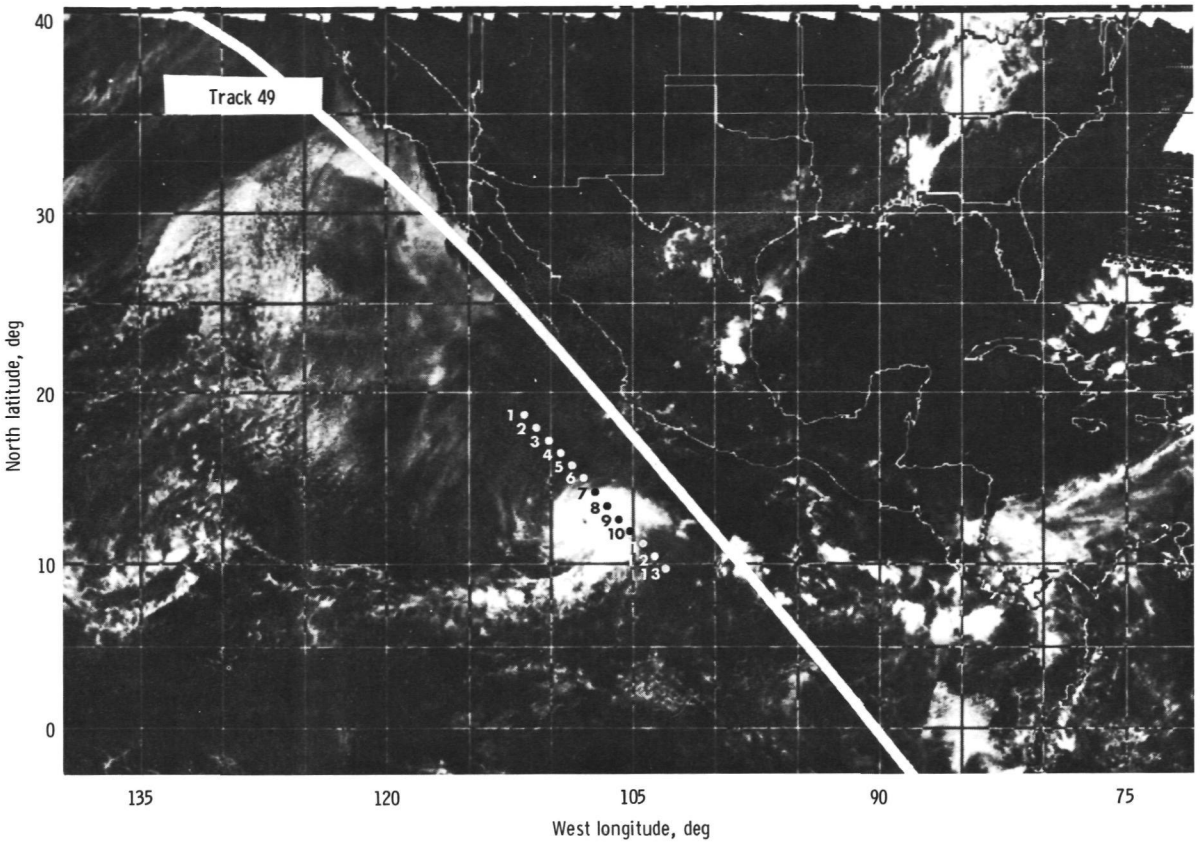


FIGURE 3–59.—Composite photograph showing approximate locations, from north to south, of 13 of the data points plotted in figure 3–56.

46.6° are given in figures 3–56 and 3–60 as a function of time. The wind velocities in these figures were taken from the report prepared by Hayes et al.[4]

During this pass, Skylab was in the solar inertial mode. The data drop after G.m.t. 18:58:17 is due to attenuation by the 0° Doppler filter. The dashed line marked 1-dB bandwidth point corresponds to a Doppler filter attenuation of 1 dB. No Doppler filter corrections have been done for the data given in these figures. In figure 3–59, locations of points 1 to 13 of figure 3–56 have been shown.

To study the wind dependence for data presented in figures 3–56 and 3–60, a function of the form

$$\sigma^\circ = k_1 W^{k_2} \qquad (3\text{–}19)$$

was used. A least-mean-square fit yields the following results (ref 3–98):

1. For the average roll angle 31.35°, $k_2 = 0.65$.
2. For the average roll angle 40.61°, $k_2 = 0.60$.
3. For the average roll angle 46.6°, $k_2 = 1.89$.

This wind dependence has been investigated for the data only to G.m.t. 18:48:17; the wind direction was very nearly downwind for these data points. No atmospheric corrections were made to the data.

*Problem areas.*—The comparison of backscattering cross sections from the various ex-

[4] Hayes et al.: A Preliminary Analysis of the Surface Truth Data To Be Correlated With the Skylab 2 Data Obtained for S193 Microwave Investigators. Informal report prepared for NASA JSC under contract NAS9–13642, Aug. 1973 (unpublished data).

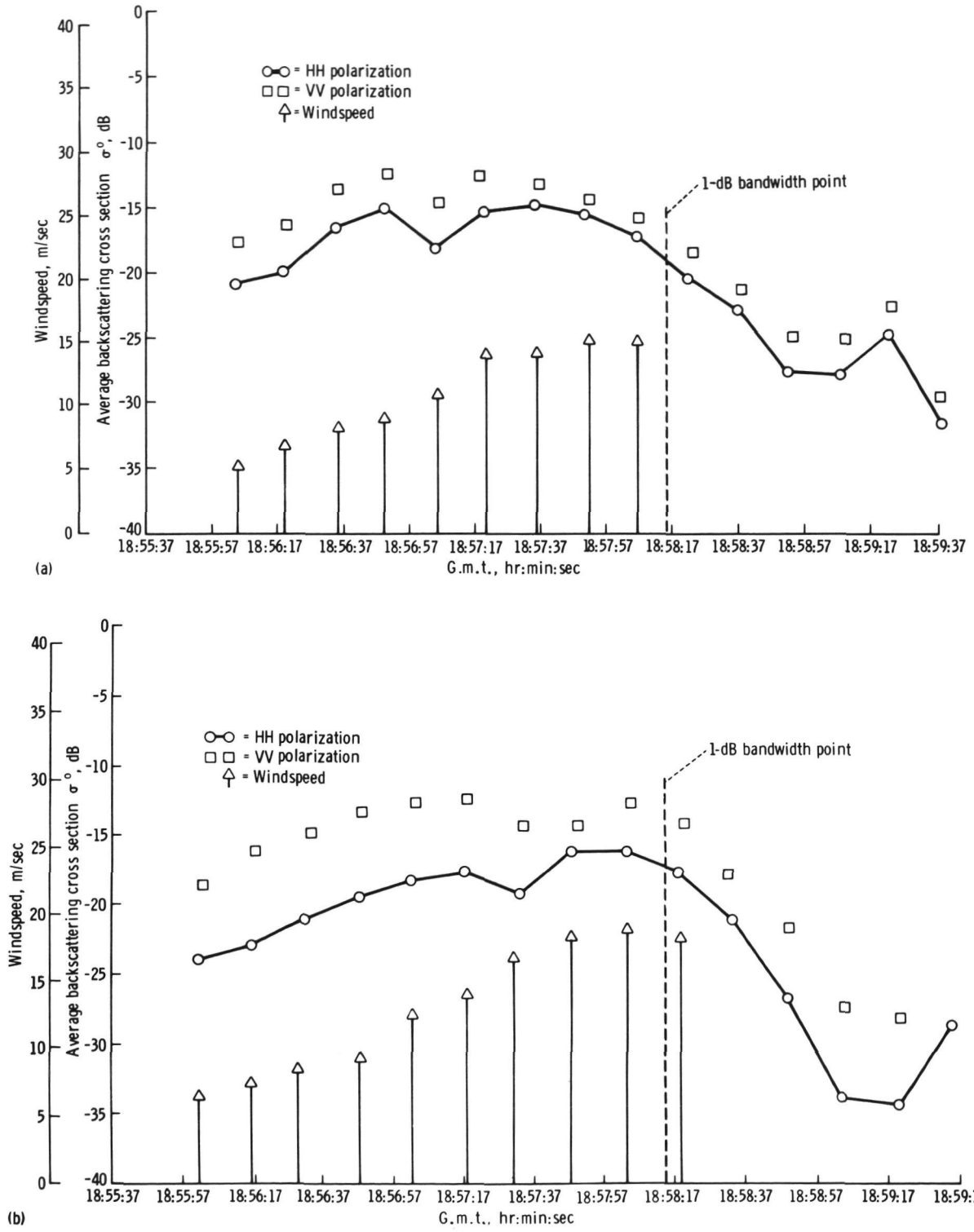


FIGURE 3–60.—Skylab S193 backscattering cross section as a function of time for Hurricane Ava pass. (*a*) Roll angle=31.35°; incident angle=33.92°. (*b*) Roll angle =40.61°; incident angle=43.8°.

periments reveals a wide spread of values under supposedly indentical ocean conditions. This disagreement has caused concern within the community of applications investigators. The sources of disagreement cannot easily be identified, and many of them still remain unknown. Common sources of disagreement fall within the following categories.

Description of the sea: The sea surface and its environment are a complex phenomenon. The identification of the ocean scene has not been given adequately in a majority of experiments. Ocean-surface data (sea spectra, surface-wind velocities, fetch, duration, effect of distant storms, surface contaminants, etc.) and intervening medium data (temperature, pressure, moisture, cloud cover, rainfall rate, spray, etc.) have not been fully specified. Even for the cases in which these data are partially given, the accuracies of the measurements and the methods of data processing differ greatly. For example, the height at which the surface winds are measured differ between experiments.

System and calibration problems: A thorough evaluation of the systems used for measuring ocean backscattering cross sections has not been reported in many investigations, and the precision and accuracy of the radar system has been neither measured nor documented. One-time determination of precision and accuracy is not sufficient because these measurements should be performed just before or after data have been collected with the system. The usual difficulties are encountered in accurate calibration for an absolute measurement of the radar cross section. The calibration methods for various radars differ significantly.

Platform perturbations: The changes in the attitude of the aircraft or spacecraft cause errors in the measurements. In many investigations, the effects of platform attitude variations are not properly compensated. Furthermore, the relative direction of flight should be properly maintained with respect to the known surface-wind vector for experimental aircraft missions. Otherwise, an unknown bias may be added to the data, as illustrated in figure 3–50.

Data collection and processing techniques: Subtle differences are observed in data collection techniques among various investigations. The extent of averaging of the data differs for various experiments. When several hours are required for collection of $\sigma^\circ$ as a function of angle-of-incidence data, the wind velocities may have changed direction significantly. When large areas are averaged, a nonuniform windfield could exist.

The algorithms used for processing the data differ in many cases. In several investigations, the value of backscattering cross section is referenced to an arbitrary number.

*Future research and development.*—The performance of NASA 13.3- and 13.9-GHz scatterometers has been fully demonstrated by aircraft and Skylab missions. However, these systems were basically experimental. These programs have indicated a need for improving both hardware and software capabilities. Also, procedures for collecting the data should be revised for an operational system.

The decade ahead requires systems that can be run reliably for extended periods of time. Also required are computational techniques that will automatically yield backscattering cross-section data without manual processing. To achieve this goal, the following recommendations for research and development are given:

1. Improved radar calibration techniques: After each data collection period, a calibration period should follow. The frequency of these calibrations will depend on the performance of the system. Some technique of external calibration should be adopted. Corner reflectors over smooth deterministic targets can be used for airborne and spaceborne scatterometers. Internal calibrations are undesirable because they do not involve all the paths through which the actual returned energy goes.

2. Improved systems design: Improvements are needed in the reliability of the antenna pointing, switching logic, and polariza-

tion isolation. System drifts, resolution, and noise-level fluctuations must be reduced in future airborne and spaceborne systems.

3. Data-processing techniques: For operational systems, highly efficient data-processing techniques are needed; no reliable data display techniques have yet been advanced. Onboard processing of the data should be explored, and the digitally processed data should be color coded to display ocean winds and waves for visual interpretation and use. These programs should be capable of processing large volumes of reflectivity data and displaying these data on a world map.

4. Calibration data measurements: For spaceborne and airborne instruments, the calibration data corresponding to each subsystem are usually measured in the laboratory. The amplifier, mixer, and filter gains are some examples. For instruments flown for extended periods, these internal gains change with time. To alleviate this problem, automatic calibration modes should be designed to check all calibration data needed to calculate backscattering cross sections from raw data.

### Imaging Radars

An imaging radar has been selected as one of the active instruments for the SEASAT–A payload. An imaging radar was flown in space during the Apollo 17 mission, when the Apollo lunar sounder experiment used synthetic aperture techniques to map the lunar surface and to sound the near-lunar subsurface. Imaging radars have been flown on numerous aircraft and have detected several ocean surface and ice phenomena that are of interest to oceanographers.

Almost all ocean and ice mapping requirements can be fulfilled with radars using synthetic aperture techniques from satellites or with radars using synthetic or real aperture techniques from aircraft. The width of surface imaged from an aircraft platform is approximately 10 to 20 km. However, the width imaged from spacecraft can be 1 to 200 km, which is comparable to the width of an ERTS photograph. Aircraft platforms can be either dedicated aircraft or commercial aircraft. Dedicated aircraft have the advantage of being the most flexible for observation, parameter modification, and target selection. Radars carried aboard commercial aircraft could provide quasi-global coverage, particularly when there are no imaging radars in space. Spacecraft are the only way to obtain global coverage, which is vitally important to the monitoring of wave climatology and polar ice. The tradeoffs between aircraft and spacecraft are discussed further in this section.

The use of either spacecraft or aircraft imaging radars is suggested for the following research and application programs:

1. The mapping of ocean-wave buildup in storms.
2. The global monitoring of ocean-wave spectra.
3. The mapping and monitoring of oil slicks.

*Imaging radar observables.*—The use of imaging radars for oceanographic observations has been generally overlooked, although these radars have been flown in numerous configurations and over numerous portions of the Earth. However, the following phenomena have appeared in existing imagery.

1. Ocean waves with wavelengths of 50 m or more.
2. Ocean-wave diffraction patterns near shores and structures.
3. Oil-slick patterns caused by internal waves.
4. Slicks from oil and/or freshwater.
5. Ocean-wave differences at current boundaries.
6. Kelp beds.
7. Sea ice cover (floes, leads, polynyas, and ridges).
8. Ocean-wave attenuation in shallow areas.
9. Lake ice cover (floes, leads, polynyas, ridges, and estuary ice cover).

Thus, the imaging radar apparently senses two different aspects of the ocean surface: the longer gravity waves, which disturb the ocean surface with scales larger than the ra-

dar resolution; and the relative abundance of very small capillary waves, which disturb the ocean surface with scales near the radar wavelength.

*Some instrumental constraints.*—A primary requirement for imaging radars is that they be carried on aircraft or spacecraft platforms. These moving platforms provide the motion that carries the radar past the target so that its Doppler history can be mapped to a single point (synthetic aperture) or so that the target is backscattering for only a short period when it is in a narrow antenna beam (real aperture).

An aircraft platform is advantageous because radars can be varied and the observation area can be easily targeted. Radar parameters such as wavelength can be as short as approximately 1 cm and as long as a few meters, and resolutions and polarizations can be changed with moderately little difficulty.

Investigators at JPL have developed a multifrequency synthetic aperture radar that operates at wavelengths of 3.5 and 25 cm and 2 m, with a nominal resolution of 10 to 30 m. This JPL radar is configured to operate on the NASA CV–900 operated by the NASA Ames Research Center. Another aircraft dedicated to active radar experiments would be a valuable asset to ocean, ice, and other observations. The primary advantage of the dedicated aircraft would be the ability to target its observation area and to allow targets to be imaged at different angles of incidence. Jet aircraft fly at altitudes of slightly less than 15 km; thus, image swath widths could be 15 km either side of the aircraft.

Aircraft platforms for imaging radars can also be provided by large commercial jets, which routinely fly regular routes. Using spacecraft construction techniques, an imaging radar would have low weight, power, and volume. The NASA has developed other nonradar instruments to be carried aboard commercial aircraft. If this commercial aircraft were flown on ocean routes, oceanographers would be provided with ocean-wave spectra across an ocean basin. If this commercial aircraft were flown over the North Pole, daily images of sea ice could be obtained to help monitor ice motion. Imaging radars operating daily on a commercial aircraft could provide valuable quasi-global radar images during the next decade when global monitoring by spaceborne imaging radars is not possible. This period would occur before SEASAT–A is operating, several years after SEASAT–A is shut down, and before Space Shuttle follow-ons are launched and operating.

Satellites and the Space Shuttle will provide the only platforms for truly global coverage. In addition, spaceborne imaging radars can have swath widths of 1 to 200 km and will provide imaging capabilities similar to ERTS space photography. Spacecraft platforms for imaging radars in the 1970's and 1980's include the automatic unmanned SEASAT–A, presently scheduled for launch in 1978; the manned adaptable Space Shuttle Spacelab missions, scheduled for launch in the early 1980's; and Space Shuttle launched, automatic, and unmanned spacecraft, scheduled for launch in the late 1980's. Current plans for SEASAT–A operating parameters are given in table 3–IX.

In summary, both aircraft and spacecraft platforms are needed for radar imaging of ocean and ice phenomena. Aircraft have swaths as much as 15 km but can be easily targeted to areas of interest, if an aircraft is dedicated to active microwave remote sensing. Quasi-global coverages can be obtained with radar images carried aboard commercial aircraft, which will provide valuable data when no spacecraft are in orbit. Radar imagers on spacecraft have the advantage of providing global coverage with wide swaths of 200 km, which yield imagery like that obtained at optical wavelengths by the ERTS spacecraft.

Finally, a need exists for a real aperture radar imager that could be carried on a slow-moving or stationary lighter-than-air ship or that could be stationed on land. This type imager would be extremely valuable for mapping oil slicks that are fairly local and generally slow moving and that may not easily

be imaged by the fast-moving platforms needed for the other ocean and ice phenomena.

*Research problems and applications.*—The research problems addressable by imaging radar techniques are generally related to (1) ocean waves and their behavior in storms and near currents, shorelines, and structures; (2) behavior of oilspills under the influence of winds and currents; and (3) sea and lake ice dynamics and iceberg motion.

Ocean surface waves: The imaging radar is the only instrument presently existing that can provide maps of the behavior of ocean waves under heavy cloud cover in storm conditions. Tropical cyclones and high-latitude storms generate wavefields of great destructive capability at precisely those times when wave information is most difficult (if not impossible) to obtain. The radar is a promising instrument for providing these data. Present indications are that a spaceborne or airborne radar with 10-m resolution can image wavefields in all wavelengths from approximately 20 m in length to some unknown upper limit. Images of wave systems and amplitude measurements are required when the wave patterns change appreciably in space. This requirement is also needed near hurricanes and storms or in the vicinity of shorelines, jetties, harbor mouths, and offshore structures. Similarly, images are useful near current boundaries such as the Gulf Stream.

TABLE 3–IX.—*SEASAT-A Imaging Parameters*

| | |
|---|---|
| Wavelength, cm | 21.4 |
| Frequency, GHz | 1.3 |
| Swath width, km | 10 000 and 200 |
| Image length, km | 10 to 100 |
| Nadir angle at beam center, deg | 20 |
| Angle of incidence at beam center, deg | 22 |
| Surface resolution: | |
| Swath of 10 or 100 km, m | 25 by 25 |
| Swath of 200 km, m | 100 by 200 |
| Signal-to-noise at beam center, dB | 10 to 15 |
| Orbital altitude, km | 800 |
| Orbital inclination, deg | 108 |

In the open ocean, images by themselves may not be required; instead, a spectral description is adequate for the spatial homogeneity. The desired quantity is the distribution of wave energy among various wavelengths propagating at varying angles (i.e., the two-dimensional power spectral density). The current thinking is that imaging radar probably gives the slope spectrum rather than the amplitude. These two spectra are related by simple algebraic transformations.

Oilspills: Because of the damping effect of oils on capillary wave structure, oilspills (both natural and manmade) should be visible on imaging radar pictures. For example, it should be possible to assay the existing amount of surface oil cover in a region such as the eastern Gulf of Mexico, which will soon be opened for oil exploration and drilling, and, once in possession of these baseline data, determine if significant increases in that coverage have occurred because of the drilling operations. Furthermore, the drift of oilspills under the influence of currents and winds may be observed, especially in bad weather. This observation is probably best accomplished from aircraft optimized for coastal zone viewing.

Sea and lake ice dynamics and iceberg motion: The discussion related to polar, sea, and lake ice dynamics and the iceberg motion study using a SLAR is given in the section of this chapter entitled "Polar Ice Fields."

*Recommendations: imaging radars.*—In the first few years of the 1970's, the potential benefits of observing ocean and ice phenomena with a spacecraft imaging radar have been established by many programs, which have shown that ocean wave and ice patterns, forms, and structures appear in radar images. In the remainder of the 1970's and in the 1980's, imaging radars will be flown on SEASAT and the Space Shuttle. For the SEASAT and Space Shuttle missions, the first missions to carry imaging radars in Earth orbit, the radar parameters are being established by well-organized and well-operated programs of user/instrumenter interactions, such as the SEASAT user and instru-

ment working goups. No doubt exists that these early imaging radars will observe and measure interesting and important ocean and ice phenomena.

The scientific and application values of these radars can be further enhanced by careful surface-truth verifications. These surface-truth programs are presently underway and must be continued throughout the 1970's and 1980's. For imaging radars, it is very important to establish the physical surface mechanism of ocean waves that modulates the echo power and to establish the relationship that will convert a two-dimensional transform of a radar image into a two-dimensional wave spectrum. Also, the monitoring of wave buildup in large storms is very important. Ice observation programs must be continued so that the relationship between radar and echo and ice form can be established.

*Measurement characteristics.*— Experiments concerning nanosecond radar returns from the ocean surface have been conducted by NRL from a fixed tower in Chesapeake Bay, from ships, and from aircraft (ref. 3–100).

The ability of the radar to profile is shown in figure 3–61. The upper trace is a laser profile of sea surface taken along the aircraft groundtrack. The bottom trace was obtained simultaneously by an NRL nanosecond radar. In this comparison, the spot size of the laser was approximately 0.05 by 1 m, and the spot size of the radar was approximately 10 m.

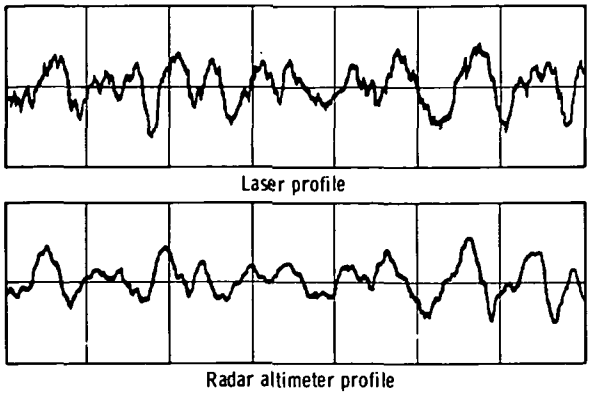


FIGURE 3–61.—Radar ocean profile return.

The poorer resolution of the radar does not affect its ability to return significant information on the vertical structure of the sea surface. The only information lost by the use of 10-m resolution is basically from the shorter water waves and capillary waves, which contain only a small percentage of the entire energy of the wave spectrum. In the surface contour radar, the average of a set number of returns would provide the range from the aircraft to the spot on the ocean illuminated by the radar. As the radar is scanned crosstrack, it will provide a crosstrack profile of the sea surface. As the aircraft advances downrange, successive crosstrack profiles are recorded, which produce a three-dimensional plot of the ocean surface.

*Experimental apparatus.*—A block diagram of the surface contour radar is shown in figure 3–62. The ranging circuitry would consist of a discriminator, a range-time to pulse-height converter, and a low-pass filter. The output of this circuitry would be a plot of range time, which is equivalent to vertical sea structure as compared to clock or experiment time. These data would then be digitized and stored on tape. All the components shown in figure 3–62 and the components of the ranging capability are readily available.

The elliptical wobble plate, which would be approximately 50 cm in diameter, would be mounted in the lower portion of an aircraft fuselage, although not so low as to be within the airstream. The 10° off-nadir scanning would not require significant modifications to the fuselage of the aircraft.

*Physical parameters of the experiment.*— Typical values of parameters for the proposed experiment are given in table 3–X. The proposed experiment could use commercially available components. A reasonable estimate for the total volume of the experiment would be 6 $m^3$, with approximately one-fourth of this volume located in the lower part of the fuselage. No particularly difficult power, data rate, or interface requirements are presented by this experiment, which should be easily accommodated in the NASA Wallops Flight

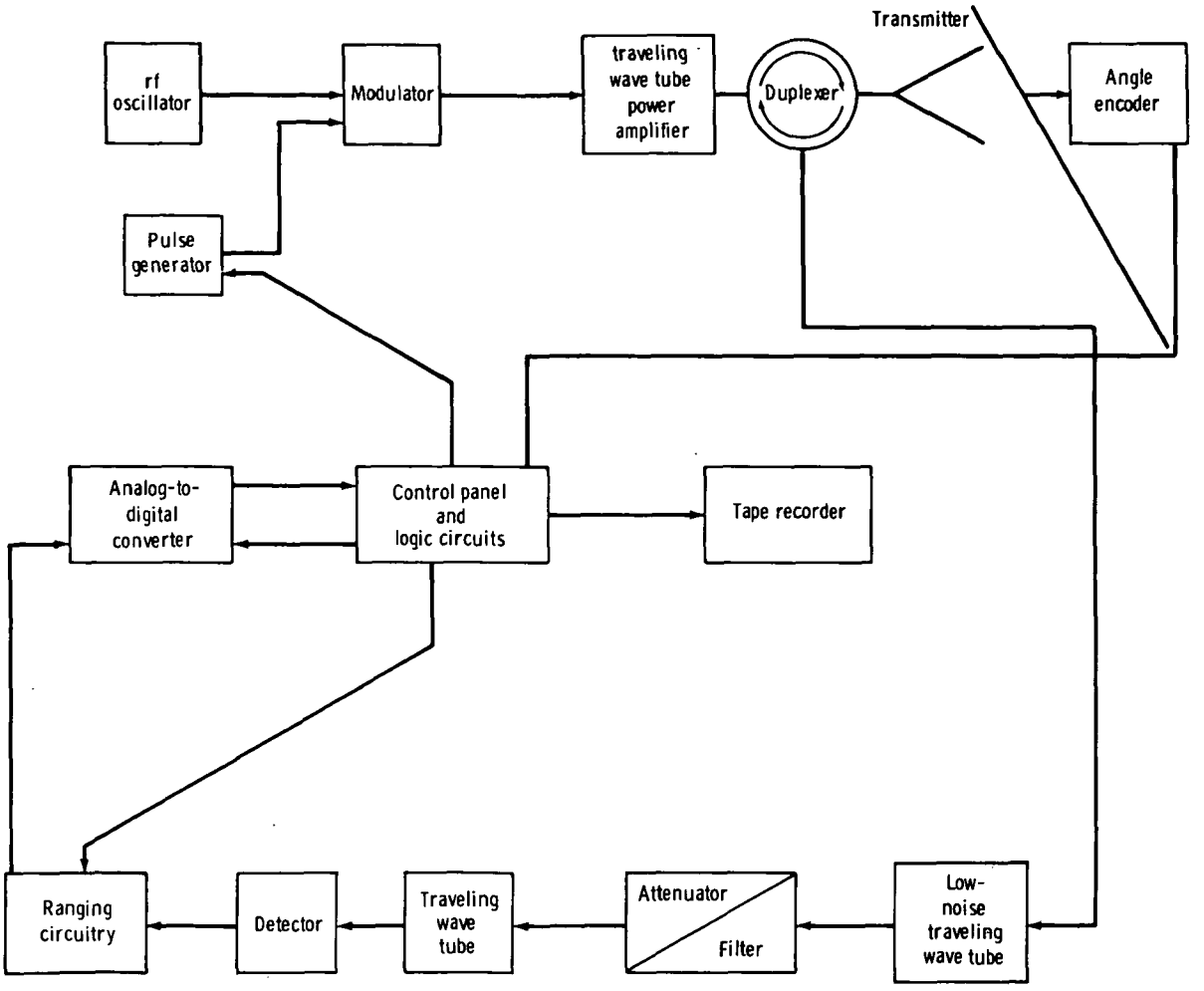


FIGURE 3–62.—Block diagram of surface contour radar.

Center experimental aircraft or another similar plane.

*Surface analytic altimeter.*—Altimetry technology has rapidly advanced beyond the capability of present satellite orbital determination and geodesy. Both orbital determination and geodetic improvements will be aided by the GEOS–C experiments. The ability of an altimeter to measure ocean-wave heights is useful to ocean meterology without the need for either orbital or geodetic improvements. This capability gives the altimeter a favorable enough cost/benefit position to recover the longer term investment of improved geodesy and orbital determination needed to realize ocean topography goals such as measuring tides, boundary currents, eddy currents, and surge currents. Therefore, the possibility should be investigated that this capability (or some equivalent or better capability) to measure the properties of ocean waves will justify either added investment in altimeter capability or investment in radar imaging instrumentation.

The microwave technology that gives a basis for expanding the measurement capability is represented in the Skylab S193 altimeter orbital performance analysis. More specifically, certain anomalous operating conditions of this instrument highlighted the need for future altimeter designs to include automatic alinement of the antenna in the

TABLE 3–X.—*Typical Parameter Values*

| | |
|---|---|
| Aircraft altitude, m | 300 |
| Aircraft velocity, m/sec | 70 |
| Approximate antenna beamwidth, deg | 1.2 |
| Antenna diameter, m | 0.5 |
| Radar spot size, m | 7 |
| Radar wavelength, mm | 8 |
| Radar pulse width, nsec | 1 to 2 |
| Scan rate, Hz | 10 |
| Pulse rate, pps | 500 |
| Scan angle, deg | 10 |
| Ground swath, m | 100 |

vertical direction. Furthermore, the analysis concluded that the average return waveform contains the information required to exercise the desired control primarily by wave-shaping effects caused by pointing error, but also by the Doppler content of the returns.

The effects of antenna pointing error on the return waveshape are given in reference 3–101, which also contains a discussion of how to use this information for nadir pointing control. The change of return signal Doppler content as a function of pointing error is as follows:

1. If the pointing error is forward along the subsatellite path, the power spectral density of the returns will be skewed toward positive Doppler.

2. If the pointing error is backward along the subsatellite path, the power spectral density of the returns will be skewed toward negative Doppler.

3. If the pointing error is orthogonal to the subsatellite path, the power spectral density of the returns will peak around zero Doppler.

These effects did appear in the Skylab S193 altimeter mode III data analysis for return signal space/time decorrelation in which crosstrack pointing errors showed up by increasing significantly the decorrelation times of the signals following the peak of the return. A second type of anomalous operating condition occurred during the Skylab S193 altimeter experiments.

1. Antenna pointing errors as large as 2° from the vertical did not cause the altimeter to "automatically abort" the experiment. Instead, the instrument exhibited a "pseudotrack lock" condition characterized by large standard deviations of altitude track jitter error accompanied by automatic gain control readings indicating anomalously low return signal power.

2. In some instances, the attitude error of approximately 2° rapidly decreased (during the proces of Skylab attitude control attempting to bring the spacecraft to the Earth pointing condition). In these cases, the "pseudotracked" altitude was rapidly decreasing, whereas the received signal strength was rapidly increasing, until the pointing error was approximately three-fourths of the antenna 3-dB beamwidth, at which point the altimeter operations switched to "true altitude track lock," characterized by approximately a 0.5-m tracking error jitter and a high received signal level. Unfortunately, this sequence of operation was initially considered to be proof that the S193 altimeter could not track high-altitude rates. However, analysis of both the orbit (in which the observed rapidly decreasing altitude could not have been real) and the Skylab attitude history (showing that the Earth pointing attitude was being initialized) disproved this contention. In fact, with the given conditions, the altimeter, by its nature, had to operate just as it was observed to operate.

The effect of the only satellite altimetry technology available reveals the following information:

1. Future altimeters will require better antenna pointing and better pointing error resolution.

2. The altimeter can provide this needed pointing control.

3. The antenna pointing should be done electronically by using a simple array to eliminate torquing of the satellite.

An altimeter design that has these capabilities is also given a "natural" added capability in the following respects:

1. It can be programed to have its antenna pointing at the vertical to receive the altitude return, and/or it can be pointed to receive the return from angles off vertical incidence.

2. Signal processing of the returns from angles off vertical incidence will yield the wave-directional spectra of the ocean surface and, possibly, the power spectral density of these waves.

*Instrument requirements.*—The proposed surface analytic altimeter instrumentation will require a phased array antenna. Beam forming and pointing will be controlled by the altimeter from the average wave shape and Doppler information contained in the returns from the vertical (altitude returns). On alternate pulses (or the second pulse of dual pulses), the antenna will be pointed to illuminate and receive returns from off-vertical incidence. The alternate on/off vertical illumination is to be sequenced around a circle at a radius $R(t)$ from the subsatellite path. For SEASAT geometrics, this circle would have a radius of approximately 25 km. The surface analytic function is performed on the returns from this off-vertical scanning shown in figure 3–63. The short pulse scanning the surface off vertical incidence produces down-chirp frequency-modulated returns with a different down chirp for each wavelength composing the surface. The area $A_0$ represents the altimeter footprint. Areas $A_1, A_2, A_3 \ldots A_i \ldots A_j$ show the location of the surface from which returns at time $t$ are equal to 2700 nsec (where the time of altitude return is $t=0$). These areas sweep outward across the ocean waves at the rate

$$\frac{d}{dt}R(t) = \frac{d}{dt}\sqrt{cht} \doteq \frac{250 \text{ m/nsec}}{\sqrt{t}} \qquad (3\text{–}20)$$

where spacecraft altitude is 800 km. This produces a down-chirp frequency modulation of returns from each surface wavelength $\lambda_{0, 1, \ldots, i, j}$ of

$$f(t, \lambda_i) = \frac{250}{\sqrt{t}\,\lambda_i} \qquad (3\text{–}21)$$

where $f(t, \lambda_i)$ is in gigahertz. The physical mechanism and geometry involved is shown in figure 3–64. The surface length of short radar pulse $\delta_{\text{pulse}}$ equals $(c\tau)/[2 \cos (ct/h)]$, where $c$ is the speed of light, $\tau$ is pulse duration, $h$ is satellite altitude, and $t$ is time after altitude return. The frequency of the change in signal strength (amplitude) of the returns changes as a function of time. The short length of the radar pulse illuminates only portions of the ocean wavelength, and strong returns will come preferentially from the side of the waves toward the radar creating these down chirps $f_i(t, \lambda_i)$, which are func-

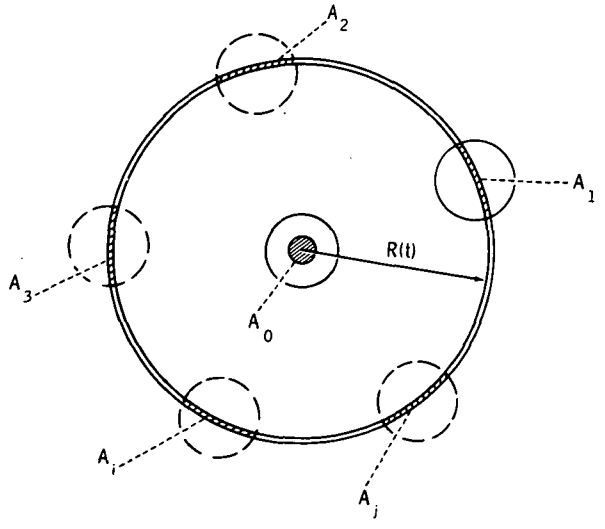


FIGURE 3–63.—Antenna illumination of ocean surface for surface analytic altimetry.

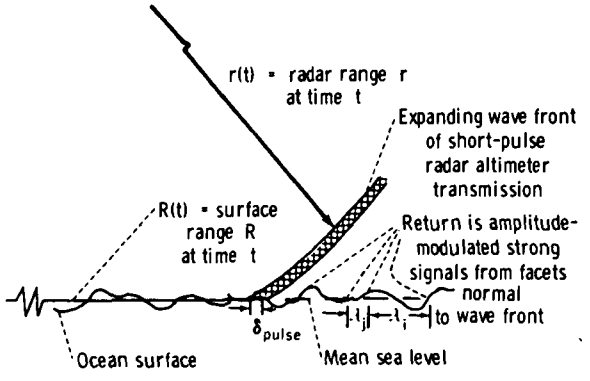


FIGURE 3–64.—Physical mechanisms involved in creation of down-chirp frequency modulation of returns from ocean surface with wavelengths $\lambda_i$, $\lambda_j$ longer than $\delta_{\text{pulse}}$.

tions of surface wavelength $\lambda_i$. Figure 3–65 shows the log-log plot of surface wave down-chirp modulation (frequency as a function of time) for ocean wavelength $\lambda_s$ from 25 to 1000 m. One reason for selecting the off-vertical scan circle radius of 25 km is that pulse compression circuitry is at least as feasible as a signal process matched to the returns. Figure 3–66 shows the surface wave down-chirp modulation for $\lambda_s$ from 25 to 500 m. Twenty-percent resolution of these wavelengths appears feasible. Simply stated, 1-$\mu$sec pulse compression circuits matched to these chirps could be selected so that no frequency overlap would occur between them over the bandwidth from 8 to 225 MHz. That set of pulse compression circuits comprises a matched receiver for the signal parameter of interest (i.e., the surface wavelengths in radial direction of each off-vertical step). The approximately 15 outputs obtained from each radial sweep at the 25-km radius should be converted from analog to digital and sent to ground processing. Probably, the only further processing required would be accumulating these numbers for approximately 2 sec

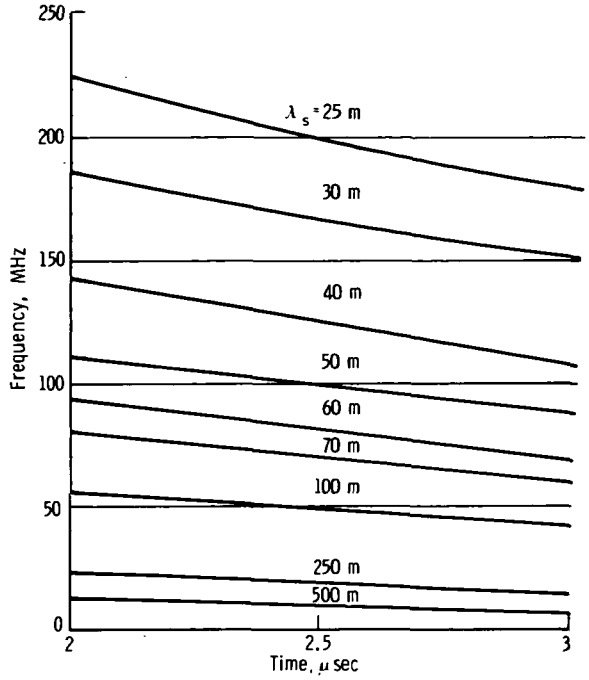


FIGURE 3–66.—Ocean surface wave down-chirp modulation in the 2- to 3-$\mu$sec window containing returns from the off nadir pointing surface analytic altimeter. From this plot it appears feasible to achieve 20-percent resolution of surface wavelengths using approximately 15 chirp pulse compression delay lines to cover the range from 25- to 500-m ocean wavelengths.

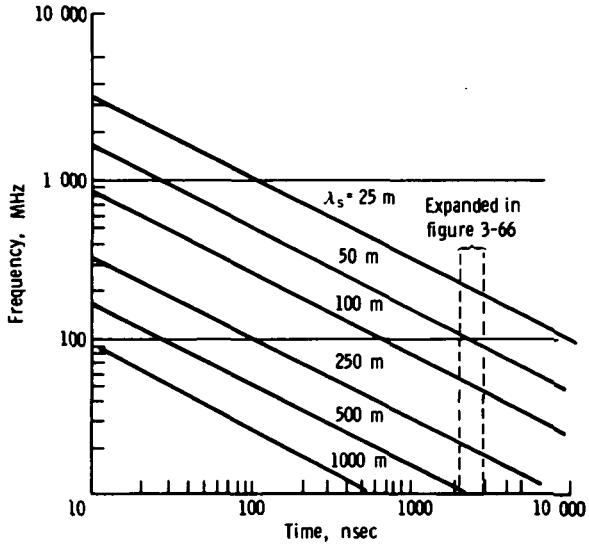


FIGURE 3–65.—Log-log plot of ocean surface wave down-chirp modulation as a function of time after altitude return. The surface analytic altimeter signal processor could be pulse compression delay lines tuned to these down chirps.

and plotting them as an amplitude contour obtained around the circle. Of course, this is a distortion of the wave directional spectra, but it should serve as a "first look" process. Spectra of particular interest can be extracted for the transformation processing required to map wave direction in latitude and longitude.

Undoubtedly, a different transformation will be required to use the same data in the wave forecasting algorithms, and a different transformation will be required for some other application.

These transformations should probably be done from the raw data (or, at most, edited raw data) so that less processing is required to get the data-editing quick-look function performed.

*Technical approach.*—Conceptual design

studies on future design and applications of satellite altimetry are required to determine a basic question. Should altimeter instrumentation become more complex by adding capability natural to its particular radar geometry, or should it be made less complex (restricted to altitude tracking only)? The answer to this question requires determining the possibilities, the payoffs, the needs for overlap and supportive data from different instruments, etc. The possibility exists that, in a fully instrumented oceanographic satellite, the need for accurate altitude measurements for 1 yr to solve ocean tide and circulation problems will be all that is required from the altimeter. This postulation assumes that the other instrumentation will obtain all the information for ocean meteorology. If this case were true, a much-simplified altimeter designed for 5- to 10-yr orbital operation may be the final configuration specified.

A laboratory research and development study should be undertaken to demonstrate the pulse compression performance obtainable for the ocean-surface-wave down-chirp-type signals. This class of chirp signal is different because it is not a linear frequency modulation with time. It is independent of transmitted carrier frequency or phase, and the down-chirp modulation ceases only at the horizon where it equals the speed of light divided by the surface wavelength.

Applications studies should be made to determine if the 25-km radius for obtaining wave directional spectra can be increased or should be decreased. Data processing required to apply these measurements should be studied.

*Applicability.*—The proposed surface analytic altimetry instrumentation simply extends the capability of an altimeter to measure the physical properties of sea state. The application of altimetry to ocean meteorology is improved. The application of altimetry to geodesy and static and dynamic oceanology will be that expected from altimetry with an accuracy of 10 cm.

*Radar spectrometers and dual-frequency interferometers.*—Several other instruments that have potential for determining ocean-wave spectral characteristics also advantageously use the "tilt modulation" effects described previously. One instrument is the "wave spectrometer." This instrument emits a short pulse for which the (effective) spatial width is less than one-half the length of the gravity waves to be observed (e.g., a pulse width of 10 nsec will provide a spatial resolution of approximately 5 m at a 15° incident angle, which is adequate to resolve gravity waves longer than 10 m). As this pulse travels out across the longer gravity wave, it illuminates specularly reflecting regions, the scattering characteristics of which vary with the slope (and position) over the longer wave. Hence, the received signal as compared to time (as would normally be displayed on an A-scope) will carry an amplitude modulation pattern corresponding to the period of the longer gravity wave. By Fourier transforming this amplitude function, a signal spectrum is produced, which is directly proportional to the ocean-wave slope spectrum along the radar line of sight. Both the first and second mechanisms described in the preceding section are responsible, to some degree, for the operation of the spectrometer. However, the third mechanism should not affect the spectrometer because the return on the A-scope is essentially instantaneous and will not be changed by the orbital velocity of the specular scatterers.

The dual-frequency interferometer is basically a frequency-domain implementation of the wave spectrometer described previously; it transmits two closely spaced frequencies, $f_1$ and $f_2$ ($\Delta f = f_2 - f_1$ ranging between 1 and 100 MHz). The correlation function of the power return at the two frequencies is then taken at the output of the receiver. Theoretical analyses have shown that this function, as compared to separation wave number $\Delta k = (2\pi\Delta f)/c$, is proportional to the slope spectrum of the longer wave components along the radar line of sight. This technique has not been demonstrated experimentally. From the theoretical models, unanswered questions

still exist about the magnitude of the desired portion of the correlation function containing the slope spectrum. Questions must also be answered concerning performance in the presence of noise and the average time required to observe a given level of sea echo correlation coefficient. However, the technique appears attractive at this point because of its simplicity and potentially low data-rate requirements compared to the wave spectrometer.

*Dual-frequency wave-height sensor.*—Work is underway at LaRC to use dual-frequency radar techniques to measure significant wave heights and probability density function of large ocean waves. The technique has been described by Weissman (ref. 3–102), and the basic results are summarized here.

If a vertical viewing radar transmits two microwave signals at frequencies $f_1$ and $f_2$ from an altitude $H$ above mean sea level, if the antenna pattern is ignored, and if the radar illuminates a statistical ensemble of specularly reflecting wave heights, then the absolute value of the time average of the product of the returning signals is

$$|\bar{R}(\Delta k)| = \frac{|\langle E(f_1)\,E^*(f_2)\rangle|}{\sqrt{\langle|E(f_1)|^2\rangle\langle|E(f_2)|^2\rangle}} = |\langle e^{i2\Delta k h}\rangle| = \left|\int_{-\infty}^{\infty} P(h)\,e^{i2\Delta k h}\,dh\right| \tag{3–22}$$

where

$R(\Delta k)$ = the correlation coefficient

$\Delta k$ = difference wave number $= [2(f_1 - f_2)]/c$

$c$ = speed of light

$h$ = height of a specularly reflecting wave

$P(h)$ = probability distribution function of heights

$E(f)$ = electric field of the scattered signal

$*$ = complex conjugate

$i = \sqrt{-1}$

$\langle\ \rangle$ = ensemble average

Thus, performing measurements by transmitting a sequence $<f_1, \Delta f_2, \ldots, \Delta f_n>$, the significant wave height $H_{1/3}$ and some features of the probability density function can be measured. The latter measurement may have some applicability to the detection of ocean currents. This is strictly a vertical viewing measurement and requires narrow-beam antennas.

This technique is a frequency analog of the impulse altimeter. If complex expression (magnitude and phase) for $R(\Delta f)$ is Fourier-transformed from the frequency domain $\Delta f$ to the time domain, the solution to the impulse response of a rough surface is obtained.

*Bistatic high-frequency local wave directional sensor.*—A concept will be described that may provide the directional wave-height spectrum near a fixed point of interest on the ocean as a satellite passes overhead. This concept is illustrated in figure 3–67 where the point on the sea is shown as a buoy; actually this point could be a ship, island, tower, or coastal site as well. Also, although figure 3–67 indicates the satellite as the receiver and the surface point as the transmitter, the converse is actually a more desirable situation. In that configuration the satellite would transmit a low power signal (less than 10-W average), which would be stepped through the hf region (from 2 to 30 MHz). The spacecraft antenna could be an electrically small omnidirectional loop or dipole pair. The user below (e.g., a ship) would receive both the direct signal from the satellite and a sea-scattered signal at a given delay time (corresponding to a given range from the ship). Thus, collection and use of the sea-state data would be at the user's option and would require carrying onboard only a receiver, a simple digital processor, and a schedule of satellite passes (which need not be directly overhead).

The principle supporting the technique is Bragg scatter. In the bistatic configuration, a contour of constant time delay is an ellipse, in general, which becomes a circle when the satellite is directly overhead. The waves from which scatter is taking place are exactly one

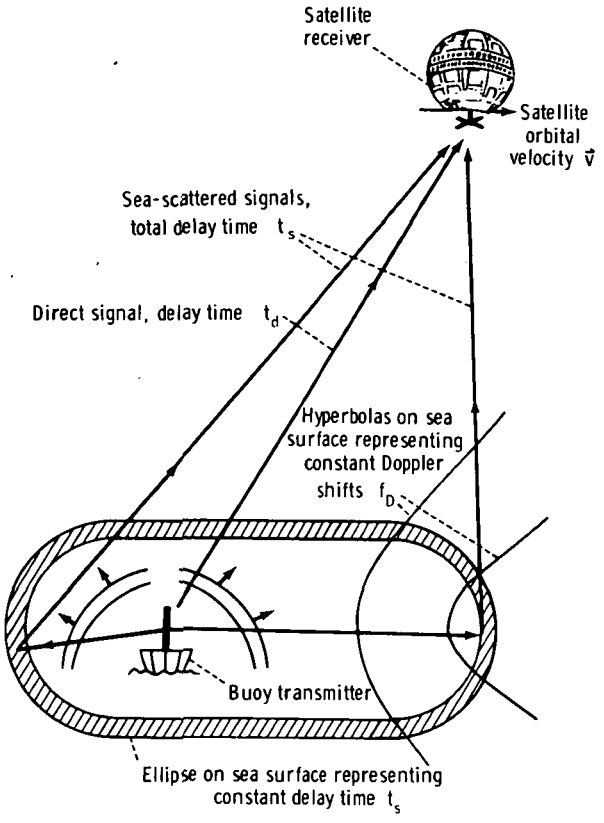


FIGURE 3–67.—Illustration showing concept of bistatic high-frequency local wave directional sensor.

radar wavelength long (when the satellite is overhead); thus, by sweeping from 2 to 30 MHz, one is measuring the heights of the ocean waves (as the strength of the received signal), the lengths of which range between 150 and 10 m.

Wave directionality is obtained by the Doppler imposed on the scatter by the satellite velocity. The greatest Doppler originates from that portion of the time-delay circle directly ahead of the satellite, with zero Doppler at the sides and the greatest negative Doppler from behind. For the satellite directly overhead, the scattered sea-echo Doppler is described by a simple cosine function of angle from the satellite track. An example of the Doppler spectrum produced at 5 MHz by an isotropic sea is shown in figure 3–68. Any departure from this shape represents the directional nature of the ocean waves and can

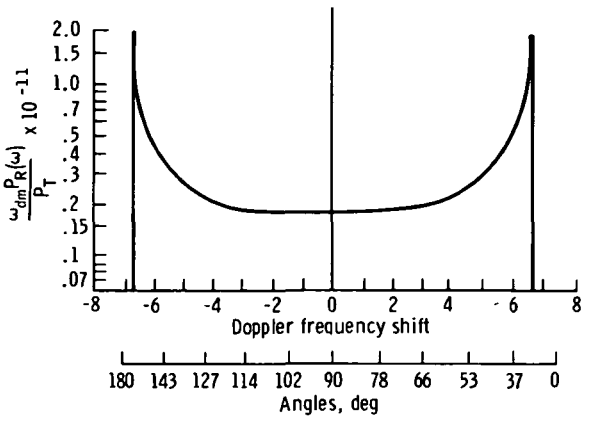


FIGURE 3–68.—Example of Doppler spectrum produced at 5 MHz by an isotropic sea (where $\omega_{dm}$ is maximum satellite-induced Doppler shift, $P_R(\omega)$ is average received power spectral density, and $P_T$ is average transmitted power).

be obtained by straightforward digital processing of the signal spectrum. The angles designate the direction of the ocean waves with respect to the satellite track, which produces the Doppler at that point.

This technique, which is straightforward and easy to implement, has the advantage of requiring no data processing aboard the satellite. Furthermore, because the users receive the direct signal also, they have all the information they need to calibrate the system and remove unknown transmitter/receiver drifts and path losses. Because the ionosphere will pose the ultimate limitation on such a system, this self-calibrating feature is very desirable. A thorough system study and experimental evaluation of the concept is currently underway at Batelle-Columbus Laboratories under Wallops Flight Center support.

*Microwave radiometry.*— Observations (refs. 3–32 and 3–103) of the surface-roughness effect have indicated an apparent dependency on observational frequency, increasing with increasing frequency. In addition, surface-roughness effect is a function of the angle of observation and polarization of the radiation received. Increases of 1.1 K of the horizontally polarized brightness temperature at 19.34 GHz and 55° inci-

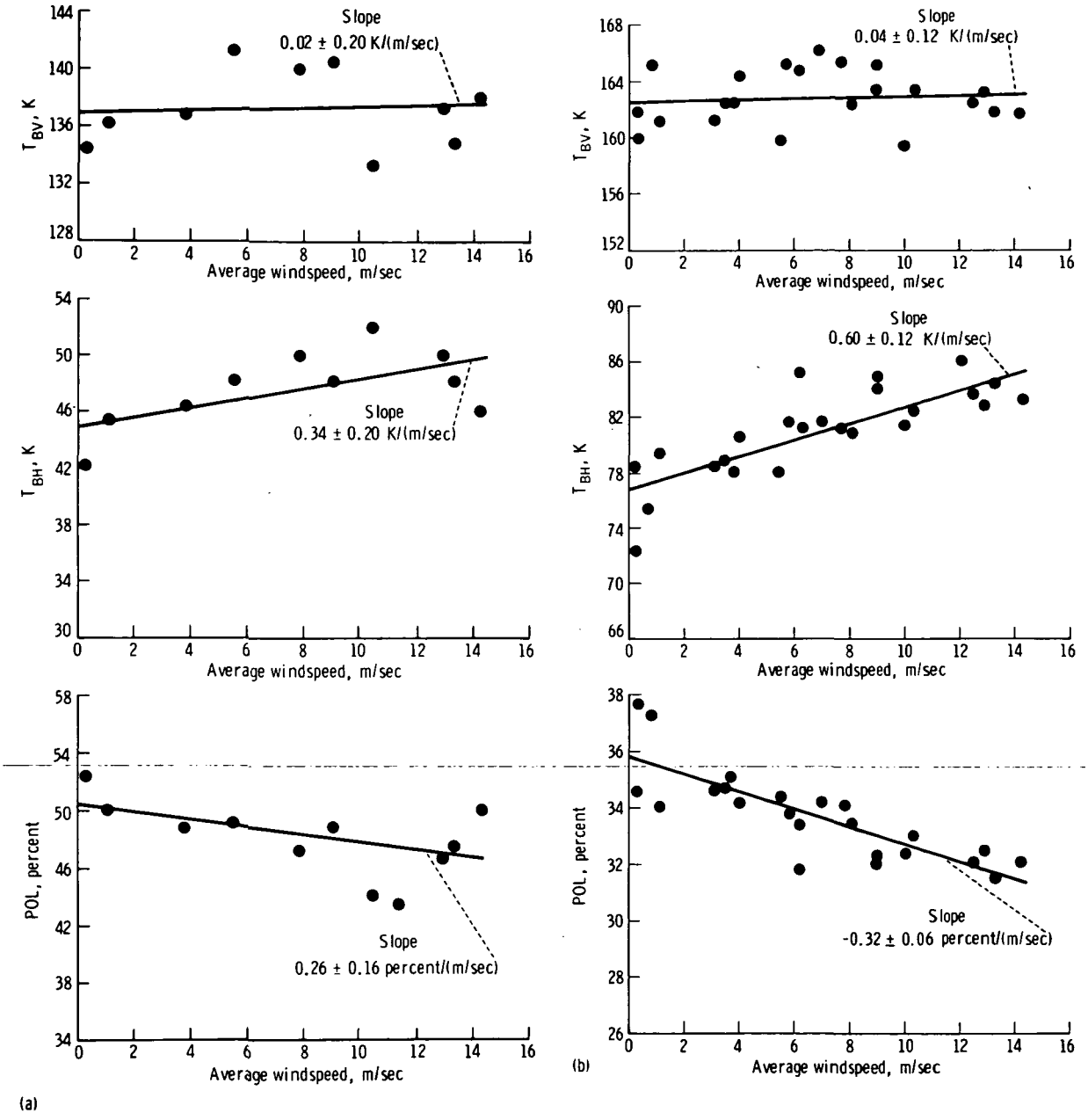


FIGURE 3–69.—Measurements of the surface roughness effect made from Argus Island Tower of Bermuda where $T_B$ is brightness temperature, $V$ is vertical polarization, $H$ is horizontal polarization, and

$$POL=\frac{T_{BV}-T_{BH}}{T_{BV}+T_{BH}}\times 100.$$ (*a*) Frequency=1.41 GHz. (*b*) Frequency=8.36 GHz.

dent angle with 1-m/sec changes in windspeed have been measured. Measurements of the surface-roughness effect made from Argus Island Tower of Bermuda at 1.41, 8.36, and 19.34 GHz (ref. 3–32) are shown in figure 3–69. The surface-roughness effect is closely coupled to the local windfield, rapidly responding to changes in the local wind;

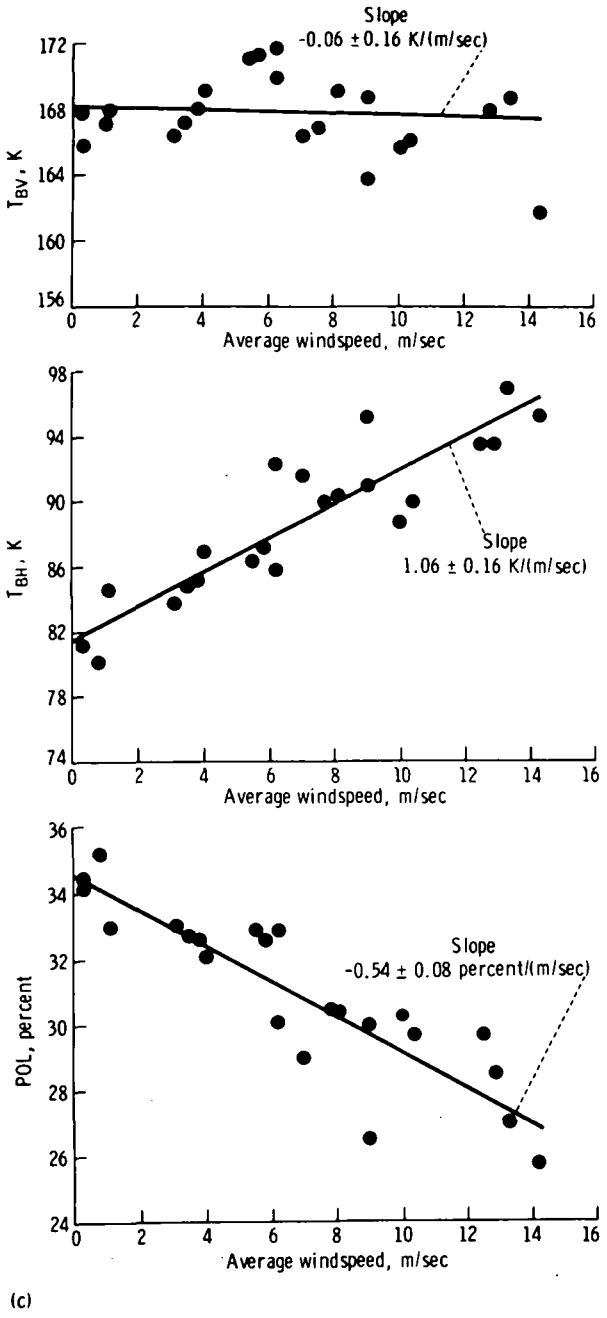


FIGURE 3–69 (concluded).—Measurements of the surface roughness effect made from Argus Island Tower of Bermuda where $T_B$ is brightness temperature, $V$ is vertical polarization, $H$ is horizontal polarization, and $POL = \frac{T_{BV} - T_{BH}}{T_{BV} + T_{BH}} \times 100$. (c) Frequency = 19.34 GHz.

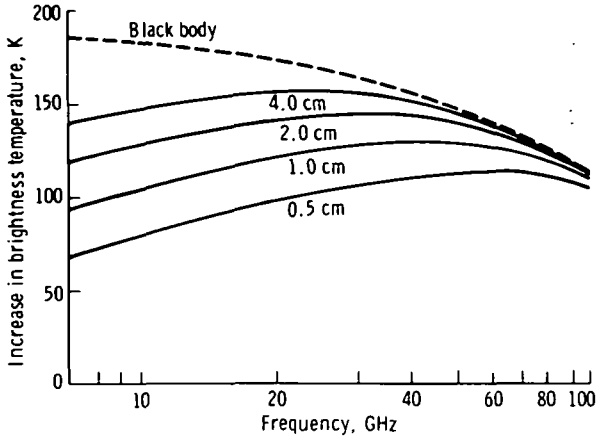


FIGURE 3–70.—Brightness temperature of foam as a function of microwave frequency.

hence, it is relatively insensitive to the energy content of low-frequency gravity waves. Evidence indicates that the surface roughness effect is primarily dependent on the mean-square surface slope.

Observations of the sea-foam effect (refs. 3–104 and 3–105) have shown it to have a very high brightness temperature (approaching the physical temperature of the sea) compared to the average sea surface. Recent laboratory and aircraft-borne measurements [5] are shown in figure 3–70. The evidence available indicates that the spectrum of the brightness temperature of foam is relatively flat at microwave frequencies, with a slight decrease with decreasing frequency. The high brightness temperature of foam is consistent with the foam serving as a matching layer to the sea rather than to inherent high loss in the foam. Unless the high brightness temperature of foam results primarily from very high loss of the foam, which seems unlikely, the brightness temperature will decrease with decreasing frequency when foam thickness of only a fraction of the observational wavelength is reached. The brightness temperature of foam is much less dependent on polarization and incident angle than is the compact sea surface.

[5] Unpublished data from James P. Hollinger, 1974.

Clearly, more detailed measurements as a function of the observational parameters of frequency, polarization, and incident angle over the range of foam characteristics, such as thickness, bubble-size distribution, water content, and degree of spatial uniformity, are required to fully understand the microwave properties of ocean foam. In addition to incomplete knowledge about the microwave characteristics of foam, the determination of the brightness temperature dependence on windspeed caused by sea foam is further complicated because the foam coverage of the sea surface does not depend only on the local wind. The foam coverage also depends on the air/sea temperature difference, the duration and fetch of the wind, and the history of the wave spectrum of the sea area being observed. An analytical model including these parameters and depending on the dissipation (by breaking waves) of energy transferred from the wind to the wave spectrum has been developed by Cardone (ref. 3–106) to predict whitecap coverage. This model is in reasonably good agreement with microwave measurements at high windspeeds (refs. 3–30 and 3–31). In addition to whitecaps, considerable wind streaking (thin lines of foam oriented in the direction of the wind) occurs at high windspeeds. Above approximately 12 m/sec, streaking contributes more to the total white water visible on a photograph than do whitecaps (ref. 3–107). The details of the microwave brightness temperature of streaks compared to that of whitecaps are not presently clear and result in difficulty in interpreting the detailed whitecap/streak/windspeed/brightness-temperature interrelationship. However, the general increase of microwave brightness temperature with windspeed caused by increasing coverage of the sea with foam is well established.

The increased noise temperature (ref. 3–103), which results from sunlight reflecting or scattering off the water, is shown in figure 3–71, where brightness temperature is plotted as a function of time. These data were obtained by pointing microwave radiometers at a fixed viewing angle over water (at the complementary Sun elevation angle) and allowing the image of the Sun to pass through the antenna beams. The closed points represent data obtained when the water surface was smooth, and the open points correspond to the data obtained when the surface was roughened by waves. The data show that, under calm conditions, the noise input to the receiver can significantly increase when solar radiation reflects specularly into the antenna, particularly at the lower microwave frequencies. When the water surface is very rough, the scattering generally becomes diffuse and causes a quasi-isotropic increase in brightness temperature, which may be tens of degrees at the lower microwave frequencies. In addition to showing the increased noise temperature in a radar receiver, these data imply that ocean roughness can be inferred by radiometrically measuring the microwave glitter pattern of the Sun.

*Solar microwave interferometer.*—The proposed instrument, the solar microwave interferometer imaging system (SMIIS), represents a novel application of the radio astronomers' very long baseline interferometry (VLBI) and forward scatter radar concepts and technology. The SMIIS can serve as a research tool for ocean studies but has limited operational potential. The history of both technologies are thus pertinent. Because the function of SMIIS (i.e., obtaining microwave imaging of the Earth environment) is also the function of any other proposed radar imaging systems being considered by the Active Microwave Workshop, the history and technology of radar imaging is also pertinent.

*Present state of the art.*—The applicable technology is contained in the previously stated historical connections to VLBI, forward scatter radar, imaging radar, short baseline interferometry, and phased arrays technologies. The present state of the art in satellite microwave antenna technology is specifically of interest because of the rela-

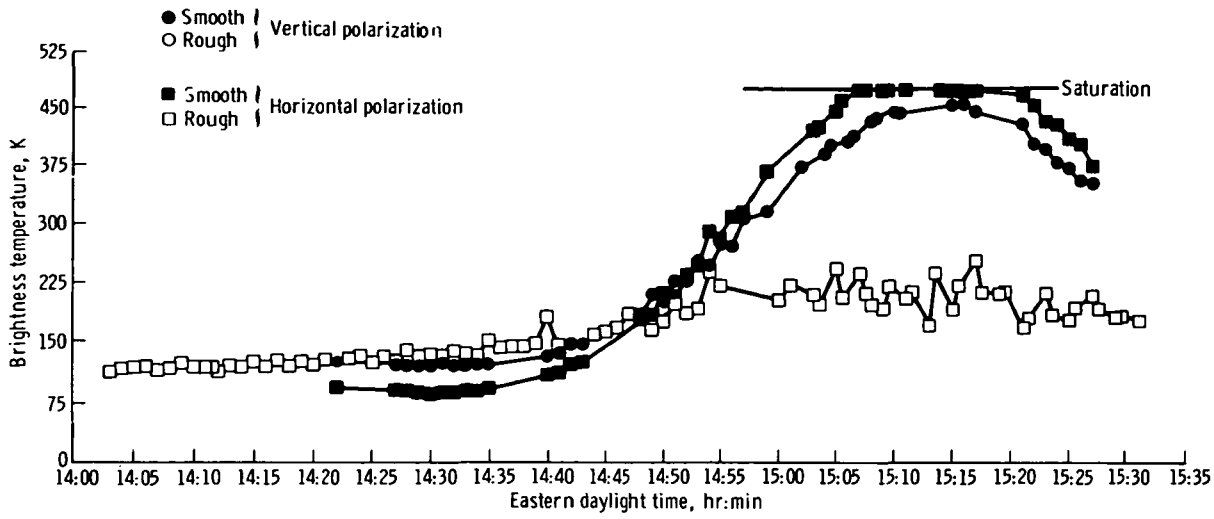


(a)

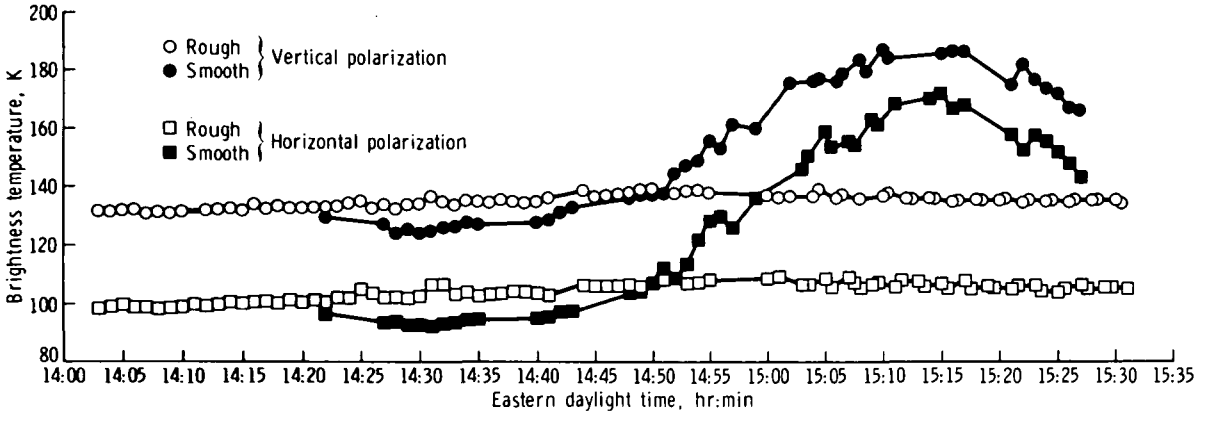


(b)

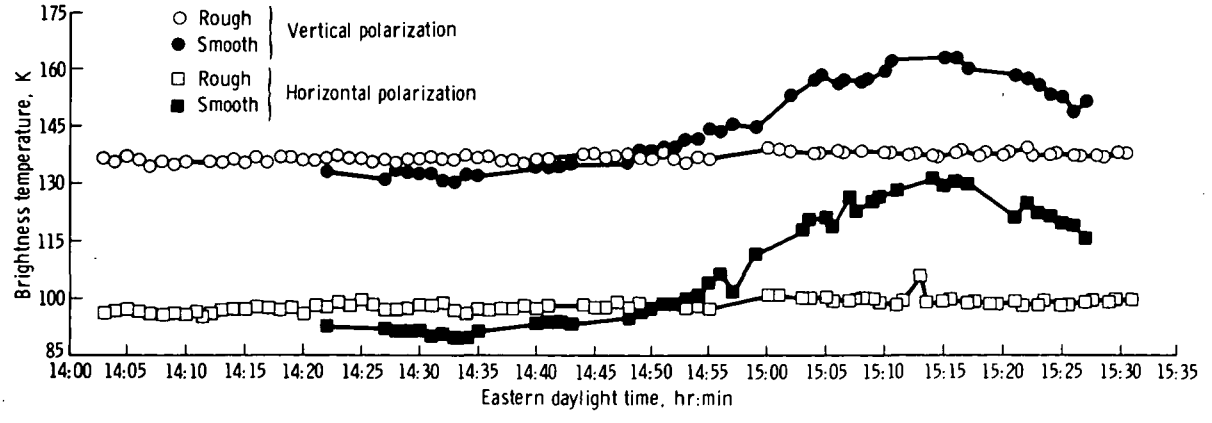


(c)

FIGURE 3–71.—Change in brightness temperature as a function of time. (*a*) Frequency =1.4 GHz. (*b*) Frequency=4.0 GHz. (*c*) Frequency=7.5 GHz.

tively large apertures and antenna pointing requirements for SMIIS.

The standard questions regarding onboard as compared to ground-site data processing associated with all satellite-borne imaging instruments must also be studied for the SMIIS. Thus, the communication/ground-site data processing and the inverse onboard data processing/communication state of the art is pertinent.

*Qualitative concept description.*—Figure 3–72 shows the proposed SMIIS instrumentation. The satellite (at 800-km altitude) has one antenna pointing directly at the Sun and another antenna pointing at the glistening surface of the Earth (i.e., the region surrounding the Sun-to-satellite specular reflection point).

The Sun-pointing antenna receives the solar noise by way of the direct ray path. This broadband noise radiofrequency signal is band-limited (to the level required for the desired imaging resolution of the system) and baseband detected by using a coherent local oscillator. The band-limited bipolar noise signal obtained and the time lags generated from the coherent local oscillator are recorded (or communicated to the ground) and stored as the reference phase and amplitude modulation for the VLBI-type correlation processing that follows. All surface elements contained within the glistening surface are also illuminated with the same solar microwave noise, except for propagation path noise differences and some signal decorrelation. The amount of signal decorrelation will be one of the problems requiring further investigation; however, for S-, C-, and X-band wavelengths, these illuminated points fall within the first (or first few) Fresnel zones of every point source of noise at the Sun generating the incident microwave noise.

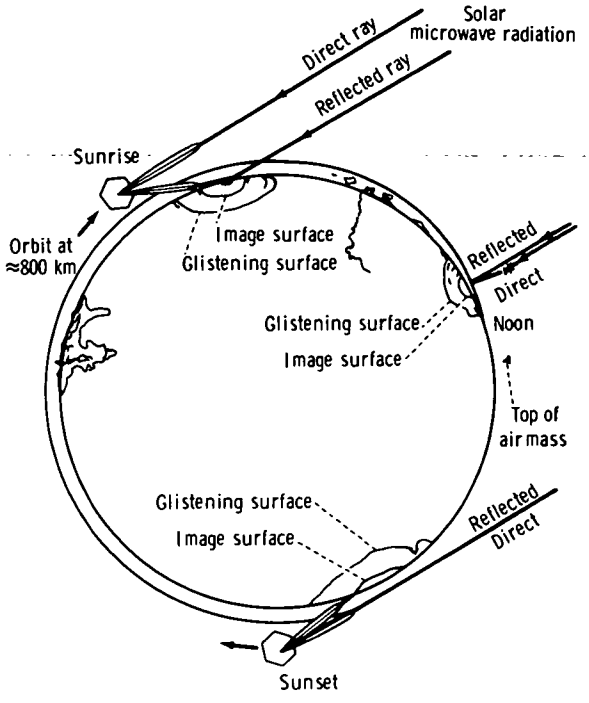


FIGURE 3–72.—Earth environment mapping using the SMIIS. Note the changes in the size and shape of the imaging and the glistening surfaces for satellite sunrise, noon, and sunset. Also note that the direct ray signal always precedes the forward scatter signal in time.

The forward scatter from the surfaces, facets, wavelets, etc., in the glistening surface provides the communication link between the VLBI remotely illuminated antenna and the satellite VLBI master antenna. These multiple-reflected signals from the glistening surface are received at the satellite and beat to baseband bipolar video by using the same receiver-coherent local oscillator that was used to obtain the direct ray reference signal. This composite baseband is time-tagged, recorded (or communicated to ground), and stored. The VLBI process is then applied to the record obtained from the reflectors in the glistening region. This process consists of applying the first-order Doppler correction (i.e., that computed for the ray reflection point in the glistening region), then running a cross-correlation of the forward scatter record with this first-order Doppler-corrected reference record. Strong correlation peaks will be generated in this time record; in fact, each peak will be a range pulse compression for a strong forward scatterer. The range pulse compression actually applied depends on the bandwidth of the reference record $B_{REF}$ and the time length of that record $R_{REF}$. The width of the cor-

relation peak will be approximately $1/B_{REF}$, whereas the amplitude of the correlation peak will be proportional to the product of the reference record length $T_{REF}$, the forward scatter signal strength from each surface element $A_i$, and the match of the first-order Doppler correction to the Doppler frequency of that signal. The VLBI process completes the imaging process by successive correlations using differentially corrected Doppler reference records. This process is essentially a Doppler correction sweep across the glistening surface, in which each detected forward scatterer is positioned in azimuth by the Doppler correction that maximizes its correlation peak. The resultant range/azimuth map of correlation peaks comprises the polar microwave interferometer image.

*Quantitative description of the SMIIS.*— The following questions are among the first to be answered in designing the SMIIS:

1. Is enough solar microwave power available at the frequencies best suited to Earth environment planning?
2. If so, how large must the antenna apertures be to at least get the direct ray at adequate signal-to-receiver noise to enable interferometer processing?
3. What is the best antenna to use?
4. What bandwidth and reference signal duration will be required to provide adequate resolution?
5. What processing must be done at the receivers as opposed to what can or should be done at the ground sites?

The approximate answers to the first three questions can be obtained from the information presented in figure 3–73. The solid line shows the microwave power of the quiet Sun (in dBm/m²-Hz) in the range of frequencies from 30 MHz to 300 GHz. This microwave power is increasing at the rate of approximately 12 dB/decade, and, for frequencies above 4 GHz, the microwave noise power from an antenna with a 1-m² aperture will exceed the noise power from the best cooled parametric amplifier receivers available with present state of the art (shown by the dashed line). Figure 3–73 shows that

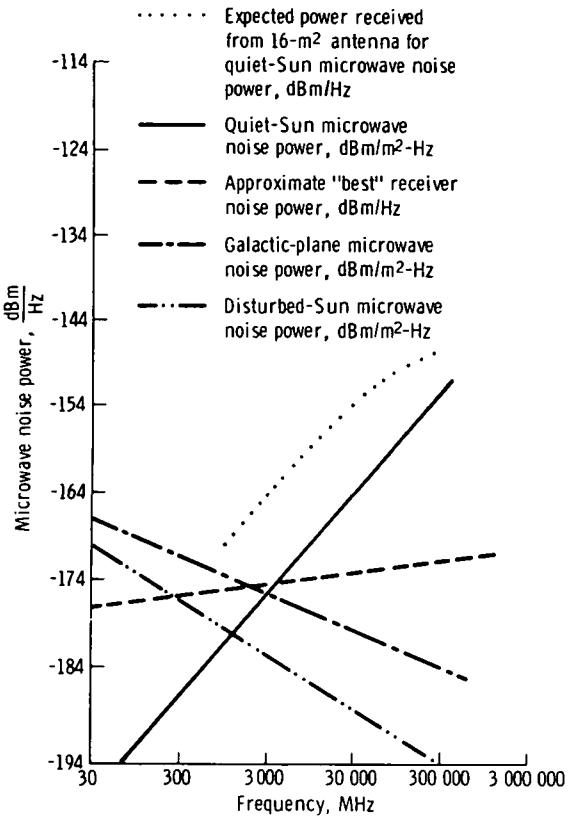


FIGURE 3–73.—Plot of solar and galactic-plane microwave noise power compared with frequency. Also shown is the approximate noise power of state-of-the-art, cooled, parametric amplifier receivers. Note that at 3000 MHz the SMIIS can use either solar or galactic-plane noise as the reference signal, thus giving day/night operation (ref. 3–108).

for almost all microwave frequencies suited to Earth environment mapping, enough microwave power is available from the quiet Sun to let the Sun be the transmitter in the SMIIS. Also shown is a dotted line, which illustrates the expected received power from a 16-m² antenna. This illustration indicates that for antenna apertures approximately as large as those required for radar mapping, the SMIIS could work at frequencies from 1 GHz and up. The microwave noise power available using the galactic plane as the transmitter for SMIIS with a 16-m² antenna aperture is sufficient for Earth environment mapping applications requiring frequencies below approximately 30 GHz. The 6-dB

signal to noise obtainable at 30 GHz is adequate for the SMIIS processes.

An initial assessment of the bandwidth required to provide adequate resolution for Earth environment mapping can be obtained from the requirement for wave directional spectra over the ocean. This data product is considered useful if ocean wavelengths from 50 m to 1 km are resolved in synoptic maps of the ocean suface. A 10-m/range resolution using SMIIS requires approximately a 30-MHz bandwidth bipolar video reference signal (because this is one-way propagation of electromagnetic waves; the resolution is at 3.3 nsec/m). Azimuth resolution of approximately 10 m requires approximately a 10-$\mu$sec duration of the bipolar video reference signals; that is, the differential Doppler from each reflecting center will cause detectable decreases in the cross-correlation peaks from records exceeding 10 $\mu$sec in duration. In the majority of cases, a much longer delay than 10 $\mu$sec will occur between the direct ray from the Sun and the reflected rays from the Earth environment; thus, much longer reference signals could be taken. However, the 300:1 pulse compression gain obtained from correlation processing the 10-$\mu$sec-duration 30-MHz-bandwidth signals should be adequate for SMIIS mapping.

The answer to question 5 is twofold.

1. The low-noise baseband receiver signal process should be performed onboard to preserve the best signal-to-noise ratio in the bipolar video signals.

2. The onboard as compared to ground data-processing tradeoffs, which must be made for radar mapping systems, apply to the SMIIS. However, the power, weight, and volume required for the radar systems transmitter can be applied to onboard data-processing electronics for the SMIIS; thus, all SMIIS data processing can be done onboard and still save power, weight, and volume over radar systems with similar mapping performance.

*Impact of microwave technology.*—The concepts embodied in the SMIIS bridge the present gap between the sophistication of the state of the art in radio astronomy (VLBI) and the state of the art in synthetic aperture radar. Because the microwave signals transmitted by the Sun (and/or the galactic plane) contain essentially all frequencies and polarizations possible, even the postulated performance of polypanchromatic radar (ref. 3–109) can be obtained with SMIIS. This attainment would represent a significant advance in the microwave mapping state of the art.

*Requirements.*—Generally, the same requirements are needed for the SMIIS instrumentation on a satellite as for any high-resolution microwave radar imaging instrument, except for one very significant difference. Radar images require a high-power transmitter, transmitted signal modulation electronics, and a matched receiver/demodulator for each microwave band used, whereas SMIIS does not require any transmitter or modulation electronics because it uses cosmic noise sources in the transmitter/transmitted signal modulator role. The fact that SMIIS has been described and initially designed as receiving its reflected signals from the region of forward scattering surfaces does not limit the system to operation in this viewing direction (i.e., this is not a requirement or limitation); it is simply the direction from which the strongest reflected signals are expected and, as such, represents the easiest direction for high-signal-to-noise, high-density mapping operation.

Electronically scanned multifrequency array antennas would be required to obtain SMIIS operation in many frequency bands with minimum use of satellite space. These antennas would not be a requirement of early experimental versions of SMIIS, but the technology of these array antennas should be nurtured for use with future operational versions of SMIIS.

Onboard data-processing requirements will be equivalent to those for radar imaging systems with the same need for growth, from the minimum amount possible to the maximum amount required, and for Earth en-

vironment monitoring and reporting missions that will evolve.

*Technical approach.*—Conceptual design studies should be done to determine the total capability of SMIIS instrumentation and to identify research and development requirements and feasibility demonstration experiments that can be done with existing instrumentation (for instance, the Massachusetts Institute of Technology Haystack radar performing SMIIS-type mapping of the lunar surface, possibly using radio stars instead of the Sun as transmitters).

Feasibility/applications studies should be done to determine design specifications for experimental SMIIS instruments aimed at specific applications missions.

A project to develop SMIIS instrumentation, data processing, and data use would be appropriate. One possibility would be to use one of the large antennas at Wallops Flight Center to get the direct ray reference bipolar video record while simultaneously obtaining the reflected ray record from an airborne platform. Both ocean and Earth could be viewed at all incident angles and at any distance from the reference station to obtain design data related to these parameters.

Continuing research and development is warranted in the area of real-time correlation technology (such as that presently underway at the General Electric Research and Development Center using charge-coupled devices that give a 32-bit correlator operating at 10 MHz on a single large-scale integration flatpack). Special developments for SMIIS applications may justify short-term funding in this technology.

*Applicability.*—The Earth environmental mapping capabilities of the proposed SMIIS extend from monitoring solar disturbances and mapping the ionosphere, using the low-frequency end of the spectrum, to mapping atmospheric phenomena using the high-frequency end of the spectrum. Only the development of receiver technology at millimeter and submillimeter wavelengths is required to close the gap between microwave imaging and long-infrared imaging instrumentation.

### Other Active Microwave Sensors

*Wave motion sensor.*—A new technique being developed at the Applied Physics Laboratory of Johns Hopkins University (APL/JHU)[6, 7, 8] is potentially capable of mapping the significant height $H_{1/3}$ of ocean waves over a wide field of view beneath either an aircraft or a satellite. The technique directly measures the Doppler broadening of a radar signal caused by the orbital motion of the waves to determine significant wave height. This technique is significantly different from conventional Doppler techniques because there is no contamination of the sea motion broadening by the much larger Doppler broadening caused by platform motion and finite antenna beamwidth. The technique is capable of measuring the shape of the power spectrum of the Doppler-broadened echo. However, the displacement of the received center frequency from the transmitted frequency is not measured. Much of the following information is extracted from the Bush-Gotwols proposal.[9]

*Present state of the art.*—The most extensive series of Doppler-broadening measurements have been performed by the NRL (refs. 3–110 and 3–111). These measurements showed that the width of the Doppler-broadened spectrum is of the form $\omega_d = C(H_{1/3})^{1/2}$, where $C$ is a constant for a given frequency and polarization. The full width at half maximum of the Doppler-broadened spectrum $\Delta f$, will always be converted to velocity units by the use of the (nonrelativistic) Doppler relation $\Delta f = 2\Delta v_d/\lambda$. This

[6] Bush, G. B.; Katz, I.; and Kropfli, R.: APL/JHU Memorandum BPP7IU–31, 1971 (unpublished data).

[7] APL/JHU: Phase-A Study for the SEASAT–A Mission. APL/JHU, vol. 1, sec. 2.6, July 1973 (unpublished data).

[8] Bush, G. B., and Gotwols, B. L.: The Wave Motion Sensor—A new Technique for Remotely Mapping the Significant Height of Ocean Waves. APL/JHU proposal submitted to NASA Wallops Flight Center, Apr. 1974 (unpublished data).

[9] *Ibid.*

facilitates the comparison of measurements taken at different frequencies. The measurements indicated that $\Delta v_d$ was almost independent of the angle between the radar viewing direction and the predominant direction of the waves. Also, indirect evidence revealed that, because of the effect of "spray" at the air/sea interface, the Doppler broadening of horizontally polarized radiation was greater than that for the vertically polarized component. The simple relationship $\omega_d = C(H_{1/3})^{1/2}$ is used in the new technique. Katz (ref. 3–112) has previously proposed use of this relationship to measure ocean-surface roughness from a satellite by an entirely different method, which is limited to a narrow field of view.

*The platform motion problem.*—A better appreciation of the new technique will be obtained if the difficulties inherent in conventional radar Doppler-broadening measurements are first analyzed. Consider the highly simplified scheme shown in figure 3–74 in which a single high-gain antenna illuminates the surface of the ocean with a continuous wave (CW) transmission. Assume that the same antenna is simultaneously used to receive the reflected signal (ignore the associated technological difficulties). For the geometry shown in figure 3–74, the range of radial velocities between the half-power points of the antenna pattern is given approximately by

$$\Delta v_d = 2v_p\theta \qquad (3\text{–}23)$$

Assuming a highly directional antenna with a 1¼ beamwidth and a platform velocity of 7 km/sec (typical of a satellite), the full width at half maximum of the received spectrum will be approximately 244 m/sec. In contrast, the broadening caused by the orbital motion of the waves is approximately 1 m/sec for a significant wave height of 1 m. Any attempt to measure wave-motion-induced broadening is highly impractical, because the width of the composite spectrum consists of 1 part caused by orbital wave motion and 244 parts caused by platform motion. This pessimistic appraisal can be improved by considering various alternative schemes (coherent short-pulse radar, off-nadir pointing, etc.), but the improvement does not appear to be substantial enough to bring the broadening by the two mechanisms even close to equality.

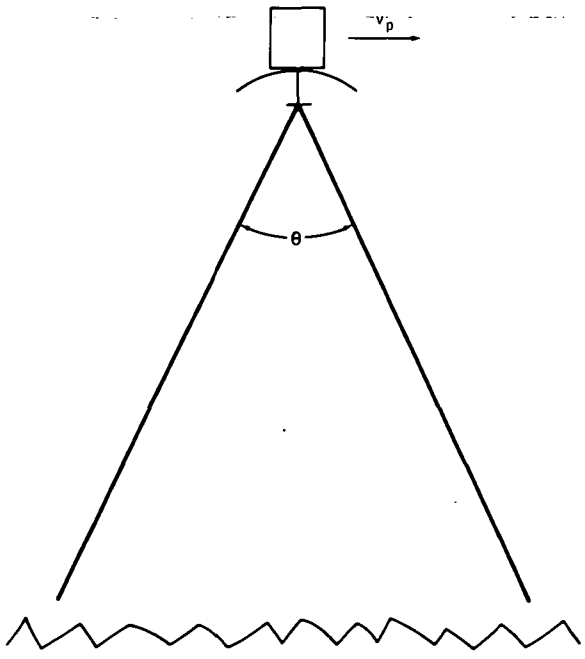


FIGURE 3–74.—Simplified diagram of a moving CW radar illuminating a rough ocean, where $v_p$ is relative platform velocity.

*The diffraction pattern in the plane of the transmitter.*—Another way to consider the broadening caused by platform motion contains the key to the solution of this problem. Consider the diffraction pattern that is formed in the plane that contains the transmitting aperture (fig. 3–75). The correlation length of the intensity fluctuations in this plane can be estimated by using the Van Cittert-Zermike theorem (ref. 3–113). This theorem states that the correlation length $l_a$ of the spatial fluctuations in the intensity caused by an extended source of diameter $L$ and at distance $h$ is given by

$$l_a = 1.22\, h\lambda/L \qquad (3\text{–}24)$$

If it is assumed that $L$ is defined by the half-power points of the antenna pattern, then (approximately)

$$L = h\theta \approx h\lambda/D \qquad (3\text{–}25)$$

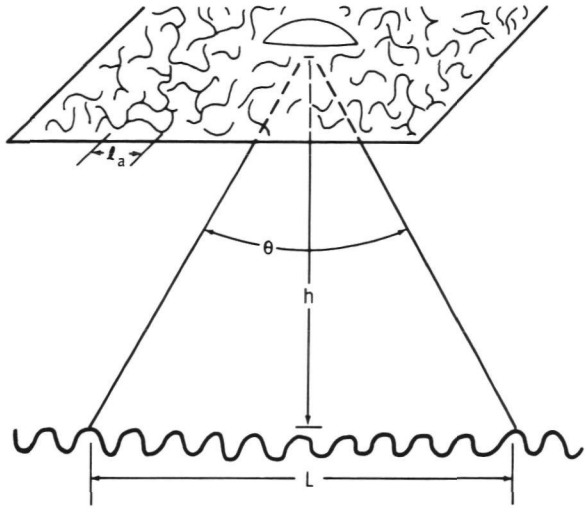


(a)

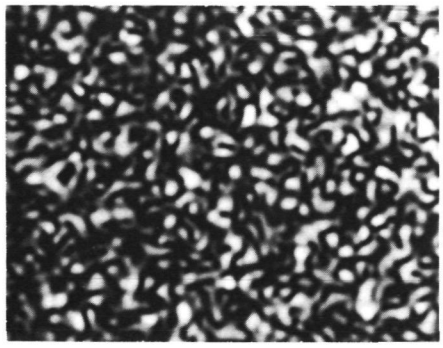

(b)

FIGURE 3–75.—Diffraction pattern. (*a*) Diagrammatic view of the diffraction pattern formed in the plane of the transmitter by radiation that is reflected from the surface of a rough ocean. (*b*) Photograph of an actual diffraction pattern created by reflecting the light from a laser off a rough surface.

where $D$ is the diameter of the transmitting aperture and $\lambda$ is the wavelength. Combining equations (3–24) and (3–25) yields the simple result

$$l_a = 1.22D \qquad (3\text{–}26)$$

By considering diffraction integral for this problem, if the transmitting aperture is moved $l$ units to the right, the (intensity) diffraction pattern will translate as a rigid body $l$ units to the left. Thus, the relative velocity between the transmitting-receiving aperture and the rest frame of the diffraction pattern of the rough ocean is $2v_p$. Therefore, the correlation length $l_a$ corresponds to a correlation time $\tau \approx l_a/(2v_p) \approx D/(2v_p)$ and to a bandwidth $\Delta f \approx 1/\tau = (2v_p)/D$. This bandwidth is identical to that given by equation (3–23) from Doppler-broadening arguments (after conversion to consistent units). This equality of bandwidths supports the theory that platform motion broadening may be analyzed either by considering the range of radial velocities intercepted by the antenna beam or by considering the transmitting-receiving antenna as moving through the diffraction pattern of the rough ocean. Thus, if a way could be found to sit at a fixed point in the rest frame of the diffraction pattern, the temporal fluctuations in the received signal that are caused by the motion of the ocean waves could be measured without having to contend with the large fluctuations caused by platform motion.

*The solution.*—The solution to the platform motion problem is to arrange a series of

receiving antennas in a line that is parallel to the relative velocity vector of the moving platform. Because the diffraction pattern translates as a rigid body in a direction opposite to the platform velocity, $N$ antennas can obtain $N$ measurements (spaced in time) of the intensity $I$ at a fixed point $x_0$ in the rest frame of the diffraction pattern. Imagine a coordinate system attached to the rest frame of the rigidly translating diffraction pattern, with the $X$-axis parallel to the velocity vector. Consider the short-term time-averaged power that an antenna centered at point $x$ delivers to its load (i.e., $P(x, t)$) rather than the intensity $I(x, t)$. Then, for each point in the diffraction pattern (e.g., $x=x_0$), the following set of measurements can be made.

$$P(x_0, t), P(x_0, t+\tau_1), P(x_0, t+\tau_2), \ldots P(x_0, t+\tau_{N-1}) \quad (3\text{–}27)$$

Thus, the autocorrelation function for $N-1$ discrete lags is

$$\{P(x, t) \cdot P(x, t+\tau_i)\} \quad (3\text{–}28)$$

where braces indicate a spatial average along the $X$-axis. Assuming that the statistical properties of the rough ocean are stationary in time and homogeneous in space, it follows from the ergodic theorem that the space and time averages are equal. Thus,

$$R_p(\tau_i) = \langle P(x_0, t) P(x_0, t+\tau_i) \rangle = \{P(x, t) \cdot P(x, t+\tau_i)\} \quad (3\text{–}29)$$

where angular brackets indicate a time average, and, because of the assumption of homogeneity, the $x_0$ argument of $R_p$ is suppressed. This result shows that the moving antenna system will obtain the same autocorrelation function as a hypothetical single stationary transmitter-receiver antenna that constructs an autocorrelation function by averaging over time.

After reasoning that the moving multi-antenna experiment is capable of measuring the same autocorrelation function as a single stationary receiving antenna, attention can be focused on the stationary antenna experiment. Because of the numerous scatterers that contribute to the reflected signal, a reasonable assumption is that the voltage induced across the output terminals of the stationary receiving antenna consists of band-limited noise with a Gaussian joint probability distribution function. The autocorrelation function of this noise voltage will be of the form

$$R_r(\tau) = v(t) v(t+\tau) = R_{vr}(\tau) \cos \omega_0 \tau \quad (3\text{–}30)$$

After linear amplification in a receiver, detection in a full-wave square-law detector, and filtering in a low-pass filter, the autocorrelation function of the short-term time-averaged power will be given by

$$R_p(\tau) = k^2 \delta^4 [1 + 2R_{vr}^2(\tau)] \quad (3\text{–}31)$$

where $k$ is a constant that depends on the receiver gain and $\delta$ is the standard deviation of $v(t)$. Thus, $R_{vr}(\tau)$ can be calculated from equation (3–31), and, in turn, the shape of the Doppler-broadened power spectrum may be obtained by taking the Fourier transform of $R_{vr}(\tau)$.

The most important difference between the stationary and moving platform equipment with $N$ antennas is restricted to obtaining $R_p(\tau_i)$ for $N-1$ discrete lags. Thus, the detail in which the power spectrum is desired will determine both the number of antennas and the separation between them. If only the width $\Delta f$ of the power spectrum is desired, the use of only two antennas with an appropriately chosen spacing should be sufficient.

A practical wave-motion sensor that uses two antennas is shown in figure 3–76. Because this configuration is not restricted to vertical pointing antennas, a wide swath could be examined.

Further investigation of the relationship between the parameters measured by the wave-motion sensor and the statistical description of the ocean is needed. The problem of how well a practical device would operate in the presence of finite receiver noise should also be analyzed.

*Surface contour radar.*—Under the sponsorship of the AAFE Program, the NRL is developing an instrument for measuring the

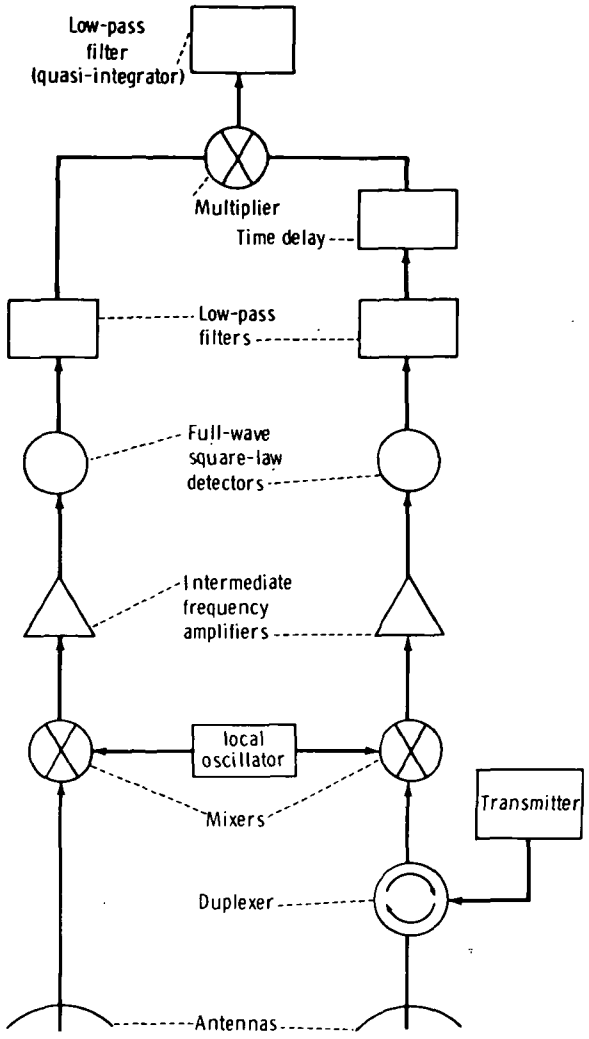


FIGURE 3–76.—A practical wave-motion sensor.

surface contours of the Earth in three dimensions. Surface contours, especially roughness of ocean surfaces, have been inferred from measurements made with other sensors; for example, scatterometers and radiometers, photography, etc. Profiling with radars or lasers provides two dimensions along the groundtrack. A sensor that profiles and scans crosstrack simultaneously will provide a three-dimensional surface contour of the sea.

Although surface contours can be measured over land and ocean areas, this discussion will be restricted primarily to coastal and ocean areas.

Scanning across the groundtrack measures the three-dimensional surface contours along the swath path from which wave heights could be determined directly. The use of data from each swath enables analysis of a slice of any angle across the Earth and determination of its spectra. Combining the analyses of slices at various angles across the swath could yield the directional wave spectra, which are fundamental to location and prediction of present and future sea-state conditions. Scanning in coastal areas will show how waves are affecting shorelines. Measuring the swells and breakers in shoaling water gives indications of the bottom topography.

*Experimental technique.*—The proposed experiment would consist of scanning a series of radar pulses crosstrack from the aircraft flightpath and recording the time and amplitude of the radar returns. The basic experimental scheme is shown in figure 3–77.

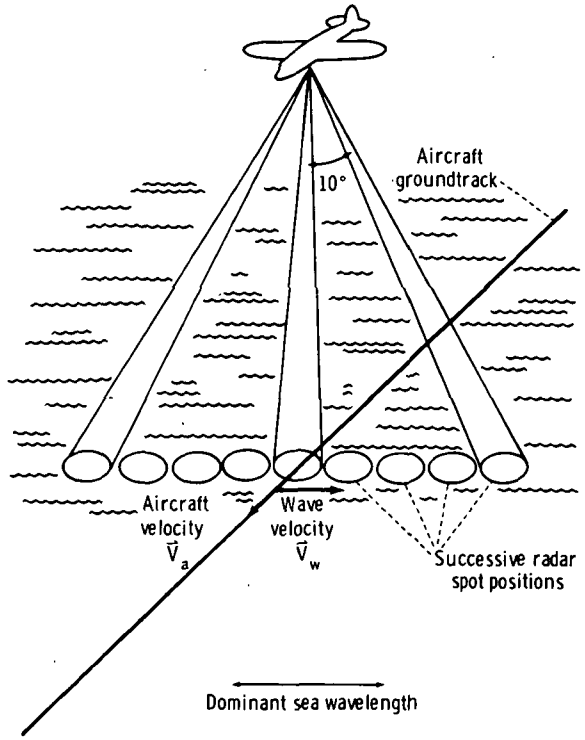


FIGURE 3–77.—Basic experimental scheme for a surface-contour radar system.

Figure 3–78 illustrates the pattern of scan on the ocean surface. The aircraft radar will operate in a beamwidth-limited mode. This choice of operation is made to avoid ambiguities that would occur in scanning a pulse-width-limited radar beam. However, the radar pulse width will still be very narrow, approximately 1 nsec, to enable resolution of the vertical structure of the sea surface.

*Observed phenomena.*—The laser has been the primary instrument for use in profiling the sea surface. However, the laser has constraints because it must operate at low altitudes and cannot penetrate clouds. The NRL (ref. 3–100) showed that a nanosecond pulse radar viewing in the vertical can profile the sea very accurately and measure the same profile and spectra that would be measured by a wave pole located in the same vicinity. The question arises as to what the radar would measure if it viewed away from the vertical. In figure 3–79, spectra measured by the radar were compared with those measured by the wave pole at angles of 0°, 10°, 20°, 30°, and 45° from the vertical, respectively. The high degree of correlation shows that only minor degradation is noted.

The understanding of ocean backscattering has just begun; thus, the factors causing disagreements between various data have to be explored. The potential offered by multiple frequencies and polarizations has not been investigated. Repeated measurements must be taken to understand the reliability of the prediction of ocean scenes from backscattering cross-section data.

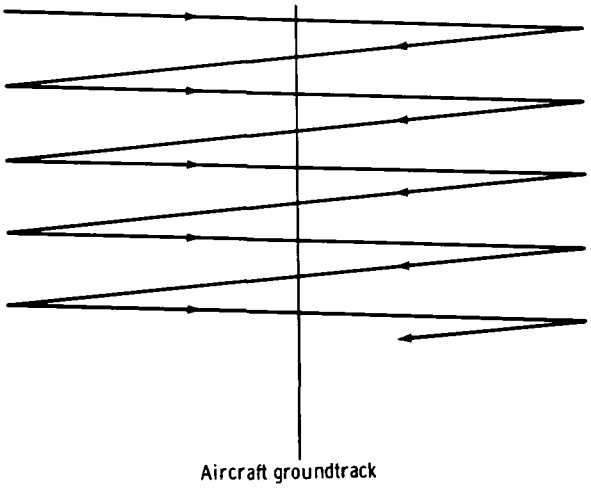


FIGURE 3–78.—Scan pattern on the ocean surface.

*Applicability.*—Scatterometer data gathered synoptically from the oceans of the world may allow production of accurate worldwide field maps and/or worldwide sea-level pressure maps.

The atmospheric sea-level pressure field specifies the conditions in the planetary boundary level or, for numerical weather prediction models, the properties of the 100 000-N/m$^2$ surface. This surface pressure field or the equivalent 100 000-N/m$^2$ surface then serves as the long-sought elusive reference surface for vertical temperature profile radiometer (VTPR) soundings; thus, the vertical structure of the entire atmosphere can be specified for numerical weather prediction models.

The height contour pattern of the planetary boundary layer 100 000-N/m$^2$ surface is complicated and consists of closed depressions and elevations corresponding to the highs and lows of conventional weather charts. If the pattern can be specified correctly, the bottom of the atmospheric soundings obtained over the oceans by the VTPR infrared sounding system, now operational on NOAA spacecraft, can be correctly related to this 100 000-N/m$^2$ reference surface, and an integration of the VTPR-computed sounding then yields the heights of all other constant pressure surfaces used in numerical weather prediction models. The most difficult part of the present use of these VTPR soundings is the determination of conditions near the sea surface, and scatterometer/altimeters can help solve this problem. Because the circulation patterns of the constant pressure surfaces become simpler with elevation and turn into the planetary wave patterns at the 100 000-N/m$^2$ surface, defining the complicated 100 000-N/m$^2$ surface correctly and integrating VTPR soundings up to the other reference surfaces will provide a more ac-

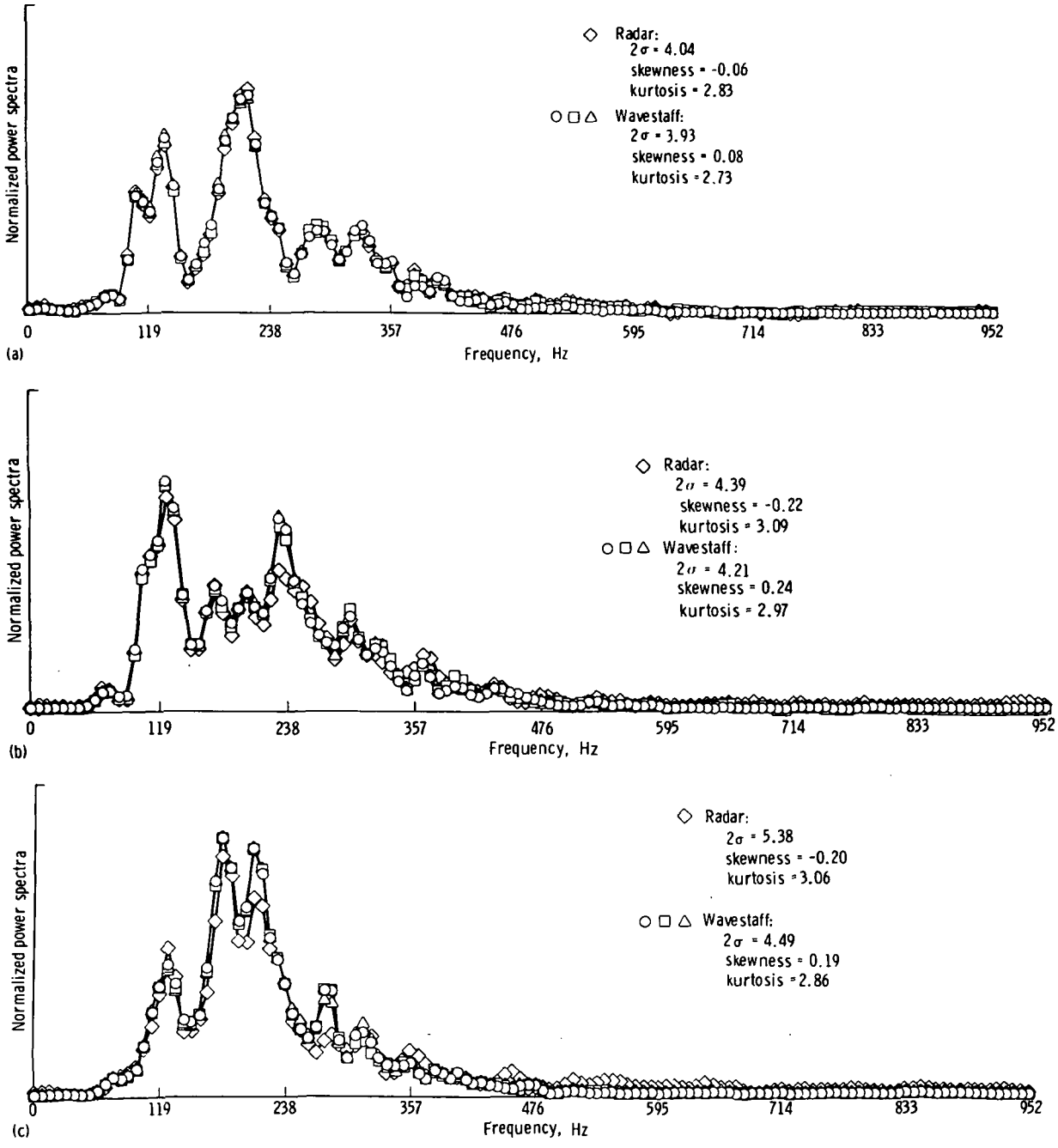


FIGURE 3–79.—Normalized power spectra for radar and wavestaffs for various look angles. (*a*) Look angle=0°. (*b*) Look angle=10°. (*c*) Look angle=20°.

curate initial value specification than, for instance, starting at a higher reference level and integrating both up and down.

*Weather forecasts.*—Improved weather forecasts on a global basis depend on (1) basic research on the physics of atmospheric, oceanic, continental, and solar interactions; (2) the development of numerical models of

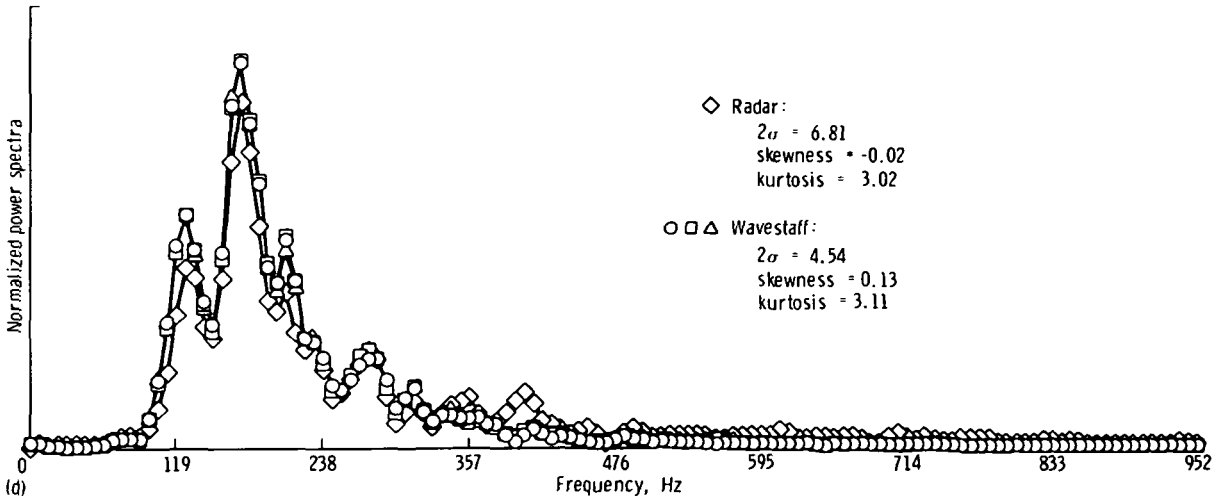


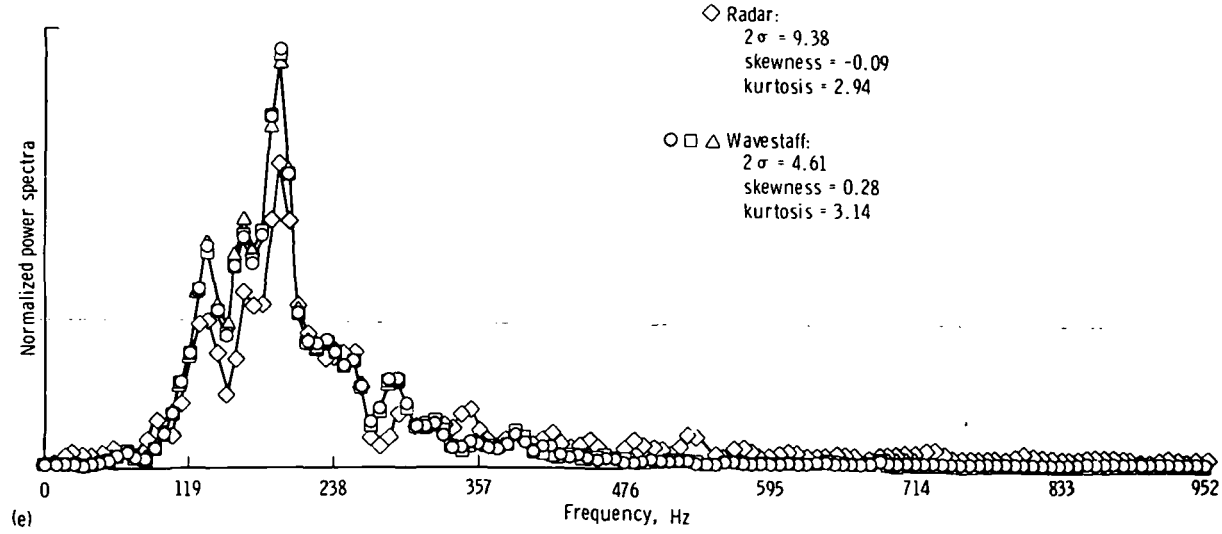


FIGURE 3–79 (concluded).—Normalized power spectra for radar and wavestaffs for various look angles. (*d*) Look angle=30°. (*e*) Look angle=45°.

the atmosphere and its interactions with the land, sea, and solar radiation; and (3) the collection of an adequate and correct data base for the initial value specification of the numerical weather forecasting model. Scatterometers will provide data for item 3 and produce an improvement in the accuracy and an increase in the range of validity of the forecasts produced by the numerical models described in item 2.

Numerical weather prediction models are continuously being refined, improved, and updated so that they can be run on computers of increasingly higher capacity and speed. Nevertheless, the models all depend on the accuracy with which the initial values are specified when the computation of the forecasted weather is started.

When random-error fields with errors of a size known to exist in the actual initial value data are introduced into a numerical model, the effects of these error fields double each day; thus, after 4 days they are 16 times as great, and the forecasted conditions no

longer agree with what actually happened. Reducing the error field in an initial value specification by a factor of 2, in effect, makes a 3-day forecast using better data as accurate as a 2-day forecast using the less-correct data.

Random-error fields are one way to study the effects of bad data; however, the situation is actually more complicated. Over the oceans, especially in the Southern Hemisphere, entire circulation patterns can be incorrectly specified as to the central pressure of a low and the horizontal extent and spacing of the isobars around the low. The proposed instruments for SEASAT–A can substantially reduce this source of error. Not only will weather forecasts over the oceans be improved by the data to be obtained, but also the forecasts over continental areas, such as the western half and the east coast of the United States, could be improved in the 2- to 3-day time frame.

Satellite-borne scatterometer systems should help improve forecasts substantially for 2 to 4 days for the Northern Hemisphere and should make possible, for the first time, 2- to 3-day forecasts for the Southern Hemisphere.

*Global heat transports.*—Another aspect of the proposed instrumentation for SEASAT–A, which includes a scatterometer, is that it provides a truly global oceanic data base, when combined with VTPR, for numerical weather prediction. The data base over the continents is reasonably adequate. Modeling interactions between the two hemispheres should be possible. Satellite heat budget studies show that the heat flux driving the Northern Hemisphere cyclones in the winter originates from as far as 30° south and has a magnitude at the Equator almost equal to the value at 40° north. The correct description on a day-to-day basis of this important global feature will be an essential step in fulfilling the stated goal of the National Weather Service of NOAA for providing reliable weather forecasts in the time range from 5 to 10 days.

*Tropical cyclones.*—An example of the value of this active microwave system is the potential contribution it can make in obtaining data on the winds and pressures on tropical cyclones wherever they occur. These tropical cyclones are called hurricanes in the North Atlantic Ocean, typhoons in the North Pacific Ocean, cyclones in the Indian Ocean, and willy-willies in the South Pacific Ocean near Australia and New Zealand. They are located by means of a characteristic cloud pattern by the NOAA Applications Technology Satellite spacecraft and tracked every 45 min or more as they move across the oceans. When their locations are known, ships avoid them almost completely. Thus, although their presence is known (recently there were four typhoons in the North Pacific Ocean at one time), their intensity and potential for damage when moving over land are not known from spacecraft data.

To determine the strength of a hurricane, the United States sends reconnaissance aircraft flights into hurricanes on a routine basis whenever they pose a threat to land. These aircraft measure the winds in the hurricane and determine the central pressure. Forecasting the movement of hurricanes is very difficult, partly because the atmosphere surrounding them is presently not well enough defined by measurements at a fine enough scale.

However, other nations do not have aircraft reconnaissance flights; although they know a hurricane is approaching, they have no information on its severity. Typhoon winds and rains caused much loss of life and damage in the Philippine Islands in 1973, and, in 1970, cyclone winds in the Bay of Bengal caused a storm surge combined with heavy rains that drowned 300 000 people in the Ganges Delta region of Bangladesh.

The problem is so acute for many nations that a special commission has been organized to attempt to find ways to obtain better data on the intensity of the surface winds in these storms as they approach populated areas. At the World Meteorological Organization meeting in Tokyo (Oct. 2 to 7, 1972), held for the study of the means of acquisition and communication of ocean data, a plea was made by the commissioner of this group for

better data on the severity of these storms. Synoptic coverage of the oceans by using satellite-borne scatterometry can solve this problem, as demonstrated by experiments performed during the Skylab Program.

The test version of this instrumentation (S193) on Skylab has scanned both a hurricane and a tropical storm in a way that may prove to have been the equivalent of having had 25 ships close enough to the storm to define the strength of the winds and the level of the central pressure.

The operational version on SEASAT–A could scan all the tropical cyclones present over the oceans twice a day and yield data on the winds and pressures. This one accomplishment would be an immediate aid to India, Burma, the Philippine Islands, many Pacific islands (such as Guam), Madagascar, New Zealand, Australia, and Mexico. Just as the adequate warning service of the National Weather Service has greatly reduced the number of lives lost and the property damage caused by hurricanes in the United States, similar benefits from this system should be possible for other nations. As more experience with the system is gained, it might be possible in a decade or more to dispense with aircraft reconnaissance of tropical cyclones.

*Wave forecasting.*—Of all oceanic phenomena, the waves, or storm seas, generated by high winds blowing over large areas of the ocean offer the most ever-present and rapidly varying patterns. The waves can grow in height from 5 m from crest to trough (as an average of the highest waves) to 17 m within 12 to 18 hr as the winds increase. Individual waves larger than 25 m from crest to trough have been measured, and waves larger than 30 m high have been estimated. Scatterometers and altimeters together can measure parameters needed for a wave forecasting model.

## PLATFORMS

### Satellites

Although the central theme of the Active Microwave Workshop is the application of active microwave systems to Earth observations, the question of integrating these systems with other sensors has to be considered. This section assesses three types of ocean-oriented spacecraft that use radar and several other types of sensors. The multisensor approach has the merit of yielding considerably more information from the simultaneous use of an array of instruments than could be obtained from their operation separately. This philosophy has been successfully used in SEASAT–A.

Three generalized types of useful oceanic observatories are: (1) a geodynamics/ocean topographic satellite, (2) an oceanic/marine atmospheric physics satellite, and (3) a marine water quality/biologic/fisheries satellite.

*A geodynamics/ocean topographic satellite.*—This system, which has evolved from the EOPAP project, would determine the marine geoid and superimposed local ocean topographic features, with the aim of understanding the space and time variations in the shapes of both surfaces caused by geodynamic and oceanographic effects and their interactions. Examples of geodynamic effects are tectonic plate motion, polar wandering, and solid Earth tides; examples of oceanographic effects are oceanic currents, deep sea tides, storm surge, and wind setup. The prime sensor would be a precision altimeter with an altitude error of approximately 2 to 5 cm, a precision that would require ionospheric, tropospheric, and ocean-wave-height corrections. The spacecraft would probably have a symmetrical drag-free configuration, laser reflectors, and satellite-to-satellite tracing capability. The orbit would be circular and inclined at 105° to 115° retrograde. By maintaining this satellite or similar ones in orbit for periods of approximately one decade, many highly significant Earth and ocean dynamics experiments could be performed, including measurements of continental drift and their relationship to earthquakes and a mapping of the major ocean currents and their time variations.

*The oceanic/marine atmospheric physics satellite.*—This spacecraft measures sea surface and maritime atmospheric parameters that help establish the near-ocean-surface

marine environment. These parameters are also of importance for weather forecasting over both land and water and for longer term climatological studies. The measurement functions of this satellite would include all-weather observations of surface and upper-level pressures, windspeeds, and directions; atmospheric profiles of water vapor, liquid water, and rainfall rates; air temperature profiles; sea-surface temperatures; wave heights, lengths, and directions; wave refractive patterns; and ice thickness, leads, polynyas, and general coverage.

The orbit would probably be circular, near-polar, and prograde, with an inclination of 75°. As such, the orbit would be non-Sun-synchronous and would process through a day/night cycle in a few weeks. The altitude would be chosen as a compromise between swath width, resolution element, power, and precision rate, but it would probably be near Earth at 1000- to 2000-km heights.

The sensor complement would include (1) an imaging radar for observing wave amplitude spectra and refractive patterns, shoreline dynamics, ice cover, and other similar features; (2) a combined scatterometer/multifrequency microwave radiometer for observing surface windspeeds and directions, atmospheric water vapor and liquid water content, and sea-surface temperature and salinity; (3) multifrequency/multiwavelength microwave and infrared sounders for determining temperature, pressure, and humidity profiles in the atmosphere; and (4) a multispectral thermal infrared imager capable of yielding quantitative land, sea surface, and cloudtop temperatures.

This combination of instruments is complex; however, the value of simultaneous observations of the relevant parameters for maritime environmental forecasts is great enough to warrant this complexity. If achievable, this second observatory would represent a highly significant advance in the data base required for a several-day global weather and maritime forecast.

*Water quality, biological assay, and fisheries identification.*—This system would rely heavily on spectral reflectivity analysis for determination of near-surface chlorophyll content, pollution, and sediment load. The required information could be derived from a multispectral imager optimized to the parameters of interest and, equally important, from data obtained by the two spacecraft mentioned previously. Of particular importance in the latter category are sea temperature, salinity, and current location.

The requirements for multispectral analyses imply a Sun-synchronous orbit and particular choices of look angle with respect to Sun angles so that illumination conditions on the ocean surface are uniformly maintained. Thus, this sensor complement may not be flown on the ocean/atmospheric physics platform, at least in a research mode, because the orbit for the research mode is deliberately designed to scan through a day/night cycle relatively quickly to observe diurnal effects. Operational spacecraft may not be so constrained, however.

Using these data, one may estimate primary biological productivity, water mass identification, sediment transport, and general condition of the ocean. Location of potential fisheries can probably be inferred from such information.

*SEASAT–A.*—This satellite is the first spacecraft dedicated to meeting in part the EOPAP objectives in ocean dynamics. The SEASAT–A is an outgrowth of a diversity of scientific and technological work conducted by NASA, the Department of Defense, the Department of Commerce, and several other institutions in both the measurement of required physical quantities and the implementation of appropriate sensors on the spacecraft and on the ground.

*Description of the program.*—SEASAT–A is a research-oriented program consisting of spacecraft precision groundtracking systems and data-processing and modeling capabilities that address both scientific and applications problems in ocean-surface dynamics. The satellite will carry an array of active radar and passive microwave and infrared instruments with the capability of observing

the ocean on a day/night near all-weather basis. This group of sensors will allow SEASAT–A to make quantitative measurements of oceanic, atmospheric, and geodetic parameters not only in clear weather but also under wind and wave conditions perhaps approaching hurricane force and over regions under persistent cloud cover.

The mission profile for SEASAT–A is tentatively as follows: lifetime, 1-yr minimum; orbit, approximately an 800-km altitude at an inclination of 108° (retrograde); eccentricity, less than 0.006 for a nearly circular orbit; and period, 100 min, resulting in 14.5 orbits/day. This orbit is nonsynchronous and will process through a day/night cycle in approximately 4.5 months. The orbit spans almost all the unfrozen oceans of the world from the Antarctic to the Alaskan North Slope and the Arctic Archipelago. The orbit is also optimum for fine-grained mapping of the geoid over the open ocean.

*Instruments and sensors.*—Each of the sensors proposed for SEASAT–A has predecessors that have been successfully flown on spacecraft and/or aircraft. Good-to-excellent assessments of the capabilities of these prototypes are available for wind and wave conditions approaching gale force, and enough is known of their theory of operation to make reasonable estimates of their performance under other, more severe environmental conditions. The selection of instruments was made to determine ocean-surface conditions in accordance with user data requirements set forth during NASA-sponsored meetings in early 1973. The sensors form a set of integrated, interactive, and mutually supporting devices, the simultaneous use of which brings about a genuinely synergistic effect wherein the total information derived from the sensor package is greater than the sum of the individual outputs. Meeting the user data requirements in their totality has not been possible because of limitations on system performance, but the five sensors described constitute a significant first step toward an optimum configuration.

Compressed pulse radar altimeter (CPRA): The CPRA has two distinct functions: the measurement of the altitude between the spacecraft and the ocean surface to an rms precision near $\pm 10$ cm and the determination of significant wave heights along the subsatellite path. When combined with accurate orbital determinations, the altitude may be used to decipher the topography of the sea surface, including spatial variations in the geoid and time variations caused by ocean dynamics.

Coherent imaging radar (CIR): Wave information will be obtained by using a CIR to obtain images of the ocean on a sampled basis. Such a radar can function through clouds and moderate rain to yield wave patterns near shorelines and in storms and can see waves with a length greater than approximately 50 m. The CIR can also provide high-resolution pictures of ice, oilspills, current patterns, and similar features. Computations can be performed on the radar data to yield a quantity called the wave directional spectrum, which gives the relative distribution of wave energy among different wavelengths traveling in various directions, and this factor, together with the surface wind velocity, is the fundamental information needed in forecasting wave conditions on the ocean.

Microwave wind scatterometer (MWS): The third radar system, an MWS, is intended to measure surface windspeed and direction by sensing the small capillary waves induced by the wind over the ocean. Previous aircraft experience and recent Skylab data taken over the Pacific Hurricane Ava in June 1973 indicate that this sensor seems useful in winds approaching 25 m/sec, yielding speeds with an error of $\pm 2$ m/sec and directions to $\pm 20°$.

In the SEASAT–A configuration, the output of the scatterometer will be measurements of lower windspeeds and directions taken over two 450-km-wide swaths equally displaced about the vertical by 300 km. In 12 hr, these swaths map out a quiltlike pattern of areas over the portion of the oceans between 72° north and 72° south latitude with enough density of observations so that an essentially complete chart of surface winds will be obtained.

An experimental variation of the MWS, termed the "wave spectrometer," is expected to be operated simultaneously with the MWS as an alternative, less complicated, and less complete method of obtaining wave directional spectra along a 300-km-wide swath about the vertical.

Scanning multifrequency microwave radiometer (SMMR): The SMMR is a passive microwave device that simultaneously senses the microwave energy emitted by and reflected from the ocean, ice, and atmosphere. To separate the various contributions to the signal from these sources, several microwave frequencies (6, 10, 18, 21, and 37 GHz) are used, each chosen for maximum sensitivity to one of those geophysical parameters. The scanning feature will enable low-resolution images of objects along its line of sight to be constructed from the signals received.

The SMMR serves several functions. First, the SMMR is a windspeed instrument that senses the increase in emitted microwave energy caused by roughness, foam, and streaks on the ocean when higher windspeeds create wave breaking and whitecaps. The estimated observable range of speeds is from approximately 10 m/sec to perhaps 50 m/sec. The upper limit has yet to be firmly established. Thus, the range of speeds measurable from SEASAT should be extended by the SMMR from the 25-m/sec limit of the scatterometer up toward hurricane-force winds. Second, the SMMR appears capable of measuring sea-surface temperature with an accuracy of 10 K even through light clouds where present infrared devices are useless. Third, the other frequencies are used for determining atmospheric liquid water and water vapor content, quantities that are needed for models of oceanic and atmospheric boundary-layer processes and for important corrections to the precision altimeter measurements. Icefields and ice cover will also be observed with low resolution from the SMMR.

Maps of higher ocean-surface winds, temperatures, and overlying atmospheric water content will be the output of the SMMR. These maps will be combined with the wind data from the MWS to yield a global quantitative chart of windspeed below hurricane force. The measurements will be equivalent to some 20 000 ship reports a day. When these measurements are combined with available ship and buoy surface information on wind and pressure, the atmospheric pressure field over the entire ocean, except perhaps near reserve storms, can be computed. This computation will also be possible in the data-sparse Southern Hemisphere. Such results should help improve the 24-hr weather forecasts substantially. This improved predictive capability for winds implies an approximately equal improvement in forecasting waves, especially when assisted by the data on the initial state of the sea obtained from the radar altimeter and imager.

Infrared radiometer (IRR): The purpose of this sensor is to provide images of thermal infrared emission from ocean, coastal, and atmospheric features that will help interpret the measurements from the other four microwave instruments. In addition, the IRR will have atmospheric correction channels that will enable temperatures to be deduced from the imagery with a precision of better than 1 K in clear air. The device will be similar to scanning radiometers flown on Nimbus and the NOAA Improved Tiros Operational Satellite.

*The total system.*—The informational output of the instrument complement will constitute three classes. The first class will be measurements of wave height, wave directional spectrum, and surface windspeed and direction over the global ocean with a repeat time of 12 to 36 hr on a somewhat uneven grid that is at least as fine as 250 km in most parts of the world. The second class will be sea-surface topography from which currents, setup tides, and other similar features may be deduced in selected regions over a time scale of days or weeks. The third class is high-resolution imagery, both radar and infrared, made over selected areas at specified times on selected time and space scales.

The interrelationships among these several

classes of data are presented in table 3–XI, which illustrates the complex nature of the contribution that each sensor makes to the geophysical parameters being measured. Table 3–XI indicates the importance of carrying the full sensor complement to achieve the measurement objectives.

SEASAT–A is thus an integrated observatory addressing the objectives discussed previously. Table 3–XII outlines the capabilities of the spacecraft system in meeting the requirements set forth by the users at the start of the program. Not all of the desiderata have been met; in particular, the operationally determined requirements demand more than one spacecraft. Thus, the request for continuous coverage of wind and waves with an update every 12 hr, the desire for 100-km surface resolution on the SMMR channels, and the requirement for all-weather temperature resolution of 0.25 K have been impossible to achieve. It does not appear feasible to reach a global overall ±10-cm accuracy in geoid, altimeter, and tracking needed to reduce the ultimate errors in current measurements to the level of 20 cm/sec. These considerations must await further work.

Nevertheless, these data will be valuable for both research purposes and for demonstration of near-operational uses in marine and weather forecasting. The program plan calls for assembling all the data in compatible format through a command and control center at the Goddard Space Flight Center, reducing and interpreting them as geophysical quantities, and disseminating them to research scientists in an orderly way. In addition, on a few occasions during the life of the satellite, a real-time quasi-operational exercise will be conducted in which the wind/wave/imagery information will be sent out on communications channels to users, such as the NOAA National Meteorological Center or the Department of Defense Fleet Nu-

TABLE 3–XI.—*Physical Parameter Measurement Methods*

| Measurements and sensors | Physical parameters | | | | | | | | |
|---|---|---|---|---|---|---|---|---|---|
| | Atmospheric water content | Surface winds, speed, and direction | Wave heights, length, and direction | Wave near shores and storms | Geoidal heights | Surface currents, speed, and direction | Tides, tsunamis, setups, storm surges | Sea surface temperatures | Ocean, ice, atmosphere, and land features |
| Radar backscatter (scatterometer) | | X | X | | | | | | X |
| Microwave emission (microwave radiometer) ..... | X | X | X | | | X | | X | X |
| Altitude and roughness (radar altimeter) ..... | | X | X | X | X | X | X | | X |
| Radar images (imaging radar) | | X | X | X | | X | | | |
| Infrared images (IRR) ..... | X | | | | | X | | X | X |
| Ocean geoid (external data) | | | | | X | X | X | | X |
| Satellite position (external data) | X | X | X | X | X | X | X | X | X |
| Other observations (external data) | X | X | X | X | X | X | X | X | X |

TABLE 3–XII.—*Capability of SEASAT–A in Meeting User Requirements*

| Physical parameter | Instruments | Range [a] | Precision | Resolution or IFOV [b] | Total FOV [c] | Comments |
|---|---|---|---|---|---|---|
| Wave height $H_{1/3}(x, y)$ | Pulse altimeter and coherent altimeter | 1.0 to 20 m | ±0.5 m or ±10 percent | 2- by 7-km spot | 2-km swath | Along subsatellite track only |
| Directional sea wave spectrum $\psi(\lambda, \theta, x, y)$ | Imaging radar (two-dimensional transform) | $\psi$: Unknown<br>$l_w$: 50 to 1000 m<br>$\theta_w$: 0 to 360° | $\psi$: —<br>$l_w$: ±10 percent<br>$\theta_w$: ±10° | 50-m resolution | 20- by 20-km squares | Global samples at 250-km intervals |
| | Two-frequency wave spectrometer | $\psi$: Unknown<br>$l_w$: 6 to 500 m<br>$\theta_w$: 90° sector | $\psi$:—<br>$l_w$: ±10 percent<br>$\theta_w$: ±90° | 8- by 25-km spot | 300-km swath about nadir | Global samples at 150-km intervals |
| Surface wind field $W(x, y)$ | Scatterometer | $W$: 3 to 25 m/sec<br>$\theta_w$: 0 to 360 | ±2 m/sec, ±10 percent; ±20° | ≤50-km spot | Two 450-km swaths | Global, 36 hr (low speeds) |
| | Microwave radiometer | $W$: 10 to 50 m/sec<br>$\theta_w$: Unknown | ±2 m/sec, ±10 percent | ≤100-km spot | 900-km swath about nadir | Global, 36 hr (high speeds) |
| Surface temperature field $T(x, y)$ | IRR | −2 to 35 K | ±.25 to 1 K | 1- to 17-km IFOV | 1500-km swath about nadir | Global, 36 hr (clear air only) |
| | Microwave radiometer | 0 to 35 K | ±1.5 K | 100-km spot | 900-km swath about nadir | Global, 36 hr (clouds and light rain) |
| Geoidal heights $h(x, y)$ (above reference ellipsoid). | Pulse altimeter and coherent altimeter | 7 cm to 200 m | ±7 cm | 2- by 7-km spot | 18-km spacing along equator | Sampled throughout 1 yr |
| Sea surface topography $J(x, y)$ (departures from geoid). | Pulse altimeter and coherent altimeter | 7 cm to 10 m | ±7 cm | 2- by 7-km spot | 2-km swath | Along subsatellite track only |
| Oceanic, coastal, and atmospheric features (patterns of waves, temperature, currents, ice, oil, land clouds, and atmospheric water content). | Imaging radar | High resolution | All weather | 25 or 100 m | 100 or 200 km | Sample directly or stored images |
| | IRR | High resolution | Clear air | 1 to 7 km | 1500-km swath | Broadly sampled images |
| | Microwave radiometer | Low resolution | All weather | 15 to 100 km | 900-km swath | Global images |

[a] The $l_w$ is wavelength of waves, $\theta_w$ is directional angle of the waves, and $W$ is windspeed.
[b] Instantaneous field of view.
[c] Field of view.

merical Weather Center, with less than a 3-hr delay. Another exercise visualized is one in which near real-time radar images of the icefields along the Northwest Passage are obtained and estimates are made of their usefulness to real or hypothetical ship passages.

An important element in interpreting the SEASAT–A data and extending its utility will be a combination of the information obtained from this spacecraft and the considerable data on oceans and atmosphere available from other sources. The environmental/meteorological satellites, ships, buoys, and transoceanic aircraft are obvious sources for marine and weather data. In the case of ocean-wave forecasts, a land-based high-frequency skywave radar that is intended for operational detailed monitoring of wave spectra near the continental United States is expected to be in service. Its fine-grained data complement the necessarily coarser-space open ocean-wave spectral data from SEASAT–A. Similarly, research data on currents, tides, the geoid, and the other parameters of interest will be amalgamated with the SEASAT–A data by individual researchers interested in specific problems.

*Scientific problems.*—In addition to being an applications satellite, SEASAT–A will be an important research tool in several areas of geophysics, as shown by the following list of scientific problems that it can address.

Oceanography: The mapping of major ocean currents and their time and space variations in selected regions will be achievable by a combination of infrared imagery to yield positions and precision altimetry for estimates of surface speeds.

Global deep-sea tides should be extractable from altimetry measurements with errors of perhaps a few tens of centimeters during a year of data taking; in contrast, only a few dozen measurements of open ocean tides presently exist.

*Altimeter sensing of a tsunami in the Pacific Ocean* may be possible if one or more of those earthquake-caused waves occurs during the lifetime of the satellite. The information obtained may assist in determining the energy content of the tsunami and help reduce the problem of overwarning that now exists. However, an operational warning system cannot be predicated on the basis of satellite altimetry.

Ice dynamics can be studied with repeated radar imagery taken in the polar regions. The size and extent of leads and cracks establish the heat exchange between air and water and, hence, determine much of the weather in those regions.

The generation, spatial distribution, and radiation of waves by storms and hurricanes may be investigated with radar imagery. Using detailed wave spectra, wave/wave interaction may be studied as a process that cascades energy from short to long waves, which result in high sea states. Little is known quantitatively about the surface-wave regime on continental shelves under severe storm conditions. Similarly, interactions of storm surf with shorelines and coastal structures can be observed during bad weather.

*Oceanographers have never been able to* gain the overview of their domain required to understand synoptic or planetary scale events in the sea. The SEASAT–A should provide a very important vantage point for that view.

Boundary-layer meteorology: The greatly increased knowledge of the surface temperature, wind, and pressure fields over the oceans will aid in understanding large-scale atmospheric circulation and air/sea heat exchange. The effects of the sea temperature on hurricane growth, jetstream deflection, and global climatology may be illuminated by these measurements. Poleward transport of heat by oceanic currents can be assessed more accurately, and the effect on the overall heat balance can be assayed.

Geodetic science: The prime geodetic output of SEASAT–A will be a precise fine-scale equipotential surface (geoid) over the ocean. *This measure of the Earth may be used to* determine gravimetric deflections of the accuracy of the new North American datum. Gravity anomalies caused by large underwater features such as sea mounts and

trenches may also be observed. The discrepancies between spirit leveling and sea-level measurements along the coasts may be resolved by the precise knowledge of sea-surface topography.

The improved gravity fields should result in more accurate satellite orbital determination. The influence of polar wandering and other nonrigid Earth motions may be measured more readily, and the origins of the motions can be sought using orbital analysis and accurate tracking.

Engineering science: A high-technology system such as a spacecraft always results in many important developments in technology and engineering science. Although it is difficult to specify exactly what the yield of SEASAT–A in this regard will be, a safe speculation would be that significant advances are expected in areas of short pulse and coherent radars, in tracking technology, and perhaps in data handling and dissemination. Other technologies presumably will be upgraded during the program.

### Aircraft

Aircraft provide mobile, variable altitude platforms to fulfill four needs:

1. Providing a relatively inexpensive means to field test hardware.
2. Collecting data to verify theoretical models.
3. Collecting ground-truth data to verify the performance of satellite systems.
4. Conducting near-shore fine-scaled quick-response studies.

For many features, the temporal requirements for observation in the coastal region are considerably more frequent than for the open ocean. For specific coastal phenomena, such as circulation, the observation may well be tidally dependent and require multiple observations during the tidal cycle. Observations should be sensitive to seasonal variations and persistent wind conditions. However, continuous observations over extended periods and regions are not required and can be accomplished on a geographically selective basis. Hence, the aircraft platform complements satellite systems by increased temporal coverage for coastal requirements.

Aircraft in the aerospace program have been used for testing and establishing feasibility for space techniques and for providing several levels of monitoring in multistage sampling systems. These roles will continue for microwave development and for sea truth and instrument validation for experimental and operational satellite systems. Because of spatial resolution limitations of microwave systems and increased levels of temporal coverage needed for coastal operations, aircraft rather than geostationary platforms will be responsible primarily for active microwave selective coverage in the coastal region. Hence, imaging radar systems developed for aircraft can play an operational role in understanding coastal dynamics.

### Lighter-Than-Air Airships

A unique opportunity exists with the station-keeping capability of relatively vibration-free airships. The plan position indicator radar (without clutter rejection circuits) can be combined with time-lapse photography techniques to monitor wave refraction effects in a continuous manner. In particular, wave energy focusing effects can be quantitatively evaluated over regions with approximately a 30- to 50-km radius, which is sufficient for many coastal activities.

The dirigible can monitor specific activities at sea on a very economical basis. Such activities include fishing operations and dumping of wastes into the ocean. For research, dirigibles offer the advantage of maintaining a specific area of ocean in the field of view of its instrument payload with varying observation angles, solar angles, etc.

Some benefits that ocean scientists could derive if they used the unique range, load, endurance, and flight characteristics potentially offered by airships are as follows:

1. Mounting of the largest microwave antennas ever flown.
2. Shortening of transit times (compared to ships) to remote ocean observation areas.

3. Unsurpassed staying power compared to airplanes or helicopters.
4. Stable and vibration-free flight.
5. Roominess onboard and good habitability characteristics.
6. Ability to carry a variety of oceanographic sensors, including very large listening arrays that can be towed without self-generated hull and propeller noise.
7. Capability to process observational data in flight and repeat the experiments on scene if required.
8. Opportunity to observe remotely from the air and simultaneously sample the ocean in situ for ground truth.

Being a function of volume, their performance could be tailored to the particular ocean work assignment involved. Nonrigid airships (the so-called blimp type) could be sized at approximately 0.1 million cubic meters for coastal work. Larger airships of the rigid or structural class, perhaps 0.55 million cubic meters, would be used for protracted mid-ocean missions. Ocean-related payloads might range from 5000 to 35 000 kg. Maximum speeds should exceed 60 m/sec. Refueling from surface ships or use of nuclear propulsion, for which lighter-than-air airships are peculiarly suited because of their low energy requirements, would insure impressive station-keeping capabilities.

### Data Collection Platforms

The NASA Synchronous Meteorological Satellite A (SMS–A) was launched in June 1974. The SMS–B is to be launched in January 1975. The backup satellite, the NOAA GOES–A, is scheduled to be launched in August 1975. The GOES–A will be stored in orbit to replace either SMS–A or SMS–B should the need arise.

The subpoint locations for SMS–A and SMS–B are expected to be near 75° and 135° west longitude, respectively. The first satellite will be temporarily located near 100° west longitude. The second satellite will be positioned near 20° west longitude to support the GARP Atlantic Tropical Experiment (GATE). At the conclusion of GATE, the satellites will be moved to their designated operating positions.

From the Earth-synchronous orbit, 35 000 km above the Equator, the satellite will (1) provide near-continuous day/night imaging of the Earth surface and cloud cover over an area with a radius of at least 55° great circle around the satellite subpoint; (2) rebroadcast that imagery in a "slowed-down" mode for direct reception by suitably equipped regional user stations; (3) monitor the space environment in terms of solar energetic particles, X-rays, and the geomagnetic field; (4) broadcast environmental service products such as charts, analyses, and advisories to remote locations; and (5) collect and relay environmental data sensed by a variety of widely dispersed in situ platforms such as river and rain gages, seismometers, tide gages, buoys, ships, and automatic weather stations.

For the environmental data collection subsystem, the spacecraft is being designed with a capacity to collect and relay environmental observations from 10 000 or more individual observing platforms within each 6-hr period. Sensor data will be transmitted to the spacecraft either in an interrogated or self-timed mode of operation, using frequencies in the lower ultrahigh frequency (400 to 500 MHz) band. The preferred data format is the American Standard Code for Information Exchange, which is the U.S. Government standard, and is computer compatible. A platform equipped with a 10-dB gain antenna and a 5-W transmitter can operate effectively at an antenna elevation angle of 7.5°. The data received at the satellite will be transponded at S-band frequencies (nominal 1694 MHz). Data collected from these platforms will be relayed through the satellite and acquired by the National Environmental Satellite Service (NESS) Command and Data Acquisition Station at Wallops, Va., and relayed to a central location in Washington, D.C. As the program evolves to a fully operational status, these data will be disseminated routinely in a standard format over environmental data communications circuits.

The long-awaited plan for the operational GOES data-collection subsystem is nearing completion. The plan includes a questionnaire to be completed by those planning to establish data collection platforms. The responses to the questionnaire will be used by NESS to evaluate the need for the service, assign the channels to be used, and determine priorities for collection. Interface requirements for the self-timed and interrogated data-collection platform radio sets have been developed.

The system will be available for international participation by environmental services agencies/organizations in programs of mutual interest. Consistent with World Meteorological Organization practices, participating user agencies will bear the cost of the in situ platforms and environmental sensors, the radio equipment to establish the platform-satellite communications link, and the standard communications terminal equipment (teletypewriters) in their operating facilities. If the user has a unique need for dissemination from Washington, D.C., he may choose to provide, at his cost, for special communications between his facility and Washington, D.C.

The use of the data-collection system will be limited to the collection of environmental data in accordance with applicable International Telecommunication Union regulations concerning use of the allocated frequency bands. Environmental data are defined as observations and measurements of the physical, chemical, or biological properties of the oceans, rivers, lakes, solid Earth, and atmosphere (including space).

## REFERENCES


3–1. APEL, J. R., AND SHERMAN, J. W. III: Monitoring the Seas From Space: NOAA's Requirements for Oceanographic Satellite Data. NOAA Rep. AOML–LORS (Miami, Fla.), June 1973.

3–2. U.S. COAST GUARD: An Analysis of the Potential Applications of Space Telecommunications Systems to U.S. Coast Guard Missions. Contractor Report by Westinghouse Defense and Electronics Systems Center, Baltimore, Md., 1975. (Available from the National Technical Information Service, Springfield, Va.)

3–3. CROMBIE, D. D.: Doppler Spectrum of Sea-Echo at 13.56 Mc/s. Nature, vol. 175, 1955, pp. 681–682.

3–4. KERR, D. E., ed.: Propagation of Short Radio Waves. MIT Radiation Laboratory Series, vol. 13, McGraw-Hill Book Co., 1951.

3–5. RUCK, GEORGE T.; BARRICK, DONALD E.; STUART, WILLIAM D.; AND KRICHBAUM, CLARENCE K.: Rough Surfaces. Radar Cross Section Handbook, vol. II, Ch. 9, Plenum Press, 1970.

3–6. SKOLNIK, MERRIL IVAN, ed.: Sea Echo. Radar Handbook. Ch. 25, McGraw-Hill Book Co., 1970.

3–7. WRIGHT, JOHN W.: A New Model for Sea Clutter. IEEE Trans. Antennas Propagat., vol. AP–16, no. 2, Mar. 1968, pp. 217–223.

3–8. BARRICK, D. E.: First-Order Theory and Analysis of MF/HF/VHF Scatter From the Sea. IEEE Trans. Antennas Propagat., vol. AP–20, no. 1, Jan. 1972, pp. 2–10.

3–9. CHAN, H. L., AND FUNG, A. K.: Backscattering From a Two-Scale Rough Surface With Application to Radar Sea Return. NASA CR–2327, 1973.

3–10. CHIA, R. C.: The Theory of Radar Scatter From the Ocean. CRES TR–112–1, Center for Research in Engineering Science, Univ. of Kansas, Oct. 1968.

3–11. KATZIN, MARTIN: On the Mechanisms of Radar Sea Clutter. Proc. IRE, vol. 45, no. 1, Jan. 1957, pp. 44–54.

3–12. SCHOOLEY, ALLEN H.: Upwind-Downwind Ratio of Radar Return Calculated From Facet Size Statistics of a Wind-Disturbed Water Surface. Proc. IRE, vol. 50, no. 4, Apr. 1962, pp. 456–461.

3–13. VALENZUELA, G. R.: Depolarization of EM Waves by Slightly Rough Surfaces. IEEE Trans. Antennas Propagat., vol. AP–15, no. 4, July 1967, pp. 552–557.

3–14. MOORE, R. K.; CLAASSEN, J. P.; FUNG, A. K.; WU, S. T.; AND CHAN, H. L.: Toward RADSCAT Measurements Over the Sea and Their Interpretation. CRES TR–186–6, Center for Research in Engineering Science, Univ. of Kansas, Aug. 1971.

3–15. PIERSON, W. J., JR., AND STACY, R. A.: The Elevation, Slope, and Curvature Spectra of a Wind Roughened Sea Surface—Final Report. NASA CR–2247, 1973.

3–16. WU, S. T., AND FUNG, A. K.: A Non-Coherent Model for Microwave Emission and Backscattering From the Sea Surface. J. Geophys. Res., vol. 77, no. 30, Oct. 1972, pp. 5917–5929.

3–17. VALENZUELA, G. R.: Scattering of Electromagnetic Waves From a Tilted Slightly Rough Surface. Radio Sci., vol. 3, no. 11, Nov. 1968, pp. 1057–1066.

3–18. GUINARD, N. W., AND DALEY, J. C.: An Experimental Study of a Sea Clutter Model. Proc. IEEE, vol. 58, no. 4, 1970, pp. 543–550.

3–19. BRADLEY, G. A.: Remote Sensing of Ocean Winds Using a Radar Scatterometer. Ph.D. Dissertation, Univ. of Kansas, 1972.

3–20. CLAASSEN, J. P.; FUNG, A. K.; MOORE, R. K.; AND PIERSON, W. J.: Radar Sea Return and the Radscat Satellite Anemometer. Proceedings of Engineering in the Ocean Environment (Newport, R.I.), Sept. 1972, pp. 180–185.

3–21. SUTHERLAND, A. J.: Spectral Measurements and Growth Rate of Wind Generated Water Waves. Tech. Rep. 84, Stanford Univ., Dept. of Civil Engineering, Aug. 1967.

3–22. STOGRYN, A.: The Apparent Temperature of the Sea at Microwave Frequencies. IEEE Trans. Antennas Propagat., vol. AP–15, no. 2, Mar. 1967, pp. 278–286.

3–23. COX, C., AND MUNK, W.: Measurements of the Roughness of the Sea Surface From Photographs of the Sun's Glitter. J. Opt. Soc. Amer., vol. 44, no. 11, Nov. 1954, pp. 838–850.

3–24. ULABY, F. T., AND FUNG, A. K.: Effects of Roughness on Emissivity of Natural Surfaces in the Microwave Region. IEEE Southwest Conf. Proc., Apr. 1970, pp. 436–440.

3–25. LYNCH, P. J., AND WAGNER, R. J.: Rough-Surface Scattering: Shadowing, Multiple Scatter and Energy Conservation. J. Math. Phys., vol. 11, no. 10, Oct. 1970, pp. 3032–3042.

3–26. WILLIAMS, G. F., JR.: Microwave Radiometry of the Ocean and the Possibility of Marine Wind Velocity Determination From Satellite Observations. J. Geophys. Res., vol. 74, Aug. 20, 1969, pp. 4591–4594.

3–27. DROPPLEMAN, J. D.: Apparent Microwave Emissivity of Sea Foam. J. Geophys. Res., vol. 75, Jan. 1970, pp. 696–698.

3–28. NORDBERG, W.; CONAWAY, J.; AND THADDEUS, P.: Microwave Observations of Sea State From Aircraft. Quart. J. Roy. Meteorol. Soc., vol. 95, Apr. 1969, pp. 408–413.

3–29. HOLLINGER, JAMES P.: Passive Microwave Measurements of the Sea Surface. J. Geophys. Res., vol. 75, no. 27, Sept. 1970, pp. 5209–5213.

3–30. ROSS, DUNCAN B.; CARDONE, VINCENT J.; AND CONAWAY, JACK W., JR.: Laser and Microwave Observations of Sea Surface Conditions for Fetch-Limited 17- to 25-M/S Winds. IEEE Trans. Geosci. Electronics, vol. GE–8, no. 4, Oct. 1970, pp. 326–336.

3–31. NORDBERG, W.; CONAWAY, J.; ROSS, D. B.; AND WILHEIT, T. T.: Measurements of Microwave Emission From a Foam Covered, Wind Driven Sea. J. Atmos. Sci., vol. 28, Apr. 1971, p. 429.

3–32. HOLLINGER, JAMES P.: Passive Microwave Measurements of Sea Surface Roughness. IEEE Trans. Geosci. Electronics, vol. GE–9, no. 3, July 1971, pp. 165–169.

3–33. STOGRYN, A.: Equations for Calculating the Dielectric Constant of Saline Water. IEEE Trans. Microwave Theory Tech., vol. MTT–19, no. 8, Aug. 1971, pp. 733–736.

3–34. BARRICK, D. E.: Wind Dependence of Quasi-Specular Microwave Sea Scatter. IEEE Trans. Antennas Propagat., vol. AP–22, 1974, pp. 135–136.

3–35. KRISHEN, K.: Detection of Oil Spills Using 13.3 GHz Radar Scatterometer. J. Geophys. Res., vol. 78, no. 12, Apr. 1973, pp. 1952–1963.

3–36. WRIGHT, JOHN W., AND KELLER, W. C.: Doppler Spectra in Microwave Scattering From Wind Waves. Phys. Fluids, vol. 14, no. 3, Mar. 1971, pp. 466–474.

3–37. SHEMDIN, O. H.; LAI, R. J.; REECE, A.; AND TOBER, G.: Laboratory Investigation of Whitecaps, Spray and Capillary Waves. Tech. Rep. 11, Coastal and Oceanographic Engineering Laboratory, Florida Univ., Dec. 1972.

3–38. WRIGHT, J. W.; KELLER, W. C.; AND DUNCAN, J. R.: Fetch and Windspeed Dependence of Doppler Spectra. Radio Sci., vol. 9, Oct. 1974, pp. 809–819.

3–39. STILWELL, DENZIL, JR.: Directional Energy Spectra of the Sea From Photographs. J. Geophys. Res., vol. 74, no. 8, Apr. 1969, pp. 1974–1986.

3–40. SVERDRUP, HENRY U., AND MUNK, W. H.: Wind, Sea and Swell: Theory of Relations for Forecasting. Pub. No. 601, U.S. Navy Hydrographic Office, 1947.

3–41. APEL, J. R.; PRONI, J. R.; AND CHARNELL, R. F.: Observations of Oceanic Internal and Surface Waves Using Remote Sensing Techniques. J. Geophys. Res., Feb. 1975. (To be published.)

3–42. DOLAN, R.: Coastal Land Forms: Crescentic and Rhythmic. Geol. Soc. Amer. Bull., vol. 82, Jan. 1971, pp. 177–180.

3–43. GREENWOOD, J. ARTHUR, ET AL.: Oceanographic Applications of Radar Altimetry From a Spacecraft. Remote Sensing Environ., vol. 1, no. 1, Mar. 1969, pp. 71–80.

3–44. VINCENT, S., AND MARSH, J. G.: Global De-

tailed Gravimetric Geoid. NASA TM X–70492, 1973.

3–45. VONBUN, F. O.: Spacecraft Missions and Experiments Important to Geodynamics. The XVII Plenary Meetings, COSPAR (São Paulo, Brazil), 1974.

3–46. KOLKER, M., AND WEISS, E.: Space Geodesy Altimetry Study. NASA CR–1298, 1969.

3–47. VON ARX, W. S.: Absolute Dynamic Topography. Limnol. Oceanogr. Suppl., vol. 10, 1965, pp. R265–R273.

3–48. VON ARX, W. S.: An Oceanographic Satellite. Proceedings of the Joint Oceanographic Assembly (Tokyo), 1971, p. 112.

3–49. ROME, H. J., AND CRUMP, E.: Near Real-Time Estimation of Vertical Deflections at Sea. IEEE International Conference on Engineering in the Ocean Environment, 1973, pp. 549–559.

3–50. MCGOOGAN, J. T.; LEITAO, C. D.; WELLS, W. T.; MILLER, L. S.; AND BROWN G. S.: Skylab Altimeter Applications and Scientific Results. AIAA Conference on Scientific Experiments of Skylab (Huntsville, Ala.), Oct. 30 to Nov. 1, 1974.

3–51. MILLER, L. S., AND BROWN, G. S.: Engineering Studies Related to the Skylab Program. NASA CR–137462, 1974.

3–52. CREPON, M.: Influence de la pression atmospherique sur le niveau moyen de la Mediterranée Occidentale et sur le flux à travers le détroit de Gibraltar. Ashiers Oceanographiques, 15, 1964.

3–53. KAULA, W. M., ed.: The Terrestrial Environment: Solid Earth and Ocean Physics. NASA CR–1579, 1970.

3–54. THIERET, D.: Geole—Système d'Aide à la Géodesie. Centre National d'Etudes Spatiales, PR/AM/DA 72–T–62, 1972.

3–55. HENDERSHOTT, M. C.: The Effects of Solid Earth Deformation on Global Ocean Tides. Geophys. J. Roy. Astron. Soc., vol. 29, 1972, pp. 389–402.

3–56. PEKERIS, C. L., AND ACCAD, Y.: Solution of Laplace's Equations for the $M_2$ Tide in World Oceans. Phil. Trans. Roy. Soc. London, Ser. A265, 1969, pp. 413–436.

3–57. MUNK, WALTER H., AND CARTWRIGHT, D. E.: Tidal Spectroscopy and Prediction. Phil. Trans. Roy. Soc. London, Ser. A259, 1966, pp. 533–581.

3–58. ZETLER, BERNARD D., AND MAUL, GEORGE A.: Precision Requirements for a Spacecraft Tide Program. J. Geophys. Res., vol. 76, no. 27, 1971, pp. 6601–6605.

3–59. CARTWRIGHT, D. E.: Tides and Waves in the Vicinity of St. Helena. Phil. Trans. Roy. Soc. London, Ser. A270, 1971, pp. 603–649.

3–60. MUNK, WALTER H., AND ZETLER, BERNARD D.: Deep-Sea Tides: A Program. Science, vol. 158, no. 3803, 1967, pp. 884–886.

3–61. FOMIN, LUCK M.: The Dynamic Method in Oceanography, Elsevier Pub. Co., 1964.

3–62. NEUMANN, GERHARD: Ocean Currents. Elsevier Pub. Co., 1968.

3–63. KRISHEN, K.: Correlation of Radar Backscattering Cross Sections With Ocean Wave Height and Wind Velocity. Geophys. Res., vol. 76, Sept. 1971, pp. 6528–6539. (See also Krishen, K.: Mathematical Model for the Relationship of Radar Backscattering Cross Sections With Ocean Scene and Wind Velocity. Proceedings of the Seventh International Symposium on Remote Sensing of Environment, vol. III, Univ. of Michigan, May 1971, pp. 1861–1877.)

3–64. DALEY, J. C.: Wind Dependence of Radar Sea Return—Composite Surface Model. J. Geophys. Res., vol. 78, no. 33, Nov. 1973, p. 7823.

3–65. VALENZUELA, G. R.; LAING, M. B.; AND DALEY, J. C.: Ocean Spectra for High Frequency Waves From Airborne Radar Measurements. J. Mar. Res., vol. 29, no. 2, 1971, p. 69.

3–66. HUANG, NORDEN E.; CHEN, DAVIDSON T.; TUNG, CHI CHAO; AND SMITH, JAMES R.: Interaction Between Steady Non-Uniform Currents and Gravity Waves, With Applications for Current Measurements. J. Phys. Oceanogr., vol. 2, Oct. 1972, pp. 420–431.

3–67. PIERSON, WILLARD J., JR., AND MOSKOWITZ, LIONEL: A Proposed Spectral Form for Fully Developed Wind Seas Based on the Similarity Theory of S. A. Kitaigorodskii. J. Geophys. Res., vol. 69, no. 24, Dec. 1964, p. 5181.

3–68. CORNISH, VAUGHN: Ocean Waves and Kindred Geophysical Phenomena. Cambridge Univ. Press, 1934.

3–69. NEUMANN, G.: On Ocean Wave Spectra and a New Method of Forecasting Wind Generated Seas. Tech. Memo. 43, U.S. Army Coastal Engineering Research Center (Fort Belvoir, Va.), 1953.

3–70. PIERSON, WILLARD J., JR.; NEWMANN, GERHARD; AND JAMES, RICHARD W.: Practical Methods for Observing and Forecasting Ocean Waves by Means of Wave Spectra and Statistics. Pub. No. 603, U.S. Navy Hydrographic Office, 1955.

3–71. PHILLIPS, OWEN M.: The Dynamics of the Upper Ocean. Cambridge Univ. Press, 1966.

3–72. Environmental Conditions Within Specified Geographical Regions, Final Report. U.S. Department of Commerce, The National Data Buoy Center, National Ocean Survey,

NOAA Mississippi Test Facility, Apr. 1973.

3–73. HOGBEN, NEIL, AND LUMB, F. E.: Ocean Wave Statistics. National Phys. Lab., London, H.M.S.O., 1967.

3–74. GLOERSEN, P.; NORDBERG, W.; SCHMUGGE, T. J.; AND WILHEIT, T. T.: Microwave Signatures of First-Year and Multi-Year Sea Ice. J. Geophys. Res., vol. 78, no. 18, June 1973, pp. 3564–3572.

3–75. CAMPBELL, W. J.; GLOERSEN, P.; NORDBERG, W.; AND WILHEIT, T. T.: Dynamics and Morphology of Beaufort Sea Ice Determined From Satellites, Aircraft and Drifting Stations. NASA TM X–66291, 1973.

3–76. ANDERSON, V. H.: High Altitude, Side-Looking Radar Images of Sea Ice in the Arctic. Proceedings of the Fourth Symposium on Remote Sensing of Environment, Univ. of Michigan, Apr. 1966, pp. 845–857.

3–77. ROUSE, JOHN W., JR.: Arctic Ice Type Identification by Radar. Proc. IEEE, vol. 57, no. 4, Apr. 1969, pp. 605–611.

3–78. PARASHAR, S. K.; BRIGGS, A. W.; FUNG, A. K.; AND MOORE, R. K.: Investigation of Radar Discrimination of Sea Ice. Proceedings of the Ninth International Symposium on Remote Sensing of Environment, vol. I, Univ. of Michigan, Apr. 1974, pp. 323–332.

3–79. GLUSHKOV, V. M., AND KOMAROV, V. B.: Side-Looking Radar System TOROS and Its Application to the Study of Ice Conditions and Geological Explorations. Proceedings of the Seventh International Symposium on Remote Sensing of Environment, vol. I, Univ. of Michigan, May 1971, p. 317.

3–80. GLOERSEN, P.; WILHEIT, T. T.; CHANG, T. C.; NORDBERG, W.; AND CAMPBELL, W. J.: Microwave Maps of the Polar Ice of the Earth—From Nimbus 5 Satellite. NASA TM X–70493, 1973.

3–81. MCGOOGAN, J. T.: Precision Satellite Altimetry. IEEE International Convention and Exposition, Mar. 1974, pp. 34–31 to 34–37.

3–82. MCGOOGAN, J. T.; MILLER, L. S.; BROWN, G. S.; AND HAYNE, G. S.: The S–193 Radar Altimeter Experiment—Onboard Skylab for Earth Surface Profile Measurement. Proc. IEEE, vol. 62, June 1974, pp. 793–803.

3–83. VONBUN, F. O.: Geodetic Satellite Mission and GEOS–C Spacecraft. Space Research XI, COSPAR, vol. 1, Akademie-Verlag (Berlin), May 1971, pp. 457–467.

3–84. MACDONALD, F. C.: The Correlation of Radar Sea Clutter on Vertical and Horizontal Polarization With Wave Height and Slope. IRE Nat. Conv. Rec., pt. 1, Mar. 1956, pp. 29–32.

3–85. GRANT, C. R., AND YAPLEE, B. S.: Backscattering From Water and Land at Centimeter and Millimeter Wavelengths. Proc. IRE, vol. 45, no. 7, July 1957, pp. 972–982.

3–86. DALEY, J. C.; BURKETT, J. A.; DUNCAN, J. R.; AND RANSONE, J. T., JR.: Sea Clutter Measurement on Four Frequencies. Rep. 6806, Naval Res. Lab., Washington, D.C., Nov. 29, 1968.

3–87. DALEY, J. C., ET AL.: Upwind-Downwind-Crosswind Sea Clutter Measurement. Rep. 6881, Naval Res. Lab., Washington, D.C., Apr. 1969.

3–88. DALEY, J. C.; RANSONE, J. T., JR.; AND BURKETT, J. A.: Radar Sea Return—Joss 1. Rep. 7268, Naval Res. Lab., Washington, D.C., May 1971.

3–89. DALEY, J. C., ET AL.: Radar Sea Return—Joss 2, Final Report. Rep. 7534, Naval Res. Lab., Washington, D.C., Feb. 1962.

3–90. MOORE, R. K.: Radar Scatterometry—An Active Remote Sensing Tool. Proceedings of the Fourth Symposium on Remote Sensing of Environment, Univ. of Michigan, Apr. 1966, pp. 339–373.

3–91. MOORE, RICHARD K., AND PIERSON, W. J., JR.: Worldwide Oceanic Wind and Wave Predictions Using a Satellite Radar-Radiometer. J. Hydron., vol. 5, no. 2, Apr. 1971, pp. 52–60.

3–92. NEWTON, RICHARD W., AND ROUSE, JOHN W., JR.: Experimental Measurements of 2.25-cm Backscatter From Sea Surfaces. IEEE Trans. Geosci. Electronics, vol. GE–10, no. 1, Jan. 1972, pp. 2–7.

3–93. KERR, F. J., AND SHAIN, C. A.: Moon Echoes and Transmission Through the Ionosphere. Proc. IRE, vol. 39, no. 3, Mar. 1951, pp. 230–242.

3–94. WRIGHT, JOHN W.: Backscattering From Capillary Waves With Application to Sea Clutter. IEEE Trans. Antennas Propagat., vol. AP–14, no. 6, Nov. 1966, pp. 749–754.

3–95. KRISHEN, K.; VLAHOS, N.; BRANDT, O.; AND GRAYBEAL, G.: Results of Scatterometer Systems Analysis for NASA/MSC Earth Observation Sensor Evaluation Program. Proceedings of the Seventh International Symposium on Remote Sensing of Environment, vol. II, Univ. of Michigan, May 1971, pp. 1451–1473.

3–96. SWIFT, C. T., AND JONES, W. L., JR.: Satellite Radar Scatterometry. IEEE International Convention and Exposition, Mar. 1974, pp. 34–41 to 34–46.

3–97. Historical Logbook, S–193 Microwave Radiometer/Scatterometer/Altimeter. No.

72SD234, rev. A, vols. 1 to 10, General Electric Corp., Oct. 1972.

3–98. KRISHEN, K.: Contribution to Ocean Panel Including Reports on Some Sea Return Experiments, Ocean Surface Windspeed Sensing and Scatterometers. Tech. Rep. LEC–3896, Lockheed Electronics Co., Inc., July 1974.

3–99. MOORE, R. K., ET AL.: Simultaneous Active and Passive Microwave Response of the Earth—the Skylab RADSCAT Experiment. Proceedings of the Ninth International Symposium on Remote Sensing of Environment, vol. I, Univ. of Michigan, Apr. 1974, pp. 189–217.

3–100. YAPLEE, B. S.; SHAPIRO, A.; HAMMOND, D. L.; AND ULIANA, E. A.: Ocean Wave Height Measurements With a Nanosecond Radar. Proceedings of the Seventh International Symposium on Remote Sensing of Environment, vol. III, Univ. of Michigan, May 1971, pp. 1879–1893.

3–101. APEL, J. R., ed.: Sea Surface Topography From Space. NASA CR–130293, 1973.

3–102. WEISSMAN, D. E.: Two Frequency Radar Interferometry Applied to the Measurement of Ocean Wave Height. IEEE Trans. Antennas Propagat., vol. AP–21, Sept. 1973, pp. 649–656.

3–103. SWIFT, C. T.: Microwave Radiometer Measurements of the Cape Cod Canal. Radio Sci., vol. 9, July 1974, pp. 641–653.

3–104. STOGRYN, A.: The Emissivity of Sea Foam at Microwave Frequencies. J. Geophys. Res., vol. 77, Mar. 1972, pp. 1658–1666.

3–105. HOLLINGER, JAMES P.: Remote Passive Microwave Sensing of the Ocean Surface. Proceedings of the Seventh International Symposium on Remote Sensing of Environment, vol. III, Univ. of Michigan, May 1971, pp. 1807–1817.

3–106. CARDONE, V. J.: Specification of the Wind Field Distribution in the Marine Boundary Layer for Wave Forecasting. Rep. TR 69–1, Geophys. Science Lab., New York Univ., Dec. 1969.

3–107. ROSS, DUNCAN B., AND CARDONE, VINCENT: Observations of Oceanic Whitecaps and Their Relation to Remote Measurements of Surface Wind Speed. J. Geophys. Res., vol. 79, no. 3, Jan. 20, 1974, pp. 444–452.

3–108. Reference Data for Radio Engineers. Fourth ed. International Telephone & Telegraph Corp., Stratford Press, Inc., 1961.

3–109. MOORE, RICHARD K.; WAITE, WILLIAM P.; AND ROUSE, JOHN W., JR.: Panchromatic and Polypanchromatic Radar. Proc. IEEE, vol. 57, no. 4, Apr. 1969, pp. 590–593.

3–110. VALENZUELA, G. R., AND LAING, M. B.: Study of Doppler Spectra of Radar Sea Echo. J. Geophys. Res., vol. 75, no. 3, Jan. 1970, p. 551.

3–111. LAING, M. B.: The Upwind/Downwind Dependence of the Doppler Spectra of Radar Sea Echo. IEEE Trans. Antennas Propagat., vol. AP–19, no. 5, Sept. 1971, pp. 712–714.

3–112. KATZ, I.: Utilization of a Radar Altimeter for Determination of Ocean Roughness. IEEE EASCON Conv. Rec., Oct. 1970, pp. 266–269.

3–113. BORN, MAX, AND WOLF, EMIL: Principles of Optics. Third ed. Pergamon Press, 1965.

## APPENDIX 3A

## ORBITAL ERRORS

Ever since orbits have been computed—of celestial bodies during the last several centuries or of artificial satellites during recent times—orbital errors in position and velocity have attracted the attention of analysts. Orbital errors were a major consideration when rockets and artificial satellites were first launched. As space missions increased and became more sophisticated, requirements for the reduction of orbital errors became increasingly important.

Presently, orbital accuracies in the meter, decimeter, and even centimeter region in position and in millimeters per second or less in velocity are needed for Earth and ocean dynamic satellite missions [1] (ref. 3A–1).

Such missions as Skylab, GEOS–C, and particularly SEASAT–A required orbital ac-

[1] NASA: Earth and Ocean Physics Applications Program. Vol. I—Executive Summary, Vol. II—Rationale and Program Plan, Sept. 1972 (NASA internal document, restricted distribution).

curacies commensurate with requirements to determine the gross features of the sea surface topography (ref. 3A–2).

Figures 3–45 and 3–46 depict the orbital height differences (quasi-errors) of the Skylab missions. Figure 3–45 shows a 25-m height variation and figure 3–46 shows a 40-m height variation, which can be seen from the difference of the "measured" sea surface and the "computed" sea surface, assuming that the bias error in the radar altimeter is small compared with these values mentioned. Experience indicates that crosstrack errors and along-track errors may be three to eight times as large, respectively (ref. 3A–3). The GEOS–C has an altimeter that can measure spacecraft height above the oceans within 0.5 to 1.0 m. Experience with Skylab certainly justifies the belief that these rather small values are attainable [2] (refs. 3A–4 and 3A–5). This knowledge, in turn, dictates that orbital height errors must be known to the same order of accuracy. Only the orbital radial component (height) is of importance for ocean altimetry.

## PRESENT STATE OF THE ART

A realistic estimate of the errors must include all errors associated with the basic measurements (tracking systems), electromagnetic propagation (troposphere and ionosphere), tracking station location, timing, basic physical constraints, and, in particular, the gravity field of the Earth. In addition, the errors have to be separated into random errors, which are subject to statistics, and bias errors, which stay more or less constant during the measurement processes. The bias errors are more harmful because they do not decrease inversely as the square root of the number of samples. An increase in the number of measurements does not decrease the total error of the spacecraft position and velocity.

## UNDERSTANDING THE PROBLEM

A brief outline will be given on the general subject of orbital uncertainty estimates, which will be interpreted as orbital errors. Both theoretical error analyses and orbital uncertainty estimates are discussed in some detail.

### Orbital Uncertainty Estimates

Orbital uncertainty estimates (refs. 3A–3 and 3A–6) are based on practical orbital determination and include all errors (known and unknown) that appear when an orbit is calculated. The principle is rather simple and is depicted in figure 3A–1. Orbits, which are calculated for 2-day time intervals, overlap by 1 day. The maximum and minimum position differences in the overlap region are recorded as a measure of the uncertainty associated with the orbit. These arcs have different data sets, different tracking stations, and, as mentioned, describe reality.

### Orbital Errors Using Error Theory

In many cases, particularly during project planning phases, error analyses have to be performed on a theoretical basis only, because the tracking system to be used is not yet built and/or the spacecraft is not designed. These techniques have been used for basic designs of range and range-rate systems, the Apollo Tracking Network, and plans for a new orbiting tracking system, which is presently under investigation (refs. 3A–7 to 3A–11).

Figures 3A–2, 3A–3, and 3A–4 show some examples of the orbital uncertainty estimates

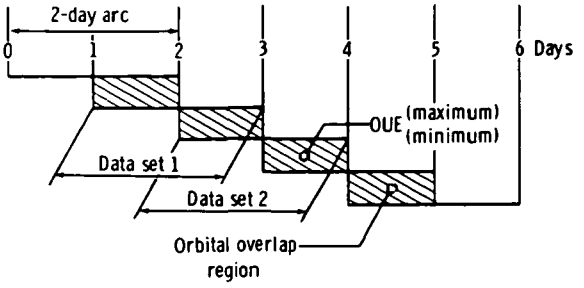


FIGURE 3A–1.—Schematic illustrating principle of orbital uncertainty estimates. Orbits are "connected" at that time within the overlap region where the position differences are at a minimum (case of 100-percent overlap).

[2] Personal communication, McGoogan, 1974.

that have been obtained for the Orbiting Geophysical Observatory IV (OGO–IV) and GEOS–I and GEOS–II. Thus, the OGO–IV spacecraft orbital uncertainty estimates during the 30-day period depicted in figure 3A–2 cover the band between 50 and 700 m; that is, the average position error should be approximately 300 m. Similarly, from figure 3A–3, if one determines a GEOS–1 orbit with the Goddard minitrack system only, the orbital uncertainty estimates cover a band from 30 to 210 m during the 15-day timespan. If good optical data are used, orbital uncertainty estimates vary between only 0 and 30 m. However, these values are still, to a certain extent, relative rather than absolute values.

An error analysis (refs. 3A–7 to 3A–11) for the 30-day OGO–IV orbit has been performed, and the result is superimposed on the orbital uncertainty estimates shown in figure 3A–2. The orbit uncertainties, based on the

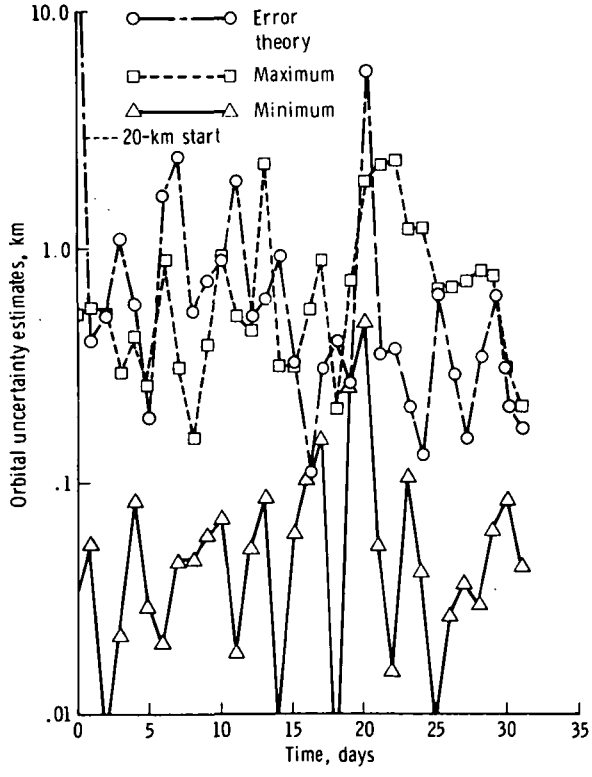


FIGURE 3A–2.—Orbital uncertainty estimates for OGO–IV.

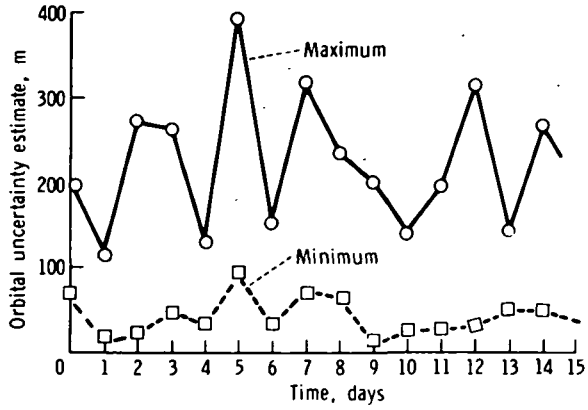


FIGURE 3A–3.—Orbital uncertainty estimates for GEOS–I.

error theory applied, fall within the upper regions of the error as determined by the overlap method. This agreement is considered good because a 50-percent "error-of-the-error" determination is an acceptable first theoretical estimate.

As previously mentioned, it is very difficult to make accurate theoretical predictions of expected orbital errors. Tracking system error parameters (refs. 3A–11 to 3A–15) have to be determined and chosen from previous orbital analyses. The information presented in figure 3A–2 shows that these theoretical errors are on the high side because rather large system bias error values are used in the error theory, and biases contribute most to the orbital errors. Noise contributions reduce statistically with an increase in the number of measurements used, whereas bias contributions, by their nature, stay constant (refs. 3A–7 to 3A–9) regardless of the number of measurements taken and actually used.

During the past few years, considerable progress has been made in reducing orbital errors because of improvements in determining (1) the Earth gravity field model (the major contributor to orbital errors); (2) the mathematical orbital systems models; and (3) the errors in the tracking system, although this has not been fully exploited at this time.

This paragraph gives some examples of orbital uncertainty estimates for GEOS–II us-

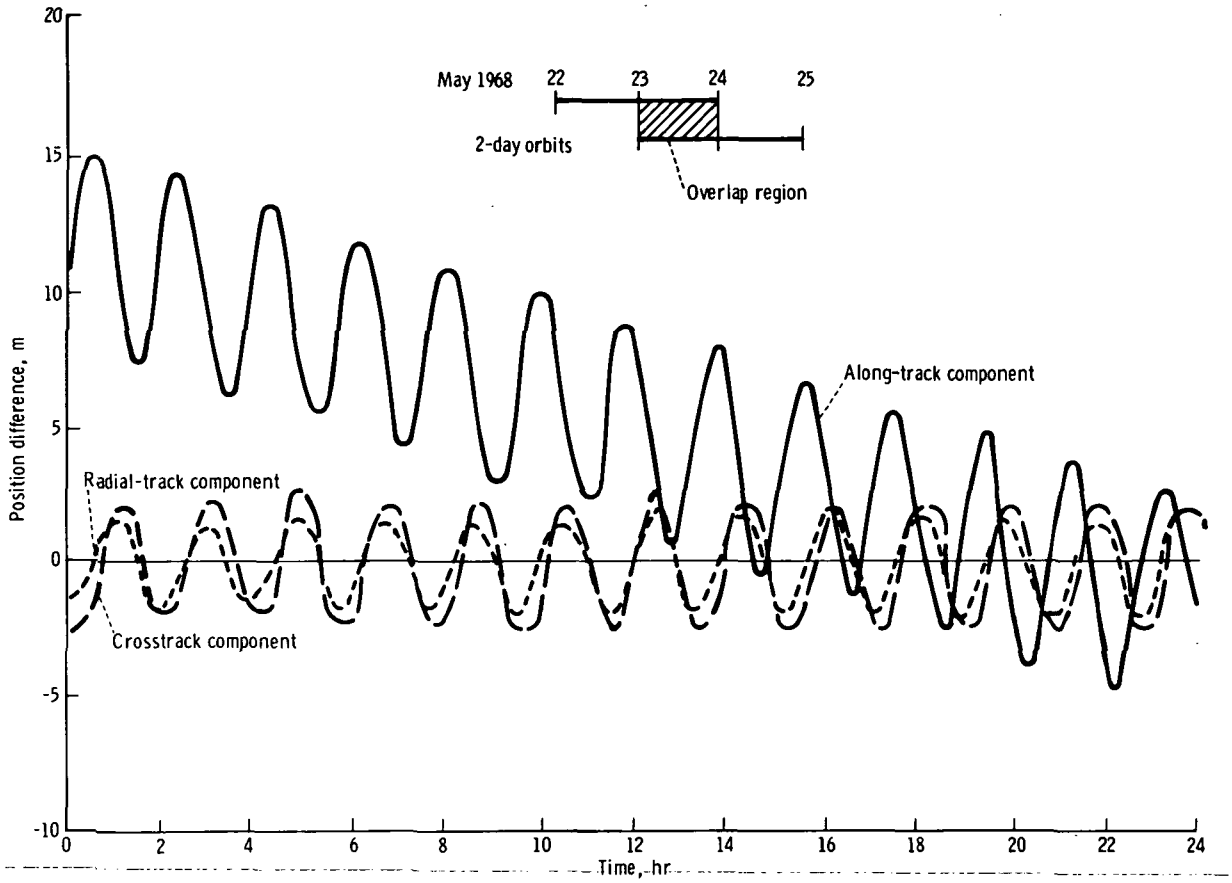


FIGURE 3A–4.—Satellite overlap position differences for GEOS–II (GEM–6 model, Naval Weapons Laboratory Doppler).

ing Naval Weapons Laboratory Doppler and optical data. The examples concern three different gravity fields: namely, the Goddard Earth models (GEM–1 and GEM–6) and the Smithsonian Astrophysical Institution (SAO). Figure 3A–4 shows the orbital uncertainty estimates for a 1-day overlap in the along-track, crosstrack, and radial-track components of the orbit. It is interesting to note that the GEM–6 errors in altitude are smaller than the GEM–1 errors (2-day computation shown in fig. 3A–5). However, if one intends to project the orbit 10 days into the future, the GEM–6 model performs this task very well (fig. 3A–5). Assuming that the GEM–6 model is better than the GEM–1 model, one should expect a good performance because, during the projection period, the satellite orbit depends solely on the gravity field. Finally, figure 3A–4 shows the behavior of the orbital uncertainty estimates over a 24-hr period of overlap. Only the along-track component has much deviation. Radial-track and crosstrack components linearly cancel out, as they should from orbital energy consideration. The sinusoidal-like variations do have orbital periodicity, as theoretically expected (ref. 3A–9).

## IMPACT OF MICROWAVE TECHNOLOGY

The only metric measurements taken from orbit that are closely related and/or dependent on accurate orbital information are radar altimeter data. All other oceanographic measurements, such as wave height, wave direc-

| Gravity field | June 1 to 3, 1968 | | | June 10 to 13, 1968 | | |
|---|---|---|---|---|---|---|
| | Radial track, m | Cross-track, m | Along track, m | Radial track, m | Cross-track, m | Along track, m |
| GEM-1 | 13.0 | 26.6 | 289 | 6.6 | 30.6 | 922 |
| GEM-6 | 8.6 | 25.3 | 91 | 11.8 | 33.2 | 555 |
| SAO-2 | 9.3 | 51 | 366 | 26.2 | 78 | 948 |

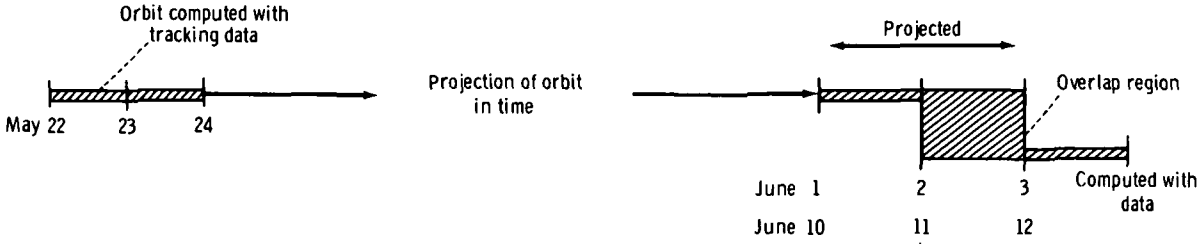


FIGURE 3A–5.—Satellite overlap projected position differences in meters for GEOS–II.

tion, and microwave images, are not so dependent on accurate position and thus on orbit determination. Spaceborne altimeter systems such as those flown (or to be flown) on Skylab, GEOS–C, and SEASAT have a substantial effect on the orbital error determination. Instead of having only a few minutes of tracking data, one can obtain such data almost continuously along the orbit (except over land areas).

The effect in this case is twofold. First, the orbital errors will be reduced (more tracking and an improved gravity field); second, the sea surface topography can actually be measured for the first time (ref. 3A–2). The Skylab results are tremendously encouraging in this respect. Much sea surface topography information[3] has already been extracted from Skylab data, and the analysis is just beginning. Relating this fact to the increased coverage that GEOS–C will have as compared to Skylab, gravity field and sea surface topography improvements will be substantial.

Thus, sea-surface topography errors that are, at present, approximately 2 to 15 m or more will be reduced. The estimates are that GEOS–C will reduce these geoidal error values on a global scale from 0.5 to 2 m in 2 to 3 yr, facilitating the way for the SEASAT–A mission with the ultimate goal of determining the sea surface topography to within 0.1 to 0.2 m (ref. 3A–1).[4]

## REQUIREMENTS

Orbital height errors have to be reduced considerably if the EOPAP requirements for the sea-surface topography are to be satisfied. As shown in figures 3–45, 3–46, 3A–1, 3A–4,

[3] Personal communication, McGoogan, 1974.

[4] Also, see Earth and Oceans Physics Applications Program. Vol. I—Executive Summary, Vol. II—Rationale and Program Plan, Sept. 1972 (NASA internal document, restricted distribution).

and 3A–5, orbital errors are still in the meter range. However, when proper boundary conditions are imposed on the oceans,[5] the errors in determining the sea-surface topography may be smaller, by a factor of 3 to 5, than those of the orbital height under certain restraining conditions. For example, a nodal distance of 19° (half wavelength of error) and a 1-m orbital height error would contribute only 0.10 to 0.15 m to the geoid error. Any orbital altitude bias error would transform directly into an equivalent geoid error. For instance, a constant height error results from an error in the Earth gravitational parameter. Thus, another requirement for accurate altimetry is the better determination of this parameter.

## REFERENCES


3A–1. The Terrestrial Environment: Solid-Earth and Ocean Physics. NASA CR–1579, 1970.

3A–2. VONBUN, F. O.: A Simulation of Synthetic Aperture Radar Imaging of Ocean Waves. Paper presented at 1974 Annual URSI Meeting (Boulder, Colo.), Oct. 1974.

3A–3. VONBUN, F. O.: Satellite Trajectory Determination and Their Expected Errors, OGO IV, GEOS–1. Dynamics of Satellites, Springer-Verlag (Berlin), 1970, pp. 89–97.

3A–4. VONBUN, F. O.: Sea Surface Determination From Space—The Goddard Geoid. USNC/URSI–IEEE Meeting (Boulder, Colo.), Oct. 1971.

3A–5. VONBUN, F. O.: Spacecraft Missions and Experiments Important to Geodynamics. The XVII Plenary Meetings, COSPAR (São Paulo, Brazil), 1974.

3A–6. SIRY, J. W., AND STEWART, D. J.: Goddard Orbit Information. NASA TM X–63892, 1969.

3A–7. VONBUN, F. O., AND KAHN, W. D.: Tracking Systems, Mathematical Models and Errors, Part I—Theory. NASA TN D–1471, 1962.

3A–8. KAHN, W. D., AND VONBUN, F. O.: Tracking Systems, Mathematical Models and Errors, Part II—Least Squares Treatment. NASA TN D–3776, 1966.

3A–9. BONAVITO, N. L.: An Analysis of Satellite Positional Uncertainty by Statistical Mechanics. NASA TN D–5259, 1969.

3A–10. VONBUN, F. O., AND MENGEL, J. T.: Tracking and Communications for Planetary Manned Missions. J. Spacecr. Rockets, vol. 5, no. 5, July 1968, pp. 863–865.

3A–11. COOLEY, J. L., AND MARLOW, A.: Orbital Error Studies—Tracking From a Synchronous Spacecraft. NASA TM X–551–69–7, 1969.

3A–12. SCHROEDER, CLARENCE A.: Electronic Interferometer Tracking. IEEE Transactions on the Fifth National Symposium on Space Electronics and Telemetry (Washington, D.C.), Sept. 19–21, 1960, pp. 1–9.

3A–13. KRUGER, B.: The Range Rate Error Due to the Averaging Techniques of Doppler Measurements. NASA TM X–55203, 1965.

3A–14. KRUGER, B.: Effects of Correlated Noise With Applications to Apollo Tracking Problems. NASA TN D–4121, 1968.

3A–15. MARSH, J. G., ET AL.: Intercomparison of the Minitrack and Optical Tracking Networks Using GEOS–I Long Arc Orbital Solutions, Part I. NASA TM X–63161, 1967.


[5] Personal communication, Mathews, 1974.

## APPENDIX 3B

## NATIONAL PRIORITY AREAS FOR COASTAL ZONES

The VIMS study is summarized in the following information. Remote sensing of temperature and salinity are two high-priority items, whereas sea state is a low-priority item.

The priorities for environmental data are as follows:

1. Water pollution and ecosystem balance
   a. Water pollution:
      (1) Toxic wastes, biocides, and heavy metals ..... 9
      (2) Sewage, nutrients, and oxygen-demanding wastes .. 9
      (3) Radioactivity ..... 9

(4) Oil ..... 9
(5) Suspended sediment ..... 8
(6) Thermal effluent ..... 9
*b.* Estuarine and coastal ecosystems:
(1) Producers:
(a) Wetlands; etc. ..... 9
(b) Phytoplankton ..... 9
(c) Coastal vegetation .... 9
(2) Hydrography
(a) Dissolved oxygen .... 9
(b) Salinity ..... 9
(c) Temperature ..... 9
(d) Currents and circulation ..... 9
(3) Chemical cycles ..... 8
(4) Mathematical models ..... 9
2. Natural resources:
*a.* Food
(1) Fish ..... 8
(2) Shellfish ..... 7
*b.* Water supply ..... 5
*c.* Minerals ..... 3
3. Extreme events: prediction, survey, and assessment of coastal storms, earthquakes, and tsunamis:
*a.* Sea state ..... 4
*b.* Surge, tides, and sea level ..... 4
*c.* Littoral response, shoals, and shorelines ..... 4
4. Other aids to shipping and navigation:
*a.* Ice cover ..... 2
*b.* Shoals, shorelines, seastate, and currents ..... 2

The following list enumerates the remote measurables defined by VIMS. Nos. 13, 15, and 16 were not included in the matrix.

1. Ice
2. Sea level (altimetry)
3. Sea state
4. Tides
5. Salinity
6. Water color
7. Water-surface temperature
8. Oilslicks
9. Bathymetry
10. Shorelines
11. Shore topography
12. Coastland vegetation and land use
13. Benthic vegetation
14. Fish schools
15. Coastal mammals
16. Bioluminescence

The areas in which active microwave systems may be applicable are indicated in table 3B–I.

The following items are recommended by VIMS for a coastal zone oceanography program.

1. Remote sensing of salinity (top priority).
2. Development of common satellite for oceanography and meteorology.
3. Development of computer-simulation models of major estuaries.
4. Accurate mapping of coastal wetlands.
5. Development of remote sensing as the primary method for detecting suspended sediments.
6. Provision for data acquisition of selected areas by command.

The approach taken by ODU to establish priorities was to circulate a questionnaire to universities, industries, institutions, and State and local governments. The results again show that more disciplines require tem-

TABLE 3B–I.—*Order of Priority of Remote Measurables Defined by VIMS* [a]

| Remote measurable | Percent score | Percent score with weighting factor removed |
|---|---|---|
| Water-surface temperature | 19.0 | 17.7 |
| Water color | 15.0 | 13.6 |
| Salinity | 14.4 | 13.2 |
| Coastland vegetation and land use [b] | 12.7 | 11.8 |
| Oil [b] | 8.3 | 7.7 |
| Bathymetry | 7.1 | 7.7 |
| Tides [b] | 5.5 | 6.4 |
| Shorelines [b] | 4.8 | 5.0 |
| Shore topography [b] | 3.7 | 4.1 |
| Sea state [b] | 2.8 | 4.1 |
| Sea level and altimetry [b] | 2.6 | 3.2 |
| Ice | 2.3 | 3.6 |
| Fish schools | 1.9 | 1.8 |

[a] Current and circulation data can be derived by means of several of the remote measurables.
[b] Denotes active microwave sensing potential.

perature/salinity measurements than sea-state measurements. The following priorities in coastal zones have been established by ODU as a result of the questionnaires.

1. Biological oceanography:
   a. Pollution
   b. Fisheries
   c. Coastal geography and cartography
   d. Hazards to shipping and coastline
2. Marine geology
   a. Baseline studies: physical, chemical, biological, and geological environment
   b. Pollution
   c. Shoreline processes
   d. Oil and mineral resources not urgent
3. Chemical oceanography:
   a. Pollution
   b. Studies related to establishing fertility of coastal waters
4. Physical oceanography/meteorology:
   a. Water-mixing dynamics
   b. Baseline data for understanding physical regime
   c. More data on spatial and temporal distribution of parameters for mathematical models

The following information needs in coastal zones have been defined by ODU.

1. Pollution:
   a. Pathways of pollution in biological systems and tolerance
   b. Importance of estuaries in general ecology and influence of pollution
   c. Good hydrological information
   d. Adequate instrumentation
2. Fisheries:
   a. Physical oceanographic studies
   b. Systematic study of specimens
   c. Population dynamics
   d. Effects of environmental alteration
3. Geological processes:
   a. Suspended sediment circulation and transport in deep and shallow water
   b. Bathymetry data
   c. Wave energy
4. Chemistry:
   a. More emphasis on transport and long-term deposition of pollutants
   b. Analytical methods for specific organic pollutants in all waters
   c. Upgrade gathering, monitoring, treatment of basic data
   d. Physical and chemical properties of particles in water
   e. Mathematical description of natural water systems
5. Physical oceanography/meteorology:
   a. Physical data of water system
   b. Effluent characteristics
   c. Nutrient distribution
   d. Incoming radiation and effective back radiation
   e. Evaporation and precipitation
   f. Improved predictions with math models

The number of disciplines requiring remote measurables defined by ODU are listed in table 3B–II.

The following information is a description of ODU recommendations for the coastal zone oceanography program.

1. Data for improving knowledge of coastal water-mixing processes.

2. Need for large engineering data base of reliable data:
   a. Surface waves
   b. Wastes and pollution
   c. Sea/shore interactions
   d. Seabed conditions

TABLE 3B–II.—*Number of Disciplines Requiring Remote Measurables Defined by ODU*

| Remote measurable | Number of disciplines |
|---|---|
| Water mixing | 4 |
| Surface temperature | 4 |
| Salinity | 4 |
| Suspended sediments | 4 |
| Sea level | 3 |
| Nutrients | 3 |
| Sea state | 2 |
| Bathymetry | 2 |
| Vegetation and soils | 2 |
| Oil | 2 |
| Shorelines (cartography) | 2 |
| Radiation | 1 |
| Evaporation | 1 |

3. Coordination of oceanographic and meteorological observations with ERTS programs: World Weather Watch, GARP, and Integrated Global Ocean Station System.

4. Establishment of communications between NASA and director of IDOE to discuss cooperative efforts.

5. Establishment of a coastal zone management system needed for coordinating disciplinary interests.

Item 2 seems to be a probable area for active microwave techniques.

The problems considered by ODSI are presented in table 3B–III, and a priority listing that reflects the ODSI, VIMS, and ODU studies is given in table 3B–IV. The areas in which active microwave techniques may be appropriate are indicated in table 3B–IV. Note that wave measurements are at the bottom of the list.

The desired measurables as a function of resolution requirements are shown in table 3B–V. One of the most notable aspects of the chart is that spatial resolutions as small as 10 m are required. For this reason, perhaps the microwave studies of coastal regions would be restricted to those done from aircraft.

TABLE 3B–III.—*National Priority Area Issues and Most Relevant Data Types for Each Area in the Coastal Zone Defined by ODSI*

| Priority area | Issue | Relevant data types |
|---|---|---|
| Pollution | Locate sources of discharge | Petroleum |
| | Determine types of discharge | Bioassays |
| | Determine extent of pollution effects | Water temperature |
| | Determine assimilative capacity | Currents |
| | Determine optimal siting for industry | Salinity |
| | Effect enforcement | Water density |
| | Assist rapid cleanup | Permeability |
| | | pH |
| | | Tides |
| | | Metals |
| | | Plankton |
| | | Color |
| | | Bathymetry |
| | | Particulates |
| | | Porosity (bottom) |
| | | Bottom $O_2$ uptake |
| | | Bacteria |
| | | Sediment pH |
| Fisheries | Locate new fishing areas | Fish |
| | Improve scouting operations | Plankton |
| | Improve catching operations | Currents |
| | Forecast abundance | Bathymetry |
| | Improve management | Water temperature |
| | | Nutrients |
| | | Mammals |
| | | Freshwater inflow |
| | | Bioassays |
| | | Salinity |
| | | Dissolved gases |
| | | Dissolved organics |
| | | Color |
| Hazards to shipping and coastlines. | Identify hazards to navigation | Winds |
| | Provide climatology | Water temperature |
| | Monitor ocean phenomena | Currents |
| | Assist rescue operations | Ice |

TABLE 3B–III.—*National Priority Area Issues and Most Relevant Data Types for Each Area in the Coastal Zone Defined by ODSI—Concluded*

| Priority area | Issue | Relevant data types |
|---|---|---|
| | | Waves<br>Air temperature<br>Precipitation<br>Clouds<br>Barometric pressure<br>Breakers and surf<br>Tides<br>Bathymetry<br>Humidity<br>Solar radiation<br>Topography |
| Coastal geography and cartography. | Assess mineral resources<br>Improve coastal surveys<br>Identify land use<br>Monitor shoreline processes | Bathymetry<br>Sediments<br>Topography<br>Land use<br>Soils and geology<br>Currents<br>Tides<br>Vegetation<br>Water temperature<br>Sediment settling rate<br>Radioactive tracer concentration<br>Particulates<br>Color<br>Metals<br>Petroleum |

TABLE 3B–IV.—*A Comparison of Coastal Zone Data Requirements Established by ODSI, VIMS, and ODU*

| ODSI, remote measurable | ODSI, percent score | VIMS, weighting factor | ODU, number of disciplines |
|---|---|---|---|
| Currents[a] | 7.5 | 9 | 4 |
| Bathymetry | 7.2 | 9 | 2 |
| Water temperature | 7.0 | 9 | 4 |
| Tides[a] | 5.0 | 4 | 3 |
| Petroleum[a] | 0.8 | 9 | 2 |
| Sediments | 4.6 | 8 | 4 |
| Winds[a] | 4.5 | 4 | 2 |
| Color | 4.5 | | |
| Plankton | 4.3 | 9 | 1 |
| Salinity | 4.3 | 9 | 4 |
| Precipitation | 4.0 | | |
| Vegetation[a] | 3.9 | 9 | 2 |
| Air temperature | 3.9 | | |
| Fish | 3.7 | 8 | |
| Bioassays | 3.7 | | |
| Nutrients | 3.7 | 9 | 3 |
| Topography[a] | 3.7 | 4 | 2 |
| Water density | 3.5 | | 1 |
| Freshwater inflow | 3.5 | 5 | 1 |
| Particulates | 3.5 | 9 | 1 |
| Metals | 3.1 | 9 | 1 |
| Land use | 3.1 | | 2 |
| Waves[a] | 3.0 | 4 | 2 |

[a] May be appropriate for active microwave techniques.

TABLE 3B–V.—*Remote-Sensing Requirements for Water Pollution Monitoring*

| Remote measurable | Type[a] | Spatial resolution, m | Spectral resolution | Spectral range | Temporal resolution | Solar elevation, deg | Low angle from nadir, deg | Area coverage, km |
|---|---|---|---|---|---|---|---|---|
| Temperature | A | 10 | ±1 K | 10 to 12 μm | 2 hr | NA[b] | NA | 20 by 20 |
| | B | 100 | ±1 K | or | 7 days | | | 150 by 150 |
| | C | 1000 | ±1 K | 3 to 5 μm | 7 days | | | 300 by 300 |
| Currents | A | 10 | 0.01 m/sec | 0.4 to 0.8 μm | 2 hr | NA | NA | 20 by 20 |
| | B | 100 | 0.05 m/sec | | 7 days | | | 150 by 150 |
| | C | 1000 | 0.05 m/sec | | 7 days | | | 300 by 300 |
| Salinity | A | NA | NA | NA | 2 hr | NA | NA | NA |
| | B | 100 | ±0.5‰ | MW[c] | 6 hr | | | 150 by 150 |
| | C | 1000 | ±0.5‰ | MW[c] | 7 days | | | 300 by 300 |
| Surface winds | A | 10 | ±0.1 m/sec | 0.4 to 0.8 μm | NA | 30 to 60 | −5 to 30 | NA |
| | B | 100 | ±0.5 m/sec | or MW[c] | 6 hr | | | 150 by 150 |
| | C | 1000 | ±0.5 m/sec | | 7 days | | | 300 by 300 |
| Oil | A | 10 | 0.1 μm | 0.3 to 0.8 μm | 2 hr | 30 to 60 | −5 to 30 | 20 by 20 |
| | B | 100 | 0.1 μm | or MW[c] | 6 hr | | | 150 by 150 |
| | C | 1000 | 0.1 μm | | 7 days | | | 300 by 300 |
| Plankton | A | 10 | 0.05 μm | 0.4 to 0.8 μm | 1 day | 30 to 60 | −5 to 30 | 20 by 20 |
| | B | 100 | 0.05 μm | | 7 days | | | 150 by 150 |
| | C | 1000 | 0.05 μm | | 7 days | | | 300 by 300 |
| Sediments | A | 10 | 0.05 μm | 0.4 to 0.8 μm | 1 day | 30 to 60 | −5 to 30 | 20 by 20 |
| | B | 100 | 0.05 μm | | 7 days | | | 150 by 150 |
| | C | 1000 | 0.05 μm | | 7 days | | | 300 by 300 |
| Bathymetry | A | 10 | 10 percent | 0.4 to 0.8 μm | 30 days | 30 to 60 | −5 to 30 | 300 by 300 |
| | B | 100 | of aver- | | | | | |
| | C | 1000 | age depth | | | | | |
| Tides | A | 1000 | ±1 K or | 10 to 12, | 2 hr | 30 to 60 | −5 to 30 | 20 by 20 |
| | B | 1000 | 0.1 μm | 3 to 5, or | 6 hr | | | 150 by 150 |
| | C | 1000 | | 4 to 11 μm | 7 days | | | 300 by 300 |
| Nutrients | A | 10 | 0.015 μm | 0.4 to 0.8 μm | 1 day | 30 to 60 | −5 to 30 | 20 by 20 |
| | B | 100 | 0.015 μm | | 7 days | | | 150 by 150 |
| | C | 1000 | 0.015 μm | | 7 days | | | 300 by 300 |
| Chemical and toxic wastes | A | 10 | 0.015 μm | 0.3 to 0.8 μm | 5 hr | 30 to 60 | −5 to 30 | 20 by 20 |
| | B | 100 | 0.015 μm | | 7 days | | | 150 by 150 |
| | C | 1000 | 0.015 μm | | 7 days | | | 300 by 300 |

[a] A=locate source; B=determine effect; C=model inputs.
[b] NA=not applicable.
[c] MW=microwave.